Astronomy Reports, Vol. 46, No. 7, 2002, pp. 521–524. Translated from Astronomicheskiĭ Zhurnal, Vol. 79, No. 7, 2002, pp. 579–582.

Limitations on the Applicability of the Crystallographic Method for Determining the Topology of the Universe

D. D. Sokolov

Moscow State University, Moscow, 119992 Russia

Received February 14, 2001

Abstract—The regular crystallographic method for determining the topology of the spatial section of the Universe from observational data is of limited applicability if the mean density of the Universe has its critical value. © *2002 MAIK "Nauka/Interperiodica".*

1. INTRODUCTION

The Einstein equations relate the curvature of spacetime to the properties of matter without imposing direct constraints on the topology of spacetime. Therefore, if a cosmological model admits several topological interpretations, additional considerations are needed to choose the one corresponding to reality. This was noted by de Sitter as early as 1917, by F. Klein somewhat later, and by W. Clifford even earlier in the context of Newtonian cosmology. In the 1920s, the efforts of mathematicians (first and foremost, H. Hopf) led to the development of the theory of so-called Clifford–Klein spatial forms, or constant-curvature spaces with nontrivial topology (see [1] for a review). This theory was employed in the 1970s to obtain the first lower limits for the size of the region in space with a trivial topology from analyses of observational information. In particular, the analysis used three-dimensional arrays of data for discrete objects—galaxies, clusters of galaxies, and quasars with known redshifts [2]; it was also noted [3] that two-dimensional arrays of data on nonuniformities in the cosmic microwave background can, in principle, be used to determine the topology. Due to evolutionary effects for discrete sources and the highly uniform distribution of the microwave background, the first analyses based on observational data yielded unexpectedly low estimates for the size of the region of trivial topology; thus, in principle, nontrivial topological structure can be present even at distances much less than the distance to the horizon.

The discovery of fluctuations in the microwave background in the past decade prompted rapid progress in observational studies of the topology of the Universe [4, 5]. Since we do not see any clear features directly interpretable as manifestations of a nontrivial topology for the Universe in the distribution of inhomogeneities in the microwave background, it is natural to suppose that, if a nontrivial topology is present, it is manifest only at distances comparable to the distance to the horizon. The translation of these considerations into accurate estimates requires dedicated studies of the microwave-background inhomogeneities directed at elucidating the topology of the Universe. Such studies are foreseen in the scientific programs for the MAP and Plank satellites (see [6] for a popular description of the problem).

If we assume that the mean density of the Universe coincides with the critical density and, accordingly, the geometry of space is Euclidian, then even the currently available data guarantee that the topology is Euclidian to distances of the order of the distance to the horizon. However, the situation is much less clear in the case of a hyperbolic geometry [7], and advantages of models with nontrivial topology are being discussed in some contexts [8, 9].

In this situation, it is natural to consider the limitations of known methods for determining the spatial topology of the Universe. An analysis of this sort is done in [7] in connection with technical aspects of specific approaches to comparing theory and observations. It is claimed that these approaches provide stable results for a flat spatial section and work best for models with positive spatial curvature, but can yield unstable results for compact spaces with negative curvature.

Here, we turn our attention to the fact that current methods for determining the topology of the Universe have another limitation related to the very formulation of the Clifford–Klein problem. This limitation does not affect existing methods if they are applied to hyperbolic and elliptic cases, but can make their conclusions unstable in the Euclidian case, which is precisely the one that may be of most interest.

1063-7729/02/4607-0521$22.00

2. CRYSTALLOGRAPHIC METHOD

The basic idea of available methods used to study the topology of space is the following [1]. Let us consider an ordinary space of a uniform and isotropic cosmological model to be a universal covering space for spaces with nontrivial topology. We will consider the latter to be a glued-together world which can be taken to correspond to a fundamental region in the universal covering space. This region is multiplied by the action of a fundamental group that is a discrete subgroup of the group of motions for the universal covering space and covers the entire universal covering space. The spatial section of the glued-together world can be obtained by identifying the boundary points of the fundamental region. This construction resembles the construction of a crystal from a crystallographic cell, and observational methods based on this basis are termed crystallographic methods.

The action of the fundamental group gives rise to a sequence of ghosts produced by a source situated in the fundamental region, or to a periodic continuation of the microwave-background distribution from the fundamental region to the entire universal covering space. The comparison of theoretical distributions obtained in this way with the observed distributions constrains the topology of the Universe.

We can see that available tests for the determination of the topology of space are based on various nonuniformities in the cosmological model, which is considered to be strictly uniform and isotropic at the time of its construction. Of course, this type of inconsistency is quite usual in cosmology, but nevertheless poses some problems. The structural instability of the method to small perturbations of the geometry of space can, in principle, restrict the applicability of the results obtained in this approximation. This danger is implied by the very structure of the family of Clifford-Klein spatial forms, which depends smoothly on the spatial curvature K for nonzero K but is discontinuous at $K = 0$. In other words, the classification of topologies in the Euclidian case differs radically from the elliptical and hyperbolic cases, although the variation of the topology in these last two cases depends smoothly on curvature variations.

We will show that this discontinuity of the properties is related to the instability of the topological structure of space to small perturbations of the density near its critical value.

3. STABILITY OF THE TOPOLOGY OF SPACE

We will first show that, in a certain case, the topological structures of an elliptical and a hyperbolic world are stable against small density perturbations. Let us assume that the curvature of space is not equal to a constant value K, but instead varies weakly as a function of the spatial position and direction of a two-dimensional area in three-dimensional space. In geometric language, we consider the section curvature $K_\sigma(\mathbf{x})$ as a function of the point $\mathbf{x}$ and the two-dimensional direction σ in three-dimensional space. Obviously, this quantity can be represented as some convolution of the three-dimensional Riemann tensor [10, p. 113].

If a cosmological model is close to hyperbolic in the sense that $K_\sigma(\mathbf{x})$ is negative for any $\mathbf{x}$ and σ, the universal covering space is close to a singly connected Lobachevsky space, having, in particular, the same topology. This is a statement of the Hadamard–Kartan theorem (see, e.g., [10]). Since the proof of this theorem is fairly simple and illustrates the essence of the problem, we present its basic ideas here.

Let us consider two geodesics issuing from a given spatial point $\mathbf{y}$ in similar directions. The distance between these geodesics is proportional to the Jacobi field ξ, which can be obtained from the geodesic-deviation equation

$$\xi'' + K_\sigma(\mathbf{x})\xi = 0. \qquad (1)$$

Here, the prime denotes derivation with respect to the length of the geodesic and σ is a two-dimensional area related to both geodesics. The initial conditions for (1) are $\xi(\mathbf{y}) = 0$ (both geodesics issue from the same point $\mathbf{y}$) and $\xi'(\mathbf{y}) = 1$ (a normalization condition). If $K_\sigma(\mathbf{x}) < 0$, then ξ does not vanish for $\mathbf{x} \neq \mathbf{y}$, the geodesics intersect only at the point $\mathbf{y}$, and a geodesic polar coordinate system maps the space under study onto the Lobachevsky space. Using this so-called exponential mapping makes it possible to relate the properties of a space with variable negative curvature to those of a space with constant negative curvature.

The elliptical case is more complex, since Eq. (1) has oscillating solutions for $K > 0$. If the Jacobi field vanishes, a conjugate point (in astronomical language, a gravitational lens) appears on the geodesic. Conjugate points may signal changes in the topology of the universal covering space. Analysis of the structure of the set of conjugate points shows that, if the variations in the section curvatures are not too large, the properties of the universal covering space are close to those of a three-dimensional sphere. This is a statement of the so-called sphere theorem [10]. More precisely, if $\mathcal{K} = K_{\sigma_1}(\mathbf{x}_1)/K_{\sigma_2}(\mathbf{x}_2) \leq 4$, the universal covering space has the topology of a sphere. Since the Universe is highly uniform and isotropic, the universal covering space is also close to a three-dimensional spherical space in the elliptical case.

Thus, for the hyperbolic and elliptical cases, the Hadamard–Kartan theorem and the sphere theorem,

respectively, provide a basis for the stability of the crystallographic method.

In contrast, for the flat case, even small-amplitude curvature variations result in large variations in $\mathcal{K}$; therefore, there is no basis for stability of the crystallographic method against small perturbations. Moreover, such perturbations can actually change the topology of the universal covering space. For example, let us consider the metric

$$ds^2 = c^2dt^2 - a^2(t)[d\Sigma_2^2(R) + dz^2], \qquad (2)$$

where $a(t)$ is the scaling factor that describes the time evolution of the Universe and $d\Sigma_2^2(R)$ is the two-dimensional spherical metric of radius R. If the radius R is sufficiently large, the curvatures of the metric (2) are negligibly small, and its dynamics far away from the singularity are indistinguishable from those of a standard Friedmann model with a Euclidian spatial metric. At the same time, the spatial forms admitted by (2) differ from those for a Euclidian metric, and are not transformed into them as $R \to \infty$. Indeed, the Euclidian metric can be used to glue together a three-dimensional torus with arbitrary size; in contrast, the metric (2) can be constructed without restrictions only in the z direction, while the construction in the other two directions must conform to a spherical geometry. Thus, as noted in [11], the maximum size of the glued-together space in these directions is of order R. Note that the metric (2) is singly connected and cannot be mapped onto a Euclidian space.

In the context of the question under study, this means that, if we have found specific tests for the topology of a flat cosmological model based on the classification of three-dimensional, locally Euclidian spaces, we must also be prepared for the fact that the nearly flat real Universe could be constructed in some other way. It is this fact that limits the crystallographic method. Fortunately, this difficulty does not arise in the elliptical and hyperbolic cases.

4. DISCUSSION

Our analysis indicates that the crystallographic method is apparently a necessary stage in the elucidation of the topological structure of space, but does not yield conclusive results in the flat case. At the same time, precisely the Euclidian case appears most attractive for many theoretical and observational reasons. The special role played by the flat case is due to the fact that it does not involve any natural curvature scale, so that, strictly speaking, no curvature perturbations can be regarded to be small.

We demonstrated the instability of the crystallographic method using the metric (2). This metric is also interesting as an example of a three-dimensional space with a four-parameter, transitive group of motions, which cannot be reduced to a three-parameter group. Accordingly, this metric does not come under the classification of Bianchi.

Obviously, the metric (2) does not look attractive, and cosmological models with spatial curvatures randomly fluctuating about zero seem much more realistic. However, this case remains virtually unexplored in modern geometry; only one fundamental work by Zel'dovich [12] and several related studies (reviewed in [13]) can be noted in this context. Zel'dovich considered the propagation of light in a universe with the density fluctuating about its critical value.

Let us show that curvature fluctuations about a zero mean can indeed result in the appearance of conjugate points, i.e., in topological lensing. We assume that these fluctuations are Poisson; i.e., a geodesic can be divided into intervals of length δ on which the curvature acquires independent, uniformly distributed random values. In the theory of random media, this is called a model with renewal. Even if the rms curvature fluctuations are small, a sequence of contiguous intervals with positive curvature with a length sufficient to produce a conjugate point arises with a probability of unity on an infinitely long geodesic [14]. Obviously, nothing analogous arises in a strictly flat space.

Although Poisson random fields are very attractive from a probabilistic standpoint, they are not always consistent with observations. In particular, the hypothesis of Poisson fluctuations in the number of particles in the Universe, $\delta n \sim n^{1/2}$, leads to excessively large density fluctuations [13]. Nevertheless, in principle, observational and theoretical investigations into lensing due to curvature fluctuations open a path to go beyond the framework of the crystallographic approximation. Studies of such lensing are also of independent interest. A lens produced by curvature fluctuations differs from normal gravitational lenses in the absence of a lensing quasar or another massive body, and differs from ghosts in a glued-together world in its irregular position.

Limitations on the applicability of the crystallographic method are imposed not only by spatial but also by spatiotemporal curvature fluctuations. However, modern geometry has even less to say on this point than on the issue considered above.

Let us formulate our result in a positive way. There is some hope that studies of fluctuations in the microwave background aimed at determining the spatial topology of the Universe will enable us to go beyond the scope of the standard Friedmann cosmology. This path can be developed through studies of lenses that are not associated with a visible massive body, but are also not consistent with the predictions of crystallographic methods.

ACKNOWLEDGMENTS

This work was supported by the Russian Foundation for Basic Research, project no. 01-02-16158.

REFERENCES

1. M. Lachièze-Rey and J.-P. Luminet, Phys. Rep. **254**, 135 (1995).
2. D. D. Sokolov and V. F. Shvartsman, Zh. Éksp. Teor. Fiz. **66**, 412 (1974) [Sov. Phys. JETP **39**, 196 (1974)].
3. D. D. Sokolov and A. A. Starobinskiĭ, Astron. Zh. **52**, 1041 (1975) [Sov. Astron. **19**, 629 (1975)].
4. A. A. Starobinsky, Pis'ma Zh. Éksp. Teor. Fiz. **57**, 606 (1993) [JETP Lett. **57**, 622 (1993)].
5. J. R. Bond, D. Pogosyan, and T. Souradeep, Phys. Rev. D **62**, 043005 (2000); **62**, 043006 (2000).
6. H. Miur, New Sci., No. 2152, 28 (1998).
7. R. Lehoucd, J.-P. Uzan, and J.-P. Luminet, Astron. Astrophys. **363**, 1 (2000).
8. Ya. B. Zel'dovich and A. A. Starobinskiĭ, Pis'ma Astron. Zh. **10**, 135 (1984) [Sov. Astron. Lett. **10**, 135 (1984)].
9. N. J. Cornish and D. N. Sprengel, Phys. Rev. D **62**, 087304 (2000).
10. D. Gromoll, W. Klingenberg, and W. Meyer, *Riemannsche Geometrie in Grossen* (Springer-Verlag, Berlin, 1968; Mir, Moscow, 1971).
11. I. N. Bernshteĭn and V. F. Shvartsman, Zh. Éksp. Teor. Fiz. **79**, 1617 (1980) [Sov. Phys. JETP **52**, 814 (1980)].
12. Ya. B. Zel'dovich, Astron. Zh. **41**, 873 (1964) [Sov. Astron. **8**, 700 (1964)].
13. Ya. B. Zeldovich and I. D. Novikov, *Relativistic Astrophysics* (Nauka, Moscow, 1967; University of Chicago Press, Chicago, 1971), Vol. 1.
14. V. G. Lamburt, D. D. Sokolov, and V. N. Tutubalin, in *Mathematical Physics, Mathematical Simulation and Approximate Methods* (Obninsk, 2000), pp. 37–38.

Translated by A. Getling

Astronomy Reports, Vol. 46, No. 7, 2002, pp. 525–530. Translated from Astronomicheskiĭ Zhurnal, Vol. 79, No. 7, 2002, pp. 583–588.

Macromolecules in the Galaxy and the Cosmic Microwave Background

Yu. N. Pariĭskiĭ, N. N. Bursov, A. B. Berlin, N. A. Nizhel'skiĭ, A. V. Bogdantsov, and P. A. Tsybulev

Special Astrophysical Observatory, Russian Academy of Sciences, Nizhniĭ Arkhyz, Karachaevo-Cherkesskaya Republic, 357169 Russia

Received May 7, 2001

Abstract—A deep search for the predicted Galactic microwave dipole emission of spinning interstellar fullerene-type molecules has been conducted using the RATAN-600 radio telescope. This effect is of interest both in its own right and as a new form of Galactic screen between the cosmic microwave background (CMB) and the observer. The power of this noise component on angular scales of about 0.1° ($l = 1000$) is estimated. These scales are of primary interest for the "Cosmological Gene of the Universe" (RATAN-600), PLANCK Surveyor Mission, and other projects. At the frequencies of the expected emission peak of this dust component, the small-scale noise is a factor of 20 weaker than the predicted noise. It is shown that the role of this dust component is negligible, at least at the main PLANCK frequencies. The first estimates of the contribution from Galactic polarization noise are given for $\lambda = 3.9$ cm, where the theory predicts a maximum in the CMB polarization ($l \sim 1000$). At wavelengths of $\sim$1 cm and shorter, macromolecules contribute less than 1 μK, and should not hinder CMB polarization studies. Galactic synchrotron polarization, likewise, should not prevent CMB polarization experiments at the main PLANCK frequencies. © *2002 MAIK "Nauka/Interperiodica".*

1. INTRODUCTION

All modern physical and astrophysical schools place large hope in experiments on the anisotropy of the cosmic microwave background (CMB) of the Universe (see, for example, [1–5]). However, these experiments are very difficult, not only because of the special requirements of the techniques that must be used, but also in connection with a number of objective (natural) obstacles in realizing potential instruments.

In planned major spaceborne experiments such as MAP [2] and PLANCK [3], the limitations for scales of 1°–0.1° are the following:

– noise due to background radio sources (up to several mK),

– thermal emission of the Galaxy (up to 200 μK),

– synchrotron emission of the Galaxy (up to 200 μK),

– emission of dust in the Galaxy (0–1 mK).

This background emission must be isolated and removed, leaving only the CMB signal and instrumental noise. Numerous computer simulations of next-generation experiments show that this is in principle possible in multifrequency experiments (see, for example, [3, 6]). Many kinds of interfering noise have a Kolmogorov character, and their power drops off as $\sim l^{-3}$, so that the situation is eased for studies of small-scale anisotropy of the 3 K background. The "Cosmological Gene of the Universe" project [4, 5] focuses on the smallest scales ($l = 1000$), and we are systematically exploring all types of interference on precisely these poorly studied scales.

It is interesting that, whereas powerful sky (atmospheric) noise is added in ground-based experiments, the Earth is the main noise source in spaceborne COBE-type experiments [7].

We have studied the role of atmospheric noise in ground-based experiments with reflector radio telescopes in [5, 8]. The role of background sources in connection with high-resolution instruments is evaluated in [9], and the role of the synchrotron and thermal emission of the Galaxy in [5, 6]. The current paper is devoted to the contribution of a new powerful hypothetical noise component at centimeter wavelengths—the noise of macromolecules in the Galaxy. Interest in "macromolecular" dust has recently arisen in connection with the unexpected detected correlation between the COBE variations in the sky microwave brightness and the IRAS 100-μm data (not with H_α sky maps, as was expected). Furthermore, the centimeter-wavelength RING experiment [10] detected anomalously strong Galactic emission at 1 cm (about 100 μK on scales of about 14′). This is considerably greater than follows from the H_α data for an ionized gas with the usual temperature of 10 000 K.

1063-7729/02/4607-0525$22.00

The RING project observers have attempted to explain this effect as being due to a high temperature for the Galactic plasma ($T = 10^6$ K), which leads to energetic problems in the opinion of many researchers. The Princeton group has proposed an alternative explanation of the RING data based on new theoretical studies of the background radiation of macromolecules taking into account their bombardment by cosmic rays and photons. In particular, this work has considerably refined our understanding of effects connected with the ionization of macromolecules [11–16]; for earlier studies, see [17–21].

For a number of models of carbon macromolecules, the microwave dipole spectrum associated with their rotation has been calculated [11]. The peak frequency of this spectrum depends only weakly on the parameters of the macromolecules, and falls in the frequency range 20–30 GHz. The theory of magnetic dipole microwave emission by fine dust has also been developed, and its intensity can exceed the contribution of common dust by two orders of magnitude [9, 11]. The emission of such dust should have a considerable degree of polarization.

On the one hand, the possible presence of a new component of the Galactic microwave radiation stimulates interest in new methods for investigating the interstellar medium, the formation and destruction of macromolecules, their orientation and disorientation in magnetic fields and gas flows, etc. On the other hand, it could significantly limit the accuracy of measurements of the CMB anisotropy, and even dominate the CMB [11].

Therefore, we have carried out a series of targeted observations on the RATAN-600 radio telescope using centimeter-wavelength cryoradiometers, taking into account the predictions of modern theories [22, 23]. In the first series of observations, we focused on scales of special interest for the "Genetic Code of the Universe" experiment planned for RATAN-600 [4, 5] ($l > 1000$). These scales are central to studies of the CMB polarization and of numerous "secondary" anisotropy effects, including the role of the kinematic and thermal effects of scattering of CMB photons on evolving density and velocity inhomogeneities (these include the Sunyaev–Zel'dovich effect). The deepest estimates can be made precisely here in connection with the exponential decay of "Sakharov oscillations" on these scales. Another motive for new high-resolution observations is the RING experiment [10], which allows a "blue" spatial spectrum of "spinning" macromolecules that grows toward small scales [9].

In ground-based experiments with reflector radio telescopes, atmospheric noise is lower on small scales, and it is insignificant for RATAN-600 on scales at $l > 100$ [5, 8]. The limitations for higher values of l are due to a loss of thermodynamic equilibrium between the antenna temperature and brightness temperature when the scales for the studied inhomogeneities are considerably smaller than the telescope beam. It can be shown that, in our case, a compromise can be obtained on scales $800 < l < 1400$, or 0.1°.

2. OBSERVATIONS

The RATAN-600 observations were carried out near the zenith with the radio telescope beam fixed at the declination of the radio source 3C 84 ($\delta_{1950.0} = 41.2°$), which was used as a reference for the time pixel coordinates and signal amplitude. The emission was recorded using standard radiometers at 1.38, 2.7, 3.9, 7.6, 13, and 31 cm (and partially at 49 cm) with a time step of 0.1 s. In the absence of external interference, the fluctuation sensitivity of these radiometers is higher than 10 mK/s$^{1/2}$ at all centimeter wavelengths. The maximum sensitivity, 2 mK/s$^{1/2}$, was achieved at 7.6 cm. To use the filtering properties of the large RATAN-600 aperture (450 m), the radiometers were equipped with an internal reference load instead of a horn directed toward the celestial pole. Some of the observations recorded the linear polarization in various Stokes parameters. In this paper, we report the results of our observations of Stokes parameter I at 1.38 cm, where the radio emission of macromolecules is expected to dominate [11], and of the Stokes parameter Q at 3.9 cm, which corresponds to the predicted peak of the degree of polarization for emission by fine spinning dust [16]. The observations were conducted in 1998–2001.

3. INTENSITY OF THE RADIO EMISSION OF MACROMOLECULES

We were able to use more than 2000 h of observations in the indicated period, covering the right ascension interval of $0^h < \alpha < 23^h$ at the declination of 3C 84. The half-power beamwidth was about 5″ in right ascension and about 1′ in declination. Each one-hour record was first cleaned of features exceeding the noise dispersion by more than a factor of 2.6 and having angular sizes $< 1/l$ ($l = 1/\Theta$, where Θ is the studied angular scale of CMB inhomogeneities). Then, already in the Fourier domain, we cleaned the records of all kinds of noise outside the studied range of spatial frequencies (in our case, $l \sim 1000$, i.e., corresponding to timescales shorter than 16 s and longer than 32 s). We divided the entire data set (approximately 100 diurnal records) into two equal parts (*I*, *II*), and constructed simple daily averaged records for each part. We then plotted the amplitude distributions for the half-sums and half-differences of these

two groups. Both the half-sums and half-differences displayed normal distributions with nearly identical dispersions (S):

$$S_{(I+II)/2} = 201 \pm 1.9\ \mu\text{K},$$
$$S_{(I-II)/2} = 199 \pm 1.9\ \mu\text{K}.$$

The difference in the dispersions is comparable to the 1σ error of the mean and is not significant. The formal dispersion of a signal (of any nature) is

$$\delta T_{rms} = (S^2_{(I+II)/2} - S^2_{(I-II)/2})^{1/2} = 29\ \mu\text{K}$$

in terms of the antenna temperature, or approximately 60 μK in terms of the brightness temperature. Taking into account the data of [24], which show the presence of CMB noise with about 56 ± 7 μK on scales close to those studied by us but at wavelengths where the theory predicts the role of fullerenes to be small [11], we estimate the contribution of macromolecular dust to be <30 μK, instead of the expected 600 μK in the case [9] we are testing. This reduces the coefficients C_l of the Legendre polynomial for the dust by more than a factor of 100 compared to the pessimistic case [9] (Fig. 1).

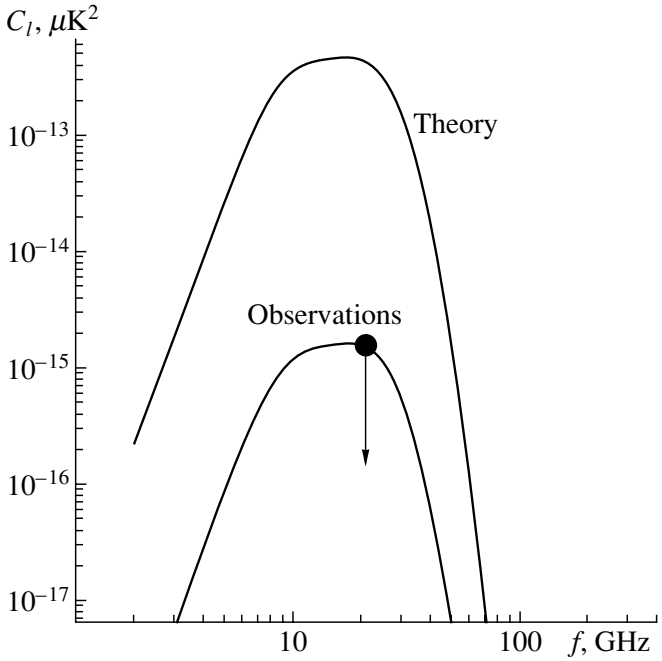

Fig. 1. Radio emission of macromolecules in the Galaxy: comparison of the theory [9] (upper curve) with the RATAN-600 observations. The lower curve has the theoretical shape, but is normalized to our observations.

4. FIRST ESTIMATES OF POLARIZATION OF DUST EMISSION AT RADIO WAVELENGTHS

The recent work of the Princeton group has shown that fine dust, which was not taken into account earlier in planning CMB experiments, may hinder measurements of both the intensity and polarization of the CMB. The predicted degree of polarization for fine spinning particles has a maximum value of 7% at 3–5 cm [16]. In our pessimistic case, this is about 50 μK at centimeter wavelengths on scales where the theory of the CMB predicts the maximum polarization ($l = 1000$, which corresponds to angular scales of 0.1° [22]).

Both the dipole and magnetic dipole emission of dust are polarized, but, in contrast to the CMB, the degree of polarization is a function of the emission frequency, which can enable us to separate the polarizations of dust and of the CMB [15].

We are carrying out a series of polarization observations of the high-latitude Galactic background radiation at 1.38, 3.9, and 13 cm. Here, we present preliminary results obtained for data taken up to the beginning of 2001 at 3.9 cm, where the maximum degree of polarization from fine spinning dust has been predicted [16]. We added a polarizer consisting of a low-loss ferrite modulator to the standard microwave channel at 3.9 cm, which enables us to measure the Stokes parameters Q or U as functions of the analyzer position. We have found that U is less sensitive to variations of the instrumental polarization, due mainly to radiation by the Earth between the secondary mirror and main surface of the RATAN-600 radio telescope. We selected about 30 diurnal records with satisfactory quality using the criterion of an absence of anomalous noise and various types of interference. As in the previous case, we divided the data into two groups of similar quality (I, II) and created datasets with the half-sums and half-differences of these two groups. We divided each hour of right ascension into four-minute intervals, for each of which we calculated the dispersions after removing a linear trend. We then calculated the mean dispersions for each hour separately for the half-sums and half-differences of the groups. Further, we determined the dispersions (S) averaged over 24 h with the two extreme values (the largest and smallest) excluded. This yielded the values

$$S_{(I+II)/2} = 61.9 \pm 5\ \mu\text{K},$$
$$S_{(I-II)/2} = 62.6 \pm 2\ \mu\text{K}.$$

Thus, we obtained the upper limit

$$\delta T^p_{rms} = ((S_{(I+II)/2})^2 - (S_{(I-II)/2})^2)^{1/2} = 4.97 \pm 10\ \mu\text{K}$$

in terms of the antenna temperature, or 10 μK in terms of the brightness temperature.

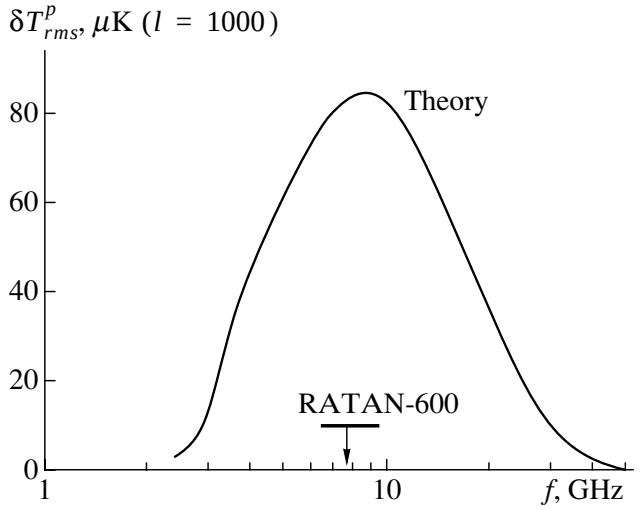

Fig. 2. Polarization of fine dust at radio wavelengths. The curve shows the prediction of the theory [16] for the pessimistic case [9]. The RATAN-600 7.7-GHz upper limit is shown by the horizontal bar.

We consider this value to be a 1σ upper limit at 3.9 cm for a scale corresponding to $l = 1000$.

Figure 2 shows that this limit is considerably lower than the value of 50 μK predicted by the pessimistic case [9], which can obviously be rejected. Even this estimate is sufficient to conclude that neither electric dipole nor magnetic dipole radiation is the main obstacle in studies of the CMB polarization, at least on small scales. Indeed, taking into account the frequency dependence of the degree of polarization predicted by the Princeton group [16, Fig. 1], the Galactic dust component is unlikely to be strong enough to hinder studies of the scalar polarization of the CMB on scales near $l = 1000$, even at 1 cm. In particular, the degree of polarization drops to 1% at 1 cm (30 GHz). For our upper limit of 20 μK, the amplitude of the polarized signal from the spinning molecules should be less than 1 μK.

This limit has no relation to estimates of the role of polarized magnetic dipole emission at frequencies much higher than 30 GHz, where the degree of polarization for magnetized particles can be large and reach 40%. Nevertheless, we should not forget that our estimates also represent a strict upper limit for the synchrotron component of the polarized Galactic radiation on the scales studied. The higher the observing frequency, the stricter the limitations. For the main frequencies of the PLANCK project (143–217 GHz), at which the maximum number of high-sensitivity bolometers will operate, our limit will be 0.01 μK.

It is useful to compare the RATAN-600 data with the deepest statistical studies of variations of the polarization of the background Galactic radiation based on the new surveys at 21, 13, and 11 cm [25]. First and foremost, the theory does not predict an appreciable contribution from emission by macromolecules, much less common dust, at decimeter wavelengths. In principle, our data at short centimeter wavelengths yield completely independent information about background radiation of a different nature, and a direct comparison is not meaningful. Furthermore, the RATAN-600 data correspond to smaller scales, down to $l = 2000$ (compared to $100 < l < 800$ in [25]). Finally, almost all the decimeter-wavelength data have been obtained for areas of sky near the Milky Way ($b < 10°$), while the RATAN-600 data were obtained at high latitudes (up to $b = 70°$), which are of the most interest for CMB anisotropy experiments. It is interesting that Baccigapuli *et al.* [25] found no large difference between new low-latitude data and old high-latitude data [26], at least for $10 < l < 200$. The extrapolation to small scales and high frequencies recommended in [25],

$$C_l^p = (4 \pm 3) \times 10^{-7} \times (l/50)^{-2.9} \times (f/2.4\ \mathrm{GHz})^{-5.8}\mathrm{K}^2,$$

should yield at 7.7 GHz (3.9 cm) and $l = 1000$

$$C_l^p(l = 1000, f = 7.7\ \mathrm{GHz}) = (7.8 \pm 5.8) \times 10^{-14}\ \mathrm{K}^2,$$

which corresponds to

$$(\delta T^p_{rms})^2 = C_l^p \times (l+1) \times l/2\pi = (1.24 \pm 0.9) \times 10^{-8}\ \mathrm{K}^2$$

or

$$\delta T^p_{rms} = 111\ \mu\mathrm{K}.$$

At the same time, we have found that

$$\delta T^p_{rms} = 4.97 \pm 10\ \mu\mathrm{K},$$

which is a factor of 20 smaller than predicted in [25]. This difference will become a factor of 400 in the power spectrum. However, taking the uncertainties into account could bring the results into agreement, since the data of [25] allow values in the interval (at the 1σ level)

$$11.8 < \delta T_l^p < 368\ \mu\mathrm{K}.$$

Thus, our estimate is useful, not only for elucidating the contribution of dust emission at radio frequencies, but also for obtaining more precise estimates of the small-scale polarization noise of the synchrotron component of the Galaxy. Note that our earlier estimate of the small-scale noise of the synchrotron emission of the Galaxy at 7.6 cm (less than 50 μK on scales $l = 200$–500 [4]) yields a value for the polarization noise that is a factor of 50 smaller than the

extrapolated value from [25] if we assume that the degree of polarization allowed by the theory is $< 75\%$. Our upper limit on the sky polarization on scales $l = 2000$ is closest to the data of [27, 28], obtained at 1 cm but with a resolution a factor of 20 lower (1.4°).

5. CONCLUSIONS

(1) We have carried out the deepest studies of the contribution of macromolecular dust to the high-latitude background radiation of the Galaxy at the frequency of the predicted radio peak of dust dipole emission (20–30 GHz) on angular scales of about 0.1°, especially important for new-generation experiments on the CMB anisotropy.

(2) The power of this emission is more than a factor of 100 lower than the pessimistic case proposed by the PLANCK group for $l = 1000$ [9], and this case need not be considered further.

(3) Our upper limit on the dust radio emission (< 30 μK) suggests that the effect of fine spinning dust is negligible at the main PLANCK frequencies (above 30 GHz). Further accumulation of data will enable us to make deeper estimates.

(4) Our upper limit is almost a factor of two lower than the data of the RING experiment. This discrepancy could be associated with features of the circumpolar area studied in the RING experiment, or with the higher angular resolution of our experiment ($800 < l < 2000$ in our observations and $l \leq 620$ in the RING experiment).

(5) A comparison with new decimeter-wavelength observations of the polarization of the Galaxy (see [25] and references therein) has shown that it is difficult to extrapolate high-latitude decimeter-wavelength data on polarization noise associated with synchrotron emission to shorter wavelengths and small scales ($l \gg 100$). Direct estimates at frequencies and scales closer to the main parameters of CMB polarization experiments are required. For the time being, we assume that the detected difference is most likely associated with the presence of a more uniform magnetic field at high latitudes and possibly with the disappearance of Faraday structures (see. [25, 29]).

(6) The available data on Galactic background emission provide hope that there exists a transparent window in the Galaxy in the scale–frequency plane where the achievable depth of observations depends only on the sensitivity of the receivers used. The polarization of the Galaxy does not pose a threat for next-generation experiments with μ Kelvin sensitivities.

ACKNOWLEDGMENTS

This work was supported by INTAS, grant 97-1192; COSMION; Integration; and the Russian Foundation for Basic Research, project no. 99-02-17114.

REFERENCES

1. M. Bersanelli, F. Boushet, G. Efstathiou, *et al.*, ESA D/SCI(96)3 (February, 1996), COBRAS/SAMBA Report on the Phase A Study ("Red Book").
2. http://map.gsfc.nasa.gov.
3. http://astro.estec.esa.nl/SA-general/Projects/-Planck.
4. Cosmological Gene: http://www.sao.ru/Projects; www.brown.west.nw.ru.
5. Y. Parijski, Astron. Astrophys. Trans. **19** (3–4), 265 (2000).
6. A. V. Chepurnov, Candidate's Dissertation in Physics and Mathematics (Spets. Astrofiz. Obs. Ross. Akad. Nauk, Nizhniĭ Arkhyz, 1996).
7. G. Smooth, *2nd Course in Current Topics in Astrofundamental Physics,* Ed. by N. Sánchez, *et al.* (1993), p. 125.
8. Y. Parijskij and P. Tsibulev, Astron. Astrophys. Trans. **19** (3–4), 287 (2000).
9. M. Tegmark, D. Eisestein, W. Hu, and A. de Oliveira-Costa, astro-ph/9905257 (1999).
10. E. M. Leitch, A. C. Readhead, T. M. Pearson, and S. T. Myers, Astrophys. J. **486**, L23 (1997).
11. B. T. Draine and A. Lazarian, Astrophys. J. **494**, L19 (1998).
12. B. T. Draine and A. Lazarian, Astrophys. J. **508**, 157 (1998).
13. B. T. Draine and A. Lazarian, Astrophys. J. **512**, 740 (1999).
14. B. T. Draine and A. Lazarian, astro-ph/9902356 (1999).
15. A. Lazarian, astro-ph/0101001 (2000).
16. A. Lazarian and B. T. Draine, astro-ph/0003312 (2000).
17. S. A. Kaplan and S. B. Pikel'ner, *The Interstellar Medium* (Fizmatgiz, Moscow, 1963; Harvard Univ. Press, Cambridge, 1970).
18. Yu. N. Gnedin, A. Z. Dolginov, and N. A. Silant'ev, Astron. Zh. **49**, 85 (1972) [Sov. Astron. **16**, 64 (1972)].
19. Yu. N. Gnedin and I. G. Mitrofanov, in *Early Stages of Stellar Evolution* [in Russian], Ed. by I. G. Kolesnikov (Naukova Dumka, Kiev, 1977).
20. D. R. Huffman, Adv. Phys. **26**, 129 (1977).
21. A. E. Douglas, Nature **269**, 130 (1977).

22. W. Hu and M. White, New Astron. **2** (4), 323 (1997).
23. D. Eisenstein, W. Hu, and M. Tegmark, Astrophys. J. **518**, 2 (1999); astro-ph/9807130 (1998).
24. A. T. Lee, P. Ade, A. Balbi, *et al.*, astro-ph/0104459 (2001).
25. C. Baccigapuli, C. Burigana, F. Perotta, *et al.*, astro-ph/0009135 (2001); Astron. Astrophys. (in press).
26. W. N. Brouw and T. A. T. Spoelstra, Astron. Astrophys., Suppl. Ser. **26**, 129 (1976).
27. E. J. Wollack, Astrophys. J. **419**, L49 (1993).
28. C. B. Netterfield, *et al.*, Astrophys. J. **445**, L69 (1995).
29. R. D. Davies and A. Wilkinson, in *Microwave Foregrounds,* Ed. by A. de Olivera-Costa and M. Tegmark, Astron. Soc. Pac. Conf. Ser. **181**, 77 (1999).

Translated by G. Rudnitskiĭ

Astronomy Reports, Vol. 46, No. 7, 2002, pp. 531–542. Translated from Astronomicheskiĭ Zhurnal, Vol. 79, No. 7, 2002, pp. 589–600.

Color Redshifts and the Age of the Stellar Population of Distant RC Radio Galaxies

O. V. Verkhodanov[1], A. I. Kopylov[1], Yu. N. Pariĭskiĭ[1], N. S. Soboleva[2], A. V. Temirova[2], and O. P. Zhelenkova[1]

[1] *Special Astrophysical Observatory, Nizhniĭ Arkhyz, Karachaevo-Cherkesskaya Republic, 357169 Russia*

[2] *St. Petersburg Branch of the Special Astrophysical Observatory, St. Petersburg, Russia*

Received May 18, 2001

Abstract—$BVRI$ data are presented for the majority of steep-spectrum objects in the RC catalog with $m_R < 23.5^m$. Previously developed programs are applied to these data to estimate the redshifts and ages of the stellar systems of the host galaxies. Applying this program to the color data ($BVRIJHK$) for distant radio galaxies with spectroscopic redshifts indicates that this approach provides accurate estimates of the redshifts of such radio galaxies, close to those obtained using field galaxies ($\sim 20\%$). The age estimates are much less trustworthy, but a lower limit to the ages of objects that are not very distant ($z < 1.5$) can be determined with certainty. We have identified several galaxies whose formal ages exceed the age of the Universe at the corresponding z in simple Cold Dark Matter models for the Universe. The possibility of using such objects to elucidate the role of "dark energy" is discussed. This paradox disappears in models with cosmological constants (Λ terms) equal to 0.6–0.8. © *2002 MAIK "Nauka/Interperiodica"*.

1. INTRODUCTION

Currently available astronomical instruments are capable of tracing the population of powerful radio galaxies out to virtually any distance, making it possible to study the radio evolution of this population from the time of its origin to the present. However, finding new objects at $z > 3$ requires considerable effort and the application of strict selection criteria based on radio, optical and infrared properties, which results in samples whose representativeness is difficult to characterize.

The population of extremely powerful FRII radio galaxies is believed to be associated with giant ellipticals harboring supermassive ($\sim 10^9 M_\odot$) black holes at their centers, so that the evolution of this population is related to the formation of the largest stellar systems and the evolution of massive black holes. Moreover, these objects are often associated with clusters and groups of galaxies, and may be indicators of distant clusters forming in nodes of the large-scale structure. Finally, there have been a number of suggestions about ways to use these objects to estimate the parameters of the surrounding medium and even the geometry and dynamics of the Universe [1, 2].

In contrast to quasars, radio galaxies admit a detailed analysis of their stellar populations. As a rule, the optical and near-IR spectra of these objects at redshifts $z < 1$–1.5 are dominated by their stellar and not their gaseous component. This makes it feasible to attempt to use stellar-evolution and population-synthesis methods to determine "color" redshifts, and even the ages of the stellar populations of these galaxies. If successful, such analyses can yield estimates of the time of (at least the last) episode of massive star formation.

According to generally accepted unified schemes for active objects, FRII radio galaxies differ from quasars, BL Lac objects, and other active galactic nuclei only in the angle between the line of sight and the rotational axis of a gas and dust torus screening the accretion disk surrounding the black hole, and data about their evolution can also be applied to other classes of objects.

Finally, powerful galaxies with active nuclei (radio galaxies and quasars, primarily radio-quiet quasars) are important sources of UV radiation in the Universe. Together with the integrated optical depth to Thomson scattering of the 3 K cosmic background photons, data for such galaxies can be used to refine estimates of the epoch of secondary ionization of the Universe.

Deep optical studies of the host galaxies of these radio sources are made difficult by the fact that their spatial density is five to six orders of magnitude lower than the density of foreground galaxies, so that they are essentially absent from small, deep fields. For example, only one intermediate-power distant ($z = 4.42$) radio galaxy has been found in the Hubble Deep Field. Therefore, sampling of fields for such studies

1063-7729/02/4607-0531$22.00

Table 1. Photometric bands

Filter	λ_{eff}, Å	$A/E(B-V)$	C
Landolt B	4400	4.315	3.620
Landolt V	5500	3.315	3.564
Landolt R	6500	2.673	3.487
Landolt I	8000	1.940	3.388

should begin with a preliminary selection based on radio data and applying all possible indirect criteria. The principles for the selection of distant-object candidates in the "Large Trio" program [3–5] are similar to generally adopted ones [6].

Obtaining quality spectroscopic data for distant, faint galaxies and radio galaxies is very resource intensive, necessitating searches for relatively simple, indirect methods for the determination of the redshifts and other characteristics of these objects. In the case of powerful radio galaxies, even photometric estimates proved to be useful and have been widely employed [6–8].

In recent years, in addition to photometric redshift-estimation methods, color data for faint galaxies have been used, and this approach has formed the basis for a number of major projects (see, e.g., [9]). As we pointed out above, the colors of stellar systems can also be used to estimate their ages. Strictly speaking, a special analysis is needed to determine whether color data can be used for the population of powerful radio galaxies, since the color manifestations of the nuclear activity in these objects are not clearly understood. Color parameters can also be affected by sites of "secondary" star formation.

This work continues our program aimed at using multicolor data to estimate the color redshifts and ages of the stellar systems of host galaxies. The use of these data has become almost inevitable. Until recently, direct mass spectroscopy of faint objects with the 6-m telescope of the Special Astronophysical Observatory required too much observing time to study objects fainter than 20^m. For example, in 1995–1996, we were able to measure the spectroscopic redshifts of only four bright objects (three quasars and a galaxy, all of them brighter than $m_R = 20.5^m$) and one faint galaxy ($m_R = 23^m$) [10], with this last redshift ($z = 2.73$) being determined from only one emission line. This result is independently corroborated by our color data: the negative color index $B-V$ agrees with our identification of this line as Ly_α, which is characteristic of distant radio galaxies.

Recent commissioning of more efficient instruments at the Special Astrophysical Observatory promises substantial improvements in faint-object spectroscopy on the 6-m telescope. In March 2001, the new SCORPIO instrument [11] mounted on the 6-m telescope was used to take the spectra of two more objects: the radio galaxy 0908+0451 and quasar 1154+0431. The spectroscopic redshift of the radio galaxy was virtually identical to the color redshift. Color redshift data will help improve the efficiency of spectroscopic observations.

In the next section, we report the results of $BVRI$ photometry. We then describe the technique used to determine the color redshifts and ages of the stellar systems from their $BVRI$ colors using modern evolutionary models for their spectral energy distribution (SEDs). In the following sections, we discuss our results, model-dependent differences between the redshift and age estimates, and the reliability of the results. We also suggest further steps toward improving the accuracy of the estimates.

2. MULTICOLOR PHOTOMETRY OF RC OBJECTS

$BVRI$ color data have now been obtained for 60 objects (radio galaxies and quasars) from the RC catalog [12, 13] using the 6-m telescope of the Special Astrophysical Observatory. We here report our photometric results for 50 radio galaxies based on observational data collected in 1994–1998. The 1994–1995 observations used an ISD015A 580×520 CCD with a pixel size of $0.205'' \times 0.154''$, while the 1996–1998 observations used an ISD017A 1160×1040 CCD with a pixel size of $0.137'' \times 0.137''$. In the latter case, we coadded the initial pixels into double-sized elements in both coordinates. The exposure times were determined during the observations based on the brightness and color of each object and ranged from a total of 1200–1800 s in the B filter to 400–800 s in the R filter for a typical object in our sample with $R = 22^m$–23^m. We chose the exposures to ensure that the resulting signal-to-noise ratios were no lower than four to five in all filters. We had to increase the exposure times by a factor of 1.5–2 when seeing was poorer than $2''$.

We reduced the frames in the standard way using the MIDAS package by performing a mean dark-frame subtraction and pixel-by-pixel sensitivity correction based on frames of the twilight sky. We eliminated the residual nonuniform background in the I filter due to bright night-sky emission lines by subtracting the median sum of all the program frames for a given night or for several nights within a single observing session. We translated our photometric measurements into the standard Johnson–Cousins system using standard stars from the list [14], which we observed several times during the night. The photometric measurements of a given object were made

using a circular aperture of the same size in all filters, which ranged from $3''$ to $12''$ depending on the magnitude of the object. The typical aperture size was $4''-5''$. We measured the background in an annular aperture with a sufficiently large radius to exclude the light from the outermost regions of the object studied. When required, we eliminated the contribution of nearby objects by interpolating the surrounding background. The photometric errors were usually $0\overset{m}{.}1$ or better for galaxies brighter than 21^m, increasing to $0\overset{m}{.}2 - 0\overset{m}{.}25$ for $23^m - 24^m$ galaxies and to $0\overset{m}{.}3 - 0\overset{m}{.}5$ for galaxies fainter than $25^m - 25\overset{m}{.}5$.

We performed the extinction corrections using the "Maps of Dust IR Emission for Use in Estimation of Reddening and CMBR Foregrounds" [15] recorded as FITS files. We converted the magnitudes into fluxes using the formula $S(\mathrm{Jy}) = 10^{C-0.4m}$ [16].

Table 1 gives the constants C for the filters together with the name of the filter, its wavelength, and the total/selective extinction ratio $A/E(B-V)$ assuming an extinction curve with $R_V = 3.1$. Table 2 gives the extinction-corrected magnitudes for the radio galaxies in our sample in the four filters.

3. MODELS OF THE SED OF THE HOST GALAXIES

Attempts were made to use the colors of radio galaxies to estimate the redshifts and ages of the stellar systems of their host galaxies in the late 1980s and early 1990s. Numerous evolutionary models were developed and compared to the observational data, yielding discrepancies in results [4, 17–20].

Attempts have been made to remove the inadequacies of previous versions of the PEGASE (Project d'Etude des Galaxies par Synthese Evolutive) [21] and GISSEL'98 [22, 23] models, which have been widely used in recent years.

In the Large Trio experiment [4], we attempted to apply these methods to distant RC objects with steep spectra for which we had measured $BVRI$ colors. Compared to [4], the current paper is based on more reliable identifications, new photometric measurements, new models for the galaxy SEDs, and the application of smoothing procedures (convolving the SEDs with the transmission curve for the corresponding filter while taking into account the object's redshift).

We have also investigated the applicability of these new models to the population of distant ($z > 1$) radio galaxies with known redshifts for which we could find reasonably trustworthy published optical and near-IR photometry in at least three filters [24, 25].

One of our SED models was the evolutionary PEGASE model [21] for Hubble-sequence galaxies that are both undergoing starbursts and evolving passively. The main new feature of this model is its extension of the atlas of synthetic spectra [26] toward the near infrared using a revised stellar library including the parameters of cold stars. The model covers the wavelength interval from 220 Å to 5 μm. According to [21], the algorithm used in the model makes it possible to trace phases of rapid evolution, such as the red-supergiant and AGB phases, in the near infrared. We used an extensive set of SED curves for this model covering ages from 7×10^6 to 19×10^9 yr for massive elliptical galaxies.

We used the new GISSEL'98 model with a library of synthetic spectra for elliptical galaxies adopted from [23], based on the evolutionary models of [22, 27]. The library of elliptical-galaxy synthetic spectra was constructed for the case of a simple stellar population, a starburst duration of 1 Gyr, and exponentially decaying starburst activity.

We assumed that the stars had solar metallicity and adopted the initial mass function of Miller and Scalo [28] with an upper mass limit of 125 $M_\odot$. Bolzonella *et al.* [23] have shown that the choice of the initial mass function does not influence the accuracy of the derived redshifts. We computed model tracks in the wavelength interval from 200 to 95 800 Å by using the interval specified by redshifts from zero to six. The sets of evolutionary models we used are available at http://sed.sao.ru [29].

4. FITTING PROCEDURE

Before using the model curves, we smoothed them using the algorithm

$$S_{ik} = \frac{\sum\limits_{j=0}^{n} s_{i-n/2+j} f_{jk}(z)}{\sum\limits_{j=0}^{n} f_{jk}(z)},$$

where s_i is the unknown model SED curve, S_{ik} is the model SED curve smoothed by the kth filter, $f_k(z)$ is the energy distribution in the kth filter "compressed" by a factor of $1+z$ along the wavelength axis of the SED curve, and $j = 1, n$ is the index of the pixel number in the filter transmission curve. We used the set of k (four for the RC objects) curves constructed in this way to build a two-dimensional array of smoothed spectra for use in the subsequent computations.

We estimated the ages and redshifts of the radio galaxies by choosing the optimal match between the measured multi-color photometric data points and the SED curves, using tabulated SED curves computed for various ages. The fitting algorithm can be described briefly as follows [30]. We shifted the data

Table 2. Extinction-corrected colors

Source	B	V	R	I	Source	B	V	R	I
0015+0503a	$23^m.89$	$22^m.97$	$22^m.20$	$21^m.36$	1152+0449	$23^m.86$	$23^m.66$	$22^m.39$	$21^m.00$
0015+0501	24.82	23.91	23.37	22.22	1155+0444	21.36	19.83	18.90	18.20
0034+0513	25.28	24.79	23.25	21.79	1213+0500	23.55	22.90	22.04	21.32
0038+0449	21.90	21.46	21.38	20.52	1235+0435b	24.15	22.81	21.59	20.35
0039+0454	24.81	24.00	22.69	21.22	1322+0449	23.68	22.52	20.77	19.17
0105+0501	24.00	22.48	22.78	22.43	1333+0452	24.87	24.44	23.56	22.46
0135+0450	20.49	19.16	18.42	17.82	1339+0445	25.05	23.72	22.70	21.55
0152+0453	23.31	23.02	22.47	21.70	1357+0453	22.98	21.85	21.10	20.11
0159+0448	22.65	21.72	21.23	20.65	1429+0501	25.57	23.24	21.64	20.50
0209+0501a	20.37	19.19	18.43	17.78	1436+0501	23.90	23.86	23.39	22.70
0209+0501b	25.72	24.09	23.12	21.63	1446+0507	21.48	20.03	19.17	18.54
0318+0456	23.80	23.13	23.11	22.80	1503+0456	24.02	23.67	23.14	22.24
0444+0501	23.48	23.70	23.33	23.13	1510+0438	24.98	23.73	22.57	21.25
0457+0452	22.01	20.86	20.05	19.37	1551+0458	25.57	25.34	24.43	23.30
0836+0511	23.68	23.53	23.09	22.44	1626+0448	22.32	23.07	22.73	22.63
0837+0446	23.03	23.29	22.99	22.11	1638+0450	22.86	22.33	22.14	21.04
0845+0444	24.72	22.42	21.09	19.77	1646+0501	24.01	22.44	20.97	19.76
0908+0451	21.63	20.72	19.85	19.07	1703+0502	24.22	23.39	23.12	22.26
0909+0445	22.60	21.53	20.50	19.59	1706+0502	24.73	24.19	23.25	21.88
0934+0505	25.29	24.45	24.67	23.61	1722+0442	22.30	21.59	20.63	19.44
1011+0502	23.71	23.18	22.47	22.60	2029+0456	22.85	22.24	21.66	20.53
1031+0443	23.93	22.79	22.09	20.85	2219+0458	24.80	25.03	23.72	22.25
1043+0443	23.98	23.57	22.51	21.70	2224+0513	23.16	22.31	21.43	20.32
1124+0456	20.30	18.79	17.85	17.07	2247+0507	23.64	23.18	22.53	21.43
1142+0455	24.83	22.53	21.38	20.39	2348+0507	23.89	23.79	23.56	23.08

points along and across the SED curves to determine the position minimizing the sum of the squared residuals of the data points from the smoothed curves; i.e., we minimized χ^2:

$$\chi^2 = \sum_{k=1}^{N} \left(\frac{F_{\mathrm{obs},k} - p \cdot \mathrm{SED}_k(z)}{\sigma_k} \right)^2,$$

where $F_{obs,k}$ is the observed magnitude in the kth filter, $\mathrm{SED}_k(z)$ is the model magnitude for a given SED in the kth filter at a given z, p is a free coefficient, σ_k is the measurement error, and N is the number of filters.

We estimated the redshift of a galaxy by determining the shift of the optimal filter positions on the SED curve relative to their positions for $z = 0$. From the entire set of curves for various ages, we selected the

curve yielding the minimum sum of squared residuals for each radio galaxy.

5. PHOTOMETRIC REDSHIFTS FOR THE RC RADIO GALAXIES

To investigate the potential of using multicolor photometry to derive the redshifts and stellar-population ages of radio galaxies, we found about 40 distant radio galaxies with known redshifts and published magnitudes in at least three filters [31]. The published photometric data are very inhomogeneous and consist of observations made by different authors using different instruments, filters, and calibrations, with the same object sometimes being observed with different apertures, etc. Subsamples of objects for which relatively homogeneous data are available (e.g. those from the 3C, 4C, and B2 catalogs) are too small to be statistically compared.

We first used the collected photometric data and the PEGASE and GISSEL'98 models to determine the ages of the stellar populations of the galaxies at a specified known redshift. We then searched for the optimum model to reproduce both the redshift and age of the stellar population, and compared the results obtained. In this way, we estimated the age and redshift of the galaxy in the framework of these models (see also [32], [33]).

It is evident from general considerations that the stability of the results for large redshifts depends substantially on the availability of infrared data (up to the K band), since the fitting process can "grab onto" the jump at the leading edge of the optical SED, enabling a reliable determination of the best-fit position of the data (there will be a conspicuous maximum in the likelihood curve). We tested the stability of the algorithm by repeating our analysis excluding some of the data so that only three points were left, one of them in the K band; this yielded the same results for the residual curve as those obtained using four or five points. However, the results obtained without the use of IR photometric data are much more uncertain.

However, we showed earlier [24, 25] that an analysis with four closely spaced filters (as in our $BVRI$ photometry) yielded good results for a control sample of six objects, in agreement with the results obtained using all filters, including infrared photometric data.

We used our technique to compute the redshifts and stellar-population ages for the objects in our sample based on our four-color ($BVRI$) photometry. The results are summarized in Table 3. The columns give (1) the IAU name of the RC radio source (epoch 2000), (2)–(5) the color redshift (z_c), age of the stellar population (t) in Myr, sum of squared residuals (ϵ^2), and age of the Universe (T) at the given z in Myr for the GISSEL'98 model, and (6)–(10) the corresponding parameters for the PEGASE model. The asterisks indicate what we believe to be the most likely redshifts and ages for the objects (see comments in Table 3).

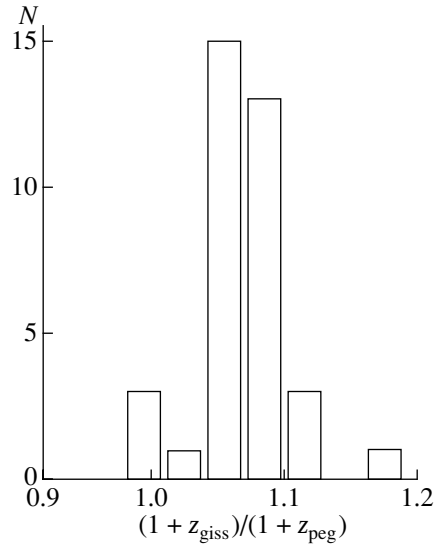

Fig. 1. Histogram of the ratio of the redshifts obtained using the GISSEL'98 (z_{giss}) and PEGASE (z_{peg}) models. We show the central part of the histogram accounting for 80% of all the objects.

6. DISCUSSION OF RESULTS

(1) The color redshifts of distant radio galaxies.

We showed earlier [24, 25] that the PEGASE model yielded satisfactory results for 40 objects with directly measured redshifts. Table 3 shows that, as a rule, the results given by the new GISSEL'98 model differ little from those derived for the PEGASE model (see also [36, 37]). Figure 1 shows a histogram of the ratio $(1 + z_{giss})/(1 + z_{peg})$.

The error distribution is not normal, and has a core with very small model errors that includes most (80%) of the objects; however, the errors for the remaining 20% of the sources are very large. A more detailed analysis of the data usually reveals a likely origin for these large errors, which can be divided into three categories: (1) one of the filters contains a strong (Ly_α) line, (2) the filters are contaminated by the light of a nearby bright object, or (3) complex cases when the SED deviates from the adopted model. A number of such cases are described in the comments in Table 3.

Note that we used the standard ($BVRI$) filter set for the 6-m telescope, which is known to yield satisfactory results for objects that are not too distant (precisely those whose colors we have measured so far). It would be desirable to expand the wavelength

Table 3. Color redshifts and stellar-population ages

Source	GISSEL'98				PEGASE			
	z_c	t, Myr	ε^2	T, Myr	z_c	t, Myr	ε^2	T, Myr
0015+0503a	4.91	16000	0.0212	1293	0.08	19000	0.035	13386
	0.47	3250	0.0308	8462	0.73	1000	0.040	7664
0015+0501	0.86	3250	0.0358	6953	0.81	1000	0.035	7214
0034+0513	1.10	15000	0.0172	5884				
	1.10	5000	0.0348	5884				
0038+0449	1.79	4000	0.0177	3925	1.73	1200	0.019	4051
0039+9454	0.99	7250	0.0083	6340	0.95	18000	0.037	6519
0105+0501	4.26	9250	0.0850	1539	0.28	500	0.086	11204
0135+0450	0.10	15750	0.0022	13317	0.12	19000	0.008	13056
	0.10	8750	0.0031	13317	0.34	3000	0.010	10607
0152+0453	0.81	905	0.0019	7214	0.75	450	0.008	7547
0159+0448	0.02	6500	0.0030	14440	0.09	4000	0.008	13451
	0.41	2100	0.0127	9967				
0209+0501a	0.38	3750	0.0066	10234	0.38	2500	0.006	10234
0209+0601b	0.72	6250	0.0461	7723	0.69	16000	0.047	7905
0318+0456	0.28	719	0.0123	11204	0.20	500	0.016	12080
	3.28	286	0.0187	2092				
0444+0501	1.27	509	0.0349	5275	1.21	350	0.030	5478
	2.35	3000	0.0502	3005				
0457+0452	0.41	4500	0.0045	9967	0.38	3000	0.011	10234
0836+0511	0.81	360	0.0064	7214	1.16	700	0.005	5657
	1.21	2200	0.0085	5478	1.34	900	0.007	5053
	1.36	2000	0.0074	4993	1.93	2500	0.027	3656
0837+0446	0.98	203	0.0469	6384	0.96	200	0.044	6474
	1.92	9250	0.0575	3674	1.91	14000	0.059	3692
0845+0444	0.66	9000	0.0529	8093	5.29	15000	0.116	1178
0908+0451	0.48	3500	0.0201	9382	0.49	1600	0.029	9302
0909+0445	0.64	4250	0.0126	8223	0.64	2500	0.014	8223
0934+0505	1.78	4250	0.0725	3946	1.68	1400	0.081	4161
1011+0502	0.51	453	0.0599	9147	0.46	350	0.048	9544
1031+0443	0.86	4250	0.0243	6953	0.75	2000	0.018	7547
1043+0443	1.21	4750	0.0164	5478	1.14	3000	0.014	5731

Table 3. (Contd.)

Source	GISSEL'98				PEGASE			
	z_c	t, Myr	ε^2	T, Myr	z_c	t, Myr	ε^2	T, Myr
1124+0456	0.36	5750	0.0160	10418	0.35	13000	0.005	10512
1142+0455	4.99	509	0.0383	1267	4.95	≤ 200	> 0.115	1280
	0.36	14000	0.0471	10418				
1152+0449	1.32	8000	0.0083	5115	1.17	17000	0.064	5621
1155+0444	0.33	5750	0.0190	10703	0.35	1000	0.009	10512
1213+0500	5.15	15500	0.0111	1218	0.70	700	0.021	7843
	0.70	2200	0.0164	7843				
1235+0435b	0.68	5750	0.0125	7967	0.64	12000	0.008	8223
1322+0449	0.99	12750	0.0082	6340				
	0.76	7250	0.0724	7490				
1333+0452	1.06	4000	0.0073	6044	1.03	1600	0.017	6168
1330+0445	0.73	5250	0.0149	7664	0.67	4500	0.022	8030
1357+0453	0.38	5000	0.0424	10234	0.72	1600	0.039	7723
	0.72	3500	0.0481	7723				
1429+0501	0.63	11250	0.0477	8289	5.29	450	0.083	1178
1436+0501	1.18	2100	0.0100	5585	1.37	900	0.013	4963
	1.35	2750	0.0102	5023	1.96	3000	0.034	3787
1446+0507	4.99	6500	0.0178	1267	0.35	7000	0.012	10512
	0.27	5750	0.0211	11309				
1503+0456	0.84	1434	0.0017	7056	0.77	500	0.008	7434
1510+0438	0.70	5750	0.0071	7843	0.66	11000	0.006	8093
1551+0458	1.32	16000	0.0160	5115				
	1.32	5250	0.0237	5115				
	1.06	4000	0.0308	6044				
1626+0448	0.03	203	0.1132	14293	0.04	200	0.111	14147
	2.30	3000	0.1613	3072	2.31	≥ 1000	< 0.165	3058
1638+0450	1.74	5000	0.0222	4030	0.84	600	0.032	7056
	0.89	1680	0.0416	6804	1.57	2000	0.039	4420
1646+0501	0.64	7250	0.0070	8223	0.64	> 5000	< 0.147	8223
1703+0502	0.00	7000	0.0375	14742	0.07	6000	0.045	13723
	0.37	1680	0.0682	10326	0.81	800	0.069	7214
	3.71	571	0.0792	1814				

Table 3. (Contd.)

Source	GISSEL'98				PEGASE			
	z_c	t, Myr	ε^2	T, Myr	z_c	t, Myr	ε^2	T, Myr
1706+0502	0.98	6000	0.0164	6384	1.02	19000	0.028	6210
					0.96	4500	0.029	6451
1722+0442	1.00	5500	0.0014	6296	1.01	7000	0.005	6253
2029+0456	0.88	3250	0.0115	6853	0.81	1000	0.008	7214
2219+0458	1.37	8500	0.0431	4963	1.22	16000		5444
2224+0513	0.93	5000	0.0058	6612	0.71	2500	0.014	7783
2247+0507	0.93	3000	0.0040	6612	0.79	800	0.010	7322
					1.05	1200	0.010	6085
2348+0507	1.44	1700	0.0047	4761	2.10	3500	0.003	3367
	2.05	3750	0.0160	3448				

0034+0513—The GISSEL'98 model yields stellar-population ages exceeding the age of the Universe at this z in both cases; we prefer the version with the smallest difference, despite its somewhat larger error.

0039+0454—The PEGASE model yields an unacceptably large age for the stellar system, exceeding the age of the Universe at the given z by a factor of three. We obtained similar results for a number of other sources (0209+0501a, 0845+0454, 1152+0449, 1235+0435b, 1510+0438, and 2219+0454). The origin of this discrepancy remains unclear.

0105+0501—In contrast to most of the sample objects, the two models yield discrepant redshifts and ages for this source. Moreover, our computations yielded very large rms errors. Optical images in the four filters [34] show that the bright Ly_α line falls in the V band, distorting the magnitude measured in this filter.

0135+0450—The redshift of this source is between 0.34 and 0.10, but should be closer to 0.34. The GISSEL'98 model yields another minimum at $z = 0.24$, with an age of 5500 Myr and an rms error of 0.0117. The solutions corresponding to the absolute minima of both models must be discarded, since the inferred age of the stellar population is inconsistent with the age of the Universe.

0159+0448—The redshifts $z = 0.02$ (GISSEL'98) and $z = 0.09$ (PEGASE) lie outside the acceptable domain in the z–R plane [35]. We therefore consider the version with $z = 0.41$ to be more reliable.

0318+0456—The redshifts $z = 0.28$ (GISSEL'98) and $z = 0.2$ (PEGASE) lie outside the acceptable domain in the z–R plane [35].

0444+0501— Although the redshifts $z = 1.27$ (GISSEL'98) and $z = 1.21$ (PEGASE) are close to each other and have the smallest errors, we adopt the value $z = 2.35$, since this source has a spectroscopic redshift of $z = 2.73$.

0836+0511—The redshifts $z = 1.36$ (GISSEL'98) and $z = 1.34$ (PEGASE) are close to each other and have nearly the minimum rms errors.

0845+0444—The redshift $z = 5.29$ (PEGASE) is unacceptable due to both the implied age and the position in the z–R plane.

0908+0451—This color redshift was confirmed by spectroscopic observations made on the 6-m telescope of the Special Astrophysical Observatory.

1142+9455—The redshifts $z = 4.99$ (GISSEL'98) and $z = 4.95$ (PEGASE) lie outside the acceptable domain in the z–R plane. We chose $z = 0.36$, although it implies a stellar-population age that somewhat exceeds the age of the Universe at the given redshift.

1213+0500—The redshift $z = 5.15$ (GISSEL'98) lies outside the acceptable domain in the z–R plane and the implied stellar-population age exceeds the age of the Universe by more than a factor of 10.

1322+0449—The version with $z = 0.99$ is ruled out, since it yields a stellar-population age that is more than twice the age of the Universe.

1357+0453—We adopt $z = 0.72$, which is close to the redshifts given by both models.

1429+0501—No acceptable parameter values could be obtained for either model, possibly due to problems with separating the radio galaxy's optical light from the contribution of a nearby star [4].

1436+0501—We adopt the versions with $z = 1.35$ (GISSEL'98) and $z = 1.37$ (PEGASE), which have nearly the minimum errors.

1446+0507—The redshift $z = 4.99$ with the minimum error lies outside the acceptable domain in the z–R plane, and the implied stellar-population age exceeds the age of the Universe by a factor of 3.5.

1626+0448—The redshifts $z = 0.03$ and $z = 0.04$ lie outside the acceptable domain in the z–R plane. The large errors in all cases are due to the fact that the bright Ly_α line falls in the B band [4].

1638+0450—We adopt $z = 1.74$ (GISSEL'98) and $z = 1.57$ (PEGASE), although $z = 0.89$ (GISSEL'98) and $z = 0.84$ (PEGASE) cannot be completely ruled out.

1703+0502—The magnitudes in all filters may be distorted by a nearby bright star [4].

2247+0507—We adopted $z = 1.05$ for the PEGASE model, which is close to the redshift obtained for the GISSEL'98 model.

2348+0507—The magnitudes in all filters may be distorted by a nearby bright star [4].

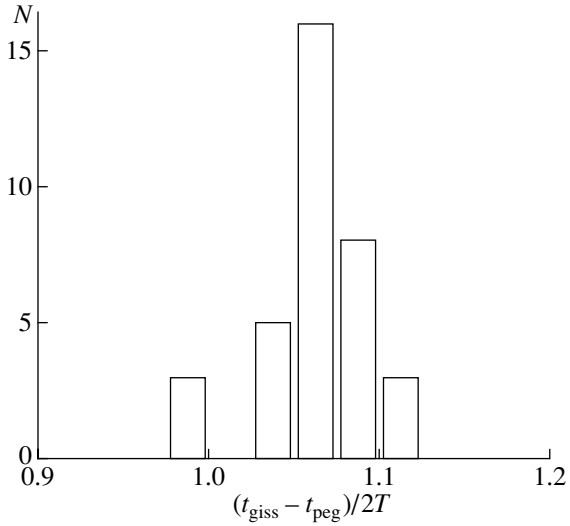

Fig. 2. The redshift dependence of the systematic difference between the stellar-population ages derived using the GISSEL'98 (t_{giss}) and PEGASE (t_{peg}) models normalized to the age of a Universe with $\Lambda = 0.7$ (T) at the epoch corresponding to the redshift. Deviations from the resulting dependence are of the order of 6%.

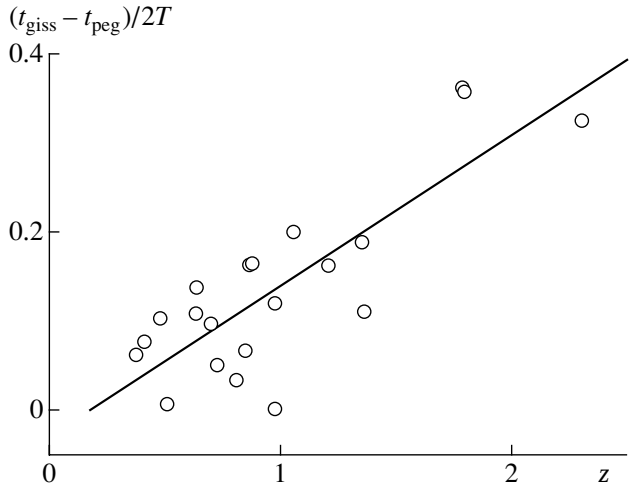

Fig. 3. Histogram of the ratio of the half-difference of the color ages for the stellar systems obtained using the GISSEL'98 (t_{giss}) and PEGASE (t_{peg}) models to the age of a Universe with $\Lambda = 0.7$ (T) at the epoch corresponding to the measured redshift. We show the central part of the histogram accounting for more than 80% of all the objects.

range for the color measurements to include the H and K bands, and this would enable us to resolve ambiguities in the results in a number of cases. The situation could change for extremely distant objects with $R > 24^m$, and we must wait for these observations to be completed before giving recommendations about how to proceed. It is clear from general considerations that there are dangers on both the "right" and the "left": sites of secondary star formation could distort the blue part of the spectrum, whereas dust at large redshifts could affect the infrared spectrum. At least the Ly_α line must be taken into account at $z > 2$. Generally speaking, large residuals may be indicative of contamination by strong lines, and we hope to take this into account in future analyses. Large errors could also be due to the serial periodicity of the Bohr model; however, energy considerations (discrepancies between color and photometric estimates) may be of help in such cases. This can be illustrated by RC J1703+0502, for which the lowest residual formally corresponds to a redshift of zero. However, this estimate would imply too low an optical luminosity for the object to produce an appreciable radio flux (recall that $P_{radio} \sim L_{opt}^{2.5}$; [38, 39]). In some cases, secondary criteria require discarding the result with the lowest residuals in favor of another with somewhat higher residuals.

(2) The ages of the host-galaxy stellar populations

Age is much more difficult to estimate than redshift, and the older the stellar population, the larger the error in its age. As in the case of redshifts, we constructed a histogram (Fig. 2) of the half-differences of the ages derived using the GISSEL'98 (t_{giss}) and PEGASE (t_{peg}) models for a given object, normalized to the age of a Universe with a cosmological constant $\Lambda = 0.7$ (T) at the epoch corresponding to the measured redshift.

The distribution of the difference of the ages derived using the two models is far from normal, and has a core including 70% of all the objects. The "model" dispersion for these core objects is close to 20%. The PEGASE ages have a large scatter, with six of the 50 objects having formal ages for their host stellar systems exceeding the age of the Universe, even when the color redshifts are close to those for the GISSEL model.

This led us to conclude that the GISSEL model was more trustworthy. The two models yielded systematically different results, with the discrepancy increasing with redshift (Fig. 3). Taking this into account, the dispersion in the model ages decreases to $< 10\%$ for objects with similar redshifts derived for the two models.

In a cosmological model with a Λ term of 0.7–0.8, none of the galaxy ages implied by the GISSEL model exceed the age of the Universe within the estimated errors, whereas there are more than ten such galaxies when we use a standard cold dark matter model. Accordingly, these galaxies can be used to independently

estimate the behavior of $H(z)$, the Λ term, and the "quintessence" (as suggested by Starobinskiĭ) [40].

The mean age of the galaxies is several Gyr, but the sample contains a subgroup of galaxies whose ages are close to that of the Universe at the given redshift within the errors, as well as a group of formally very young stellar systems (with ages of several Myr). The former evidently belong to the first generation of galaxies, which formed at $z >> 1$ ($z \sim 5$–10). The situation with the "younger" objects is more complex: in principle, their colors could be distorted by outbursts of secondary star formation due to mergers or close encounters. Furthermore, these are powerful radio galaxies, so that such young ages would require the rapid formation of supermassive black holes [41] with masses of about $10^9 M_\odot$, which is not possible in standard models for black-hole formation [39]. Therefore, the only alternative is that these objects are associated with primordial black holes with masses of 10^4–$10^6 M_\odot$, which later served as centers of galaxy formation.

To summarize, we cautiously conclude that at least the statistical redshift estimates for the populaton of powerful radio galaxies yield satisfactory results, and that the GISSEL model is recommended for both radio-quiet galaxies and powerful radio galaxies. Obtaining more trustworthy estimates will require the use of all available data about the objects, to reduce the number of large errors.

Unfortunately, the fact that different models sometimes yield similar age estimates does not always imply that the corresponding models are correct. It is usually thought that selecting the most powerful radio galaxies automatically gives us the largest, fairly old elliptical systems, whose radiation should be dominated by the contribution of old stars, with the inclination of the galaxy axis to the line of sight playing only a minor role. Possible exceptions are cases where the interstellar medium is irradiated by the central object. This conclusion is qualitatively confirmed by our own color redshifts and those obtained in other studies [36], which, as a rule, agree with the spectroscopic redshifts.

However, the literature includes data for some objects with nearly no jump in their SED near 4000 Å (i.e., nearly no Balmer jump) [42], suggesting that the luminosity is dominated by the contribution of fairly young stars. We believe that such cases do not necessarily reflect a young age for the galaxy as a whole, and that the hypothesis of secondary starburst activity is more plausible. As has been pointed out in the literature, in this case, the age of the young component of the stellar population could be comparable to the age of the radio source (although, for giant ellipticals, the models imply no appreciable color changes as a result of a merger involving a spiral galaxy).

In summary, we believe that it is safer to treat our inferred ages as lower limits. There is hope that a combination of photometric and spectroscopic studies may eventually bring success to searches for distant stellar systems. Quasars can be used to select fields for deep spectroscopic studies of galaxies located in their vicinity. The galaxies found can then be subjected to detailed spectroscopic studies of the light from their stellar components (even in the phase of active radio emission) [43, 44].

7. CONCLUSIONS

In conclusion, we summarize our results.

(1) We have reported the most extensive data set to date on the $BVRI$ colors of the host galaxies associated with powerful radio galaxies.

(2) We have developed and tested a program for the automated determination of galaxy color redshifts and ages, which can be used for any redshift and takes into account the transformation of the filter transmission curves in the transition from the rest frame to the moving frame. The program is available via the internet at http://sed.sao.ru.

(3) The color redshifts of powerful radio galaxies are in satisfactory agreement with their spectroscopic redshifts (the errors are 10–20%, with a small percentage of very large errors).

(4) A limited set of closely spaced filters, such as our $BVRI$ measurements, can yield satisfactory results even at large redshifts.

(5) The redshift distribution of the objects in our sample we have studied thus far (the subgroup of objects brighter than $m_R = 23.5^m$) shows a maximum near $z \sim 1$, i.e., in the region of maximum activity of the Universe at radio wavelengths. The group of objects with large color redshifts ($z > 2.5$–3) requires a separate analysis. In any case, we do not believe the population gap in the redshift interval ($1.5 < z < 2.5$) to be a real feature.

(6) As a rule, the color data are consistent with R-band photometry for objects with $R < 22.5^m$. Fainter sources show larger scatter of their photometric redshifts at a fixed R magnitude, and two branches are visible in the z–R plane [35]. Thus far, no conclusive results could be obtained by searching for differences in morphology, radio luminosity, or spectral index. Objects with the steepest spectra and highest radio-to-optical luminosity ratios are found only in the large-redshift branch. Further studies are required, however. As expected, objects with relatively low radio luminosities are quasars or nearby galaxies.

(7) Galaxy ages are determined with higher uncertainties, and the results obtained for large z have low statistical significance. However, it is virtually always possible to infer a lower limit for the ages of the galaxies and, consequently, a minimum redshift for their formation. This age always exceeds the standard estimate of the radio source's lifetime and, in a number of cases, the age of the Universe at the redshift of the radio source for a simple cold dark matter model. There are no such galaxies if their ages are calculated for a model with a Λ term of 0.6–0.8 (see, e.g., [45]).

We plan further studies of the application of color and photometric methods to the population of distant radio galaxies. New, more realistic models for the color evolution and refined estimates of the ages of the stellar populations should, in principle, make it possible to obtain much more reliable estimates for a large number of objects.

8. ACKNOWLEDGMENTS

This work was partially supported by the "Astronomy" State Science and Technology Program, projects 1.2.1.2 and 1.2.2.4; the Russian Foundation for Basic Research, project no. 99-02-17114; INTAS, grant 97-1192; and the Integration project (578, 206). O.V. Verkhodanov, A.I. Kopylov, and O.P. Zhelenkova thank the Russian Foundation for Basic Research, project no. 99-07-90334, for supporting the development of the server used to compute the estimated redshifts and ages of the radio galaxies (http://sed.sao.ru).

REFERENCES

1. Yu. Parijskij, A. Kopylov, N. Soboleva, *et al.*, in *Proceedings of the NATO Advanced Study Institute on Course Current Topics in Astrofundamental Physics: Primordial Cosmology,* NATO ASI Ser. **511**, 443 (1998).
2. R. A. Daly, Astrophys. J. **426**, 38 (1994).
3. Yu. N. Parijskij, A. I. Kopylov, O. P. Zhelenkova, *et al.*, Turk. J. Phys. **18** (9), 894 (1994).
4. Yu. N. Parijskij, W. M. Goss, A. I. Kopylov, *et al.*, Bull. SAO **40**, 5 (1996a).
5. Yu. N. Parijskij, N. S. Soboleva, W. M. Goss, *et al.*, in *Extragalactic Radio Sources (IAU Symposium 175, 1996)*, p. 591.
6. P. J. McCarthy, Ann. Rev. Astron. Astrophys. **31**, 639 (1993).
7. C. R. Benn, J. Wall, M. Vigotti, *et al.*, Mon. Not. R. Astron. Soc. **235**, 465 (1988).
8. Yu. N. Parijskij, W. M. Goss, A. I. Kopylov, *et al.*, Astron. Astrophys. Trans. **19**, 297 (2000).
9. A. S. Szalay, in *Cosmology and Large Scale Structure,* Ed. by R. Shaeffer *et al.* (Elsevier, Amsterdam, 1996), p. 253.
10. S. N. Dodonov, Yu. N. Pariĭskiĭ, V. M. Goss, *et al.*, Astron. Zh. **76** (5), 323 (1999) [Astron. Rep. **43**, 275 (1999)].
11. V. L. Afanas'ev and A. V. Moiseev, http://www.sao.ru/~moisav/scorpio/scorpio.html.
12. Yu. Parijskij, N. N. Bursov, N. M. Lipovka, *et al.*, Astron. Astrophys., Suppl. Ser. **87**, 1 (1991).
13. Yu. Parijskij, N. N. Bursov, N. M. Lipovka, *et al.*, Astron. Astrophys., Suppl. Ser. **96**, 583 (1992).
14. A. U. Landolt, Astron. J. **104**, 340 (1992).
15. D. Schlegel, D. Finkbeiner, and M. Davis, Astrophys. J. **500**, 525 (1998).
16. S. von Hoerner, in *Galactic and Extragalctic Radio Astronomy,* Ed. by G. L. Verschuur and K. I. Kellermann (Springer-Verlag, Berlin, 1974).
17. N. Arimoto and Y. Yoshii, Astron. Astrophys. **179**, 23 (1987).
18. K. Chambers and S. Charlot, Astrophys. J. **348**, L1 (1990).
19. S. Lilly, Mon. Not. R. Astron. Soc. **229**, 573 (1987).
20. S. Lilly, in *Evolution of the Universe of Galaxies: Proceedings of the Edwin Hubble Centennial Symposium,* Ed. by R. G. Kron (Astronomical Society of the Pacific, San Francisco, 1990), p. 344.
21. M. Fioc and B. Rocca-Volmerange, Astron. Astrophys. **326**, 950 (1997).
22. G. Bruzual and S. Charlot, Astrophys. J. **405**, 538 (1993).
23. M. Bolzonella, J. Miralles, and C. R. Pello, Astron. Astrophys. **363**, 476 (2000).
24. O. V. Verkhodanov, A. I. Kopylov, Yu. N. Pariĭskiĭ, *et al.*, Preprint No. 129 (St. Petersburg, 1999).
25. O. V. Verkhodanov, A. I. Kopylov, Yu. N. Pariĭskiĭ, *et al.*, Preprint No. 131 (St. Petersburg, 1999).
26. B. Rocca-Volmerange and B. Guiderdoni, Astron. Astrophys., Suppl. Ser. **75**, 93 (1988).
27. G. Bruzual and S. Charlot, anonymous@ftp://gemini.tuc.noao.adu/pub/charlot/bc96 (1996).
28. G. E. Miller and J. M. Scalo, Astron. Astrophys., Suppl. Ser. **41**, 513 (1979).
29. O. V. Verkhodanov, A. I. Kopylov, O. P. Zhelenkova, *et al.*, Astron. Astrophys. Trans. **19**, 662 (2000).
30. O. V. Verkhodanov, Bull. SAO **41**, 149 (1996).
31. Yu. N. Pariĭskiĭ, N. S. Soboleva, A. V. Temirova, *et al.*, Preprint No. 121 (St. Petersburg, 1997).
32. O. V. Verkhodanov, A. I. Kopylov, Yu. N. Pariĭskiĭ, *et al.*, in *Proceedings of the XV Conference on Topical Problems of Extragalactic Astronomy, Pushchino, 1998* [in Russian].
33. O. V. Verkhodanov, A. I. Kopylov, Yu. N. Parijskij, *et al.*, in *Prospects of Astronomy and Astrophysics for the New Millennium, JENAM, Prague, 1998,* p. 302.
34. N. S. Soboleva, V. M. Goss, O. V. Verkhodanov, *et al.*, Pis'ma Astron. Zh. **26** (10), 723 (2000) [Astron. Lett. **26**, 623 (2000)].
35. T. Pursimo, K. Nelson, P. Teerikorpi, *et al.*, Astron. Astrophys., Suppl. Ser. **134**, 505 (1999).
36. O. V. Verkhodanov, A. I. Kopylov, Yu. N. Pariĭskiĭ, *et al.*, Preprint No. 135 (St. Petersburg, 2001).

37. O. V. Verkhodanov, A. I. Kopylov, Yu. N. Pariĭskiĭ, *et al.*, Preprint No. 136 (St. Petersburg, 2001).
38. S. Iskudaryan and Yu. N. Pariĭskiĭ, Izv. GAO, No. 182, 175 (1964).
39. A. Franceschini, S. Vercellone, and A. Fabian, Mon. Not. R. Astron. Soc. **297**, 817 (1998).
40. T. Saini, S. Raychaudhury, V. Sahni, *et al.*, astro-ph/9910231 (2000).
41. P. Salucci, E. Szuszkievicz, P. Monaco, *et al.*, astro-ph/9811102 (1999).
42. F. Hammer, O. Le Fevre, and M. C. Angonin, Nature **362**, 324 (1993).
43. L. A. Nolan, J. S. Dunlop, R. Jiménez, and A. F. Heavens, astro-ph/0103450 (2001).
44. A. Stockton, astro-ph/0104191 (2001).
45. P. De Bernardis, P. A. R. Ade, J. J. Bock, *et al.*, Nature **404**, 955 (2000).

Translated by A. Dambis

Astronomy Reports, Vol. 46, No. 7, 2002, pp. 543–550. Translated from Astronomicheskiĭ Zhurnal, Vol. 79, No. 7, 2002, pp. 601–609.

Search for Spatial and Spectral Fluctuations of the Cosmic Microwave Background Radiation Using the RATAN-600 Radio Telescope

I. V. Gosachinskij [1], V. K. Dubrovich[2], S. R. Zhelenkov[2], G. N. Il'in[1], and V. A. Prozorov[1]

[1] *St. Petersburg Branch of the Special Astrophysical Observatory, Russian Academy of Sciences, Pulkovo, St. Petersburg, 196140 Russia*

[2] *Special Astrophysical Observatory, Russian Academy of Sciences, Nizhniĭ Arkhyz, Karachaevo-Cherkesskaya Republic, 357169 Russia*

Received November 20, 2000; revised October 23, 2001

Abstract—We report the results of a search for spatial and spectral fluctuations of the cosmic microwave background in the region of the North celestial pole carried out at 6.2 cm using the RATAN-600 radio telescope in 1999–2000. The spatial spectrum is flat and has no features exceeding $\Delta T/T = 10^{-3}$ in a $\sim$1 MHz frequency band for spatial periods from $0.5'$ to $16'$. If this estimate is adopted as an upper limit for emission associated with the first rotational transition of primordial LiH at $z = 90.7$, we obtain an upper limit for the LiH abundance of about 3×10^{-14} for protocluster masses of about $10^{13} M_\odot$.

1. INTRODUCTION

Recent achievements in studies of primordial spatial fluctuations of the brightness temperature T_r of the cosmic microwave background (CMB) form a firm experimental basis for distinguishing between theories of the evolution of matter in the early Universe [1–3]. In particular, we can discuss various models for the formation of proto-objects in the post-recombination epoch with greater confidence. The growth in the density contrast $\Delta\rho/\rho$ with decreasing redshift z and the manifestation of certain specific processes in the cooling matter lead to the formation of secondary CMB fluctuations [4–9]. Several processes resulting in the formation of spatial fluctuations of the CMB brightness temperature are known.

Fluctuations $\Delta T/T_r$ developing at the recombination stage are due to gravitational effects [10] and scattering on free electrons [11], and have a blackbody spectrum by virtue of the independence of the scattering cross section on frequency. Later stages of expansion of the Universe are characterized by a relatively low number density of free electrons. Various extrapolations of standard mechanisms operating in the interstellar medium, galaxies, and quasars [9, 12–16] are most often considered for this stage. All these schemes are based on internal energy sources in a proto-object. In this case, the radiation intensity is determined by the nature of specific models, and can take on values over a very broad range. In this sense, even a simple constraint on the amplitudes $\Delta T/T_r$ is meaningful. The constraints derived from broad-band observations [17] can be recalculated to the narrow bandwidths we use. At a wavelength of 6 cm with a bandwidth of 1 MHz, this yields $\Delta T/T_r < 5 \times 10^{-3}$.

One likely mechanism for the formation of fluctuations in the CMB temperature after the recombination of hydrogen is scattering by small density inhomogeneities, which have peculiar velocities V_p and are opaque to electromagnetic radiation [4, 8]. The peculiar velocities expected on various spatial scales are predicted by all evolutionary models [11, 15]. At the same time, opacity can have various origins.

When the temperature of matter and radiation falls below 500–600 K, opacity can result from scattering in molecular lines if the matter contains certain elements, namely, He, D, Li, C, N, or O. The formation of such fluctuations was considered in [4] for the case of opacity in lines of the molecules LiH, HeH^+, H_2D^+, etc. In addition to pure scattering, the fluorescent conversion of some super-equilibrium photons or a combination of the two mechanisms are possible [4–6, 8, 15, 16, 19]. In all these cases, an important characteristic of the fluctuations becomes apparent—their very strong frequency dependence.

In the low-opacity case, the amplitude of fluctuations in the CMB temperature $\Delta T/T_r$ due to the peculiar velocity of the object V_p is approximately [1]

$$\Delta T/T_r = V_p \tau / c, \qquad (1)$$

where τ is the optical depth of the object to molecular lines ($\tau < 1$) and c is the velocity of light. Possible values of τ have been calculated in various studies [4,

12, 13–16, 20]. These results are obviously directly related to the abundance of some molecule, which, in turn, is a complex function of z. Based on (1) and the fact that, in all models, the V_p values for large z cannot exceed 300 km/s, we can obtain a general constraint on the magnitude of the effect due to this mechanism, $\Delta T/T_r < V_p/c < 10^{-3}$.

Molecular scattering in several lines results in a superposition of images of objects located at different z. As shown in [1], the cosmological molecules LiH and HD^+ can exist at $50 < z < 200$. The corresponding waveband for LiH lines is from 13 cm at $z = 200$ to 0.5 cm at $z = 50$. The waveband for HD^+ is from approximately 4.4 to 0.2 cm. The power spectra of the spatial fluctuations at millimeter wavelengths should show an increased fraction of small-scale fluctuations compared to the spectra at centimeter wavelengths.

Here, we report the results of observations carried out at 6.2 cm on the RATAN-600 radio telescope. The primary goals were to improve techniques for searching for spectral and spatial fluctuations, estimate possible origins of interference, and derive constraints on the amplitude of narrow-band fluctuations.

Observations of other groups [17, 21] have been obtained in relatively broad frequency bands. This limits the upper limit for fluctuations that could form in primordial shock waves or other systems with large peculiar-velocity gradients.

2. INSTRUMENTATION AND TECHNIQUE

Our search for spectral and spatial fluctuations of the CMB was carried out on the southern quadrant of the RATAN-600 radio telescope [22] at 6.2 cm in April 1999 and February 2000. To increase the integration time obtained with the fixed antenna, we used transit curves near the celestial pole at an apparent declination of $+89°30'$. At this elevation, the antenna beamwidth was $45'' \times 7'$, the source crossed the horizontal beamwidth in 343^s, and the readings had to be taken no less frequently than every 171^s. This mode increased the integration time by a factor of 114, or the sensitivity by a factor of 10.7, compared to transit observations of an object at the equator. The signal was recorded at the lower culmination, beginning from apparent right ascension $\alpha = 16^h03^m$ in 1999 and from $\alpha = 04^h00^m$ in 2000. Since the precessional correction in right ascension is proportional to $\tan\delta$ and the recording system operates in mean sidereal time, we introduced corrections at the beginning of the recordings in accordance with the precessional shift of the apparent position during the monthly observing sessions.

An uncooled HEMT amplifier [23] was used at the front end, yielding a system noise temperature of 70 K. We tuned the local oscillator so that the H110α line, which has a radial velocity of 0 km/s with respect to the Local Standard of Rest, was at the center of the spectrometer band. We used a 128-channel autocorrelation spectrum analyzer [24] with a survey bandwidth of 2.5 MHz and a resolution of 40 kHz for the spectral analysis. The readings of the autocorrelation function were integrated for 60 s and recorded on disk for subsequent processing. The total recording time exceeded 4.5 h, and no fewer than 256 independent readings were obtained in each recording in each observing session. This yielded measurements of the fluctuations in a $35' \times 7'$ arc-shaped strip. When transforming the autocorrelation function readings to spectrum readings using a Fast Fourier Transform (FFT), there were two readings (channels) separated by 20 kHz for each frequency channel. The readings were calibrated in units of antenna temperature using a noise-generator signal taking into account the nonlinearity of the broad-band signal path.

We then subtracted a linear zero baseline from each spectrum, derived from a regression fit of the spectrum readings for channels 10–120. The edge channels were excluded because the insufficiently steep slopes of the frequency response curve of the video channel decreased the sensitivity in these channels. In this way, we subtracted the continuum signal with all its irregularities, fluctuations, and broad-band interference. At the same time, since the desired spectral signal can have only a very small magnitude, the distortion of its spectrum due to this procedure should not be significant. The stability of the calibration noise generator and the antenna and receiver parameters was checked in each observing session using measurements of the reference sources 3C 20 and 3C 147 and their 6-cm positions and fluxes from [25]. The effective area of the antenna at the elevation of the observations was about 1000 m^2.

In each observing session, we selected records visually based on the absence of broad-band interference, parasitic emission (when the setting Sun is in far lobes of the antenna beam), and atmospheric fluctuations, as well as on the appearance of the profile averaged over the observation time. This yielded 10 observations in April 1999 and 22 observations in February 2000 for averaging. In each session, we randomly divided the observations into two groups so that we could distinguish systematic (correlated) effects from random effects by comparing the results for their half-sums and half-differences. In addition, in the 2000 session, we obtained a four-hour measurement of the spectrum of a matched, liquid-nitrogen-cooled load connected to the waveguide instead of the primary horn.

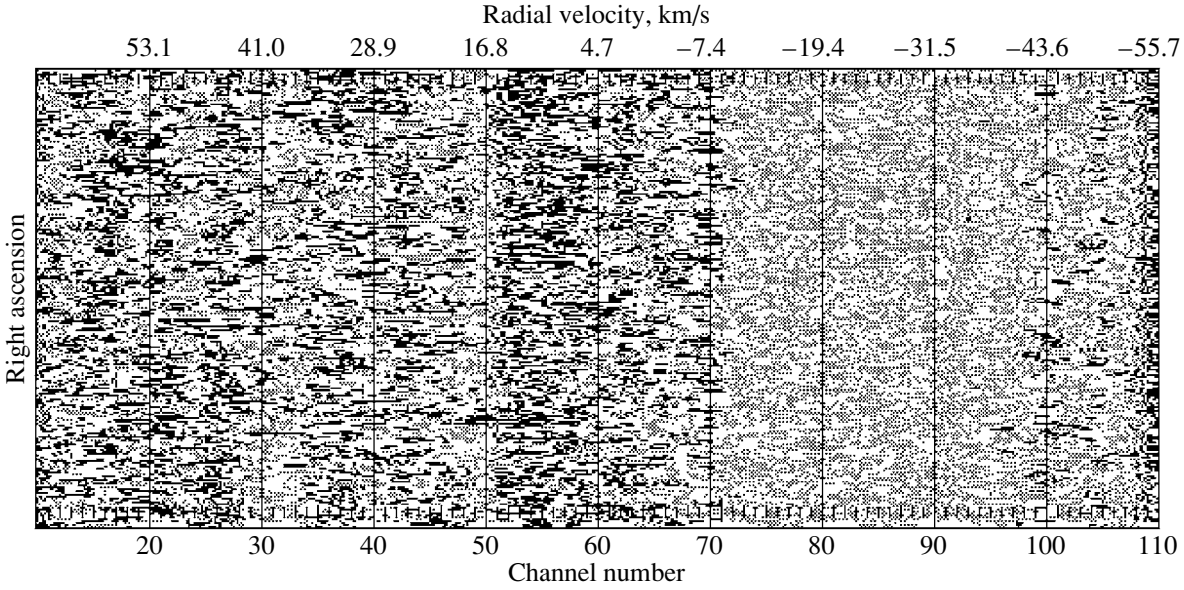

Fig. 1. Contours of the sky emission at 6.2 cm in right ascension–radial velocity coordinates for the observations of February 2000 (averaged over 16 observations). The interval between adjacent contours is 0.02 K.

We adopted a sampling period of 120^s for the subsequent reduction. To avoid so-called "frequency superposition" effects, we smoothed the records in each spectrometer channel using a $\sin(\omega t)/(\omega t)$ function with a period of 240 s. Figure 1 shows sample contours of the fluctuations for an average of 16 observations obtained in February 2000 in right ascension–radial velocity coordinates. The antenna-temperature step between adjacent contours is 0.02 K. The rms fluctuation of the antenna temperature in right ascension is 0.036 K, fairly close to the estimated value of 0.03 K, and the rms fluctuation in radial velocity is approximately the same. We can see a signal of approximately 0.07 K in spectral channels 55–70 (radial velocities near zero). We suspect that this is due to weak background emission by ionized Galactic hydrogen in the H110α line, to which the radio spectrometer was tuned in these observing sessions (essentially by chance). However, we cannot rule out the possibility of an instrumental effect due to some small spectral nonlinearity of the autocorrelation spectrum analyzer path that was not taken into account. To remove this feature from the records, we subtracted a linear "zero level" in each spectral channel, determined from reference points at the beginning and end of the record for each channel.

To study the spatial characteristics of the signal, we calculated the power spectrum of the fluctuations in right ascension (the square of the amplitudes) in each channel using a 64-point FFT. Prior to this, we removed a constant component and linear trend from processed sections of the records and multiplied the readings by a cosine time window. The scale of the power of the spatial fluctuations was calibrated using the mean square of the fluctuations of a record on the time scale in accordance with Parseval's theorem. To simplify the presentation of the results and reduce the fluctuations of the spectral readings, we averaged the resulting power spectra over 30–60 channels when there were no obvious narrower features in the spectra.

Figure 2 presents examples of logarithmic spatial spectra for the April 1999 and February 2000 observations obtained for the 30th, 60th, and 90th spectrometer channels. The spectra were smoothed over 60 channels (1.2 MHz). The zeroth harmonic is not shown in these spectra (its amplitude is zero). The ticks on the horizontal axis indicate harmonics of the spatial frequencies (from 1 to 32), and are labeled with the equivalent periods of the harmonics in right ascension (from 128^m to 4^m). This range of periods corresponds to angular values from 16.6′ to 0.52′. Note also that the readings of the spatial spectra in low-frequency channels show a much greater scatter than those in the higher-frequency part of the spectrum. This may be due to the above-mentioned insufficient quality of the spectrometer passband and episodic narrow-band crosstalk of unknown origin near spectral channels 27–28 (sinusoidal crosstalk in the records of the autocorrelation function).

3. RESULTS

It is evident from Fig. 2 that the measured spatial-fluctuation spectra look completely flat. The slopes of linear-regression approximations of the spectra are

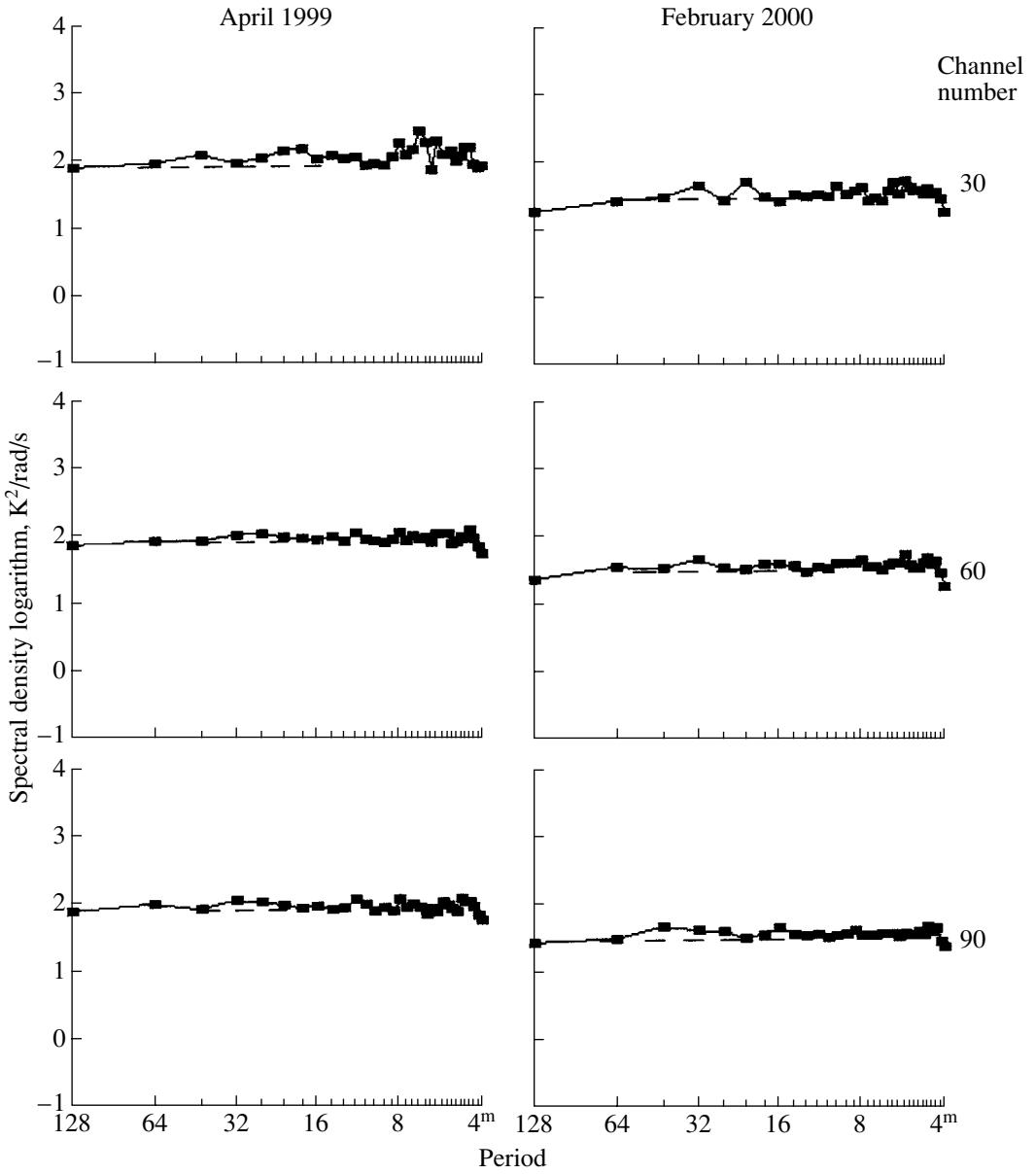

Fig. 2. Spectra of the spatial fluctuations in two observing sessions. Three 1.2-MHz intervals of the spectrometer channels are shown. The horizontal axes show the logarithms of the harmonic spatial frequencies, numbered with the equivalent periods in right ascension at declination 89°30′.

given together with their errors in Table 1. Though the systematic change in the slope of the spatial spectra as a function of frequency seems to be the same in both observing sessions, it does not exceed the 1σ errors and cannot be considered significant.

Of greater interest are the irregularities of the spectra in Fig. 2 in the region of spatial periods near $4'$ (32^m of right ascension). These are not random, since they are present in the data for both observing sessions, and vanish in the spectra of the difference signal. Figure 3 compares the spectra of the half-sum and half-difference for two groups of eight observations selected at random from the February 2000 session. These features are not visible in the difference spectrum. Unfortunately, we cannot completely rule out an instrumental or methodical origin for these irregularities. The reason is that spectral irregularities near the fourth harmonic cannot be considered completely absent from the spectra of the cold load obtained using the same procedure (Fig. 4), especially in the low-frequency channels.

It is difficult to recalculate the measured magnitude of the spectral irregularities to the corresponding amplitude of the variable component of the background antenna temperature because of the uncertain

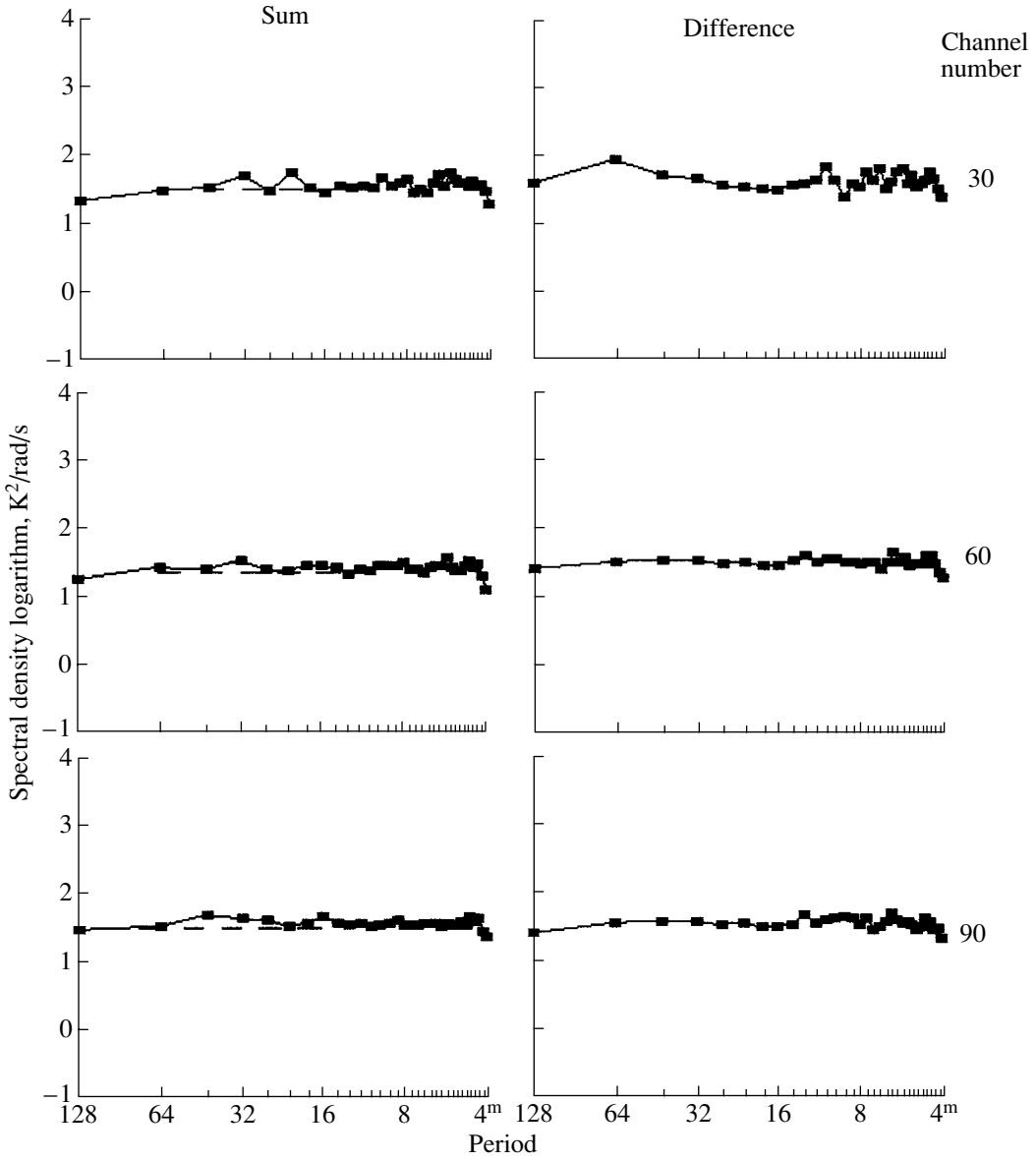

Fig. 3. Same as Fig. 2 for the half-sum and half-difference of two random groups of observations obtained in February 2000.

width of their spatial spectrum. However, a comparison of the power spectra for the observed features with model spectra for a synthetic sine-wave signal mixed with the observed noise signal shows that it is approximately 0.003 K, or $\sim 10^{-3}$ of $\Delta T/T_r$. This can be considered an upper limit for possible irregularities in the spatial spectra.

The presence of signals in the radio spectrum associated with some spatial-frequency range can also be tested using the difference of the cross-correlation functions of the signals in spectral channels separated by some frequency. Figure 5 presents correlation functions for sum and difference signals formed using two groups of 11 observations in the February 2000 session. These functions have been averaged over channels 10–120 in the entire range of spatial frequencies studied. The reading for zero shift is not shown, since it is identically equal to unity. The correlation for a shift by one channel is still fairly significant ($\sim$0.6), since there are two spectral readings ("channels") for each spectrum analyzer channel (40 kHz). A weak anticorrelated signal is visible for a wide range of channel separations (up to $\Delta n = 8$); this signal is real, since it is present in the sum signal but vanishes in the difference signal. We suggest that this is a weak spurious effect associated with two circumstances: (a) the "one-bit" technique used to measure the autocorrelation function, and, therefore, the area-normalized spectra, and (b) insufficiently accurate account of the nonlinearity of the broad-band

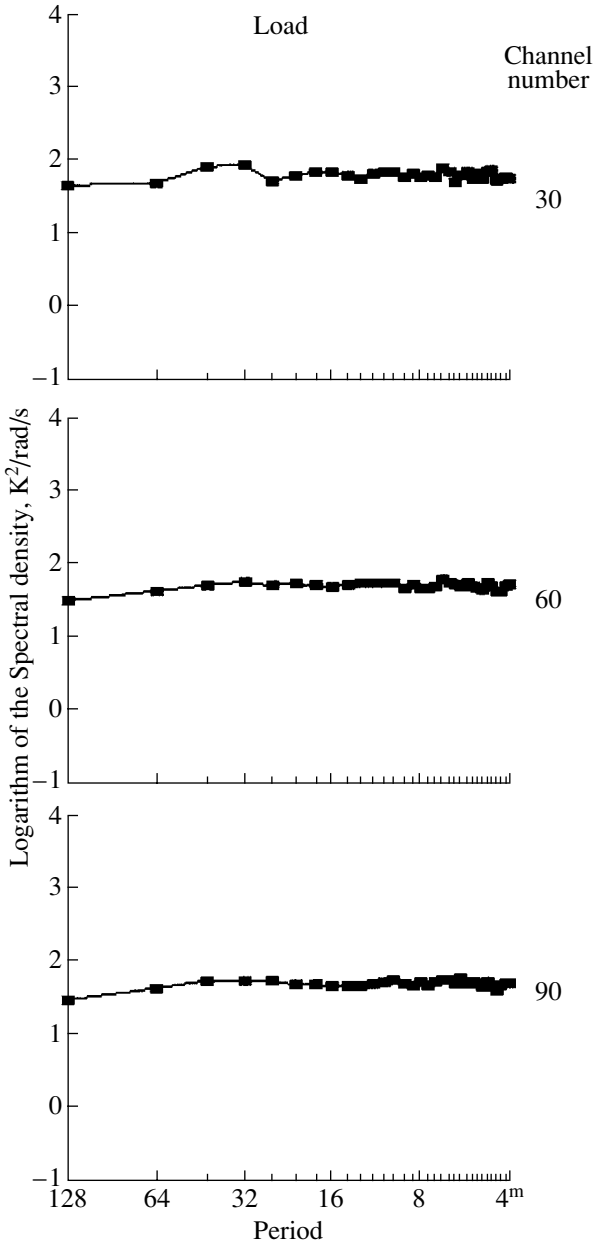

Fig. 4. Same as in Fig. 2 for a recording of a cold load in February 2000.

channel when denormalizing the spectra. The formal rms error of the correlation coefficient calculated for a sample of 259 independent readings does not exceed 0.004; however, the channel-to-channel scatter of the correlation coefficients yields an rms that is a factor of two to three higher. Although its origin is not clear, it is precisely this scatter that determines the final error σ_R after averaging over the channels. Thus, the magnitude of the spurious effect we have detected is not greater than $3\sigma_R$.

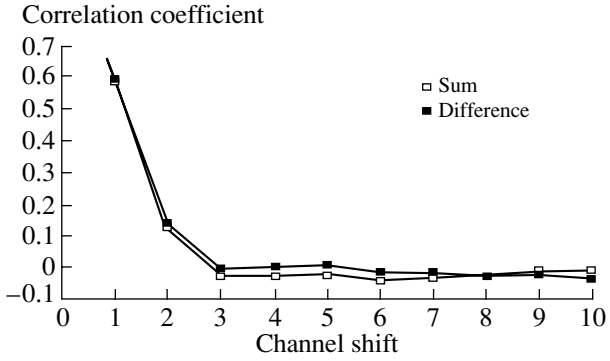

Fig. 5. Correlation coefficients of the records in right ascension as a function of channel separation.

4. DISCUSSION

To relate the angular sizes of objects θ and the linewidths to their physical sizes L, we must specify the relationship between these quantities in some model. We will consider standard models.

Modern observational data give preference to a flat expanding Universe with cosmological constant Λ. The exact relationships between θ and z in such models contain the parameters Ω_m and Ω_Λ—the ratio of the density of matter n_m and the "vacuum" density to the critical density n_c ($\Omega_m + \Omega_\Lambda = 1$)—and have the following form [26]:

$$\theta = (H_0 L/c)(1+z)/\varphi(z)$$

$$\varphi(z) = \int_0^z [\Omega_m (1+z)^3 + \Omega_\Lambda]^{-1/2} dz.$$

For large values of z, $H_0 = 60$ km s^{-1} Mpc^{-1} (h_{60}), and $\Omega_m = 0.3$, we obtain

$$\theta \approx 15'' h_{60} L_{\rm Mpc}(1+z),$$

where $L_{\rm Mpc}$ is L in megaparsecs. On the other hand, the near and far edges of the cloud are at different distances; i.e., they have different z's. The corresponding difference Δz is related to L as

$$\Delta z/(1+z) = (H_0 L/c)[\Omega_m (1+z)^3 + \Omega_\Lambda]^{1/2}.$$

Table 1. Measured exponents of the spatial spectra for periods from 16.6′ to 0.52′

Channel number	April 1999	February 2000
30	0.06 ± 0.07	0.06 ± 0.05
60	0.01 ± 0.03	0.03 ± 0.03
90	-0.02 ± 0.03	-0.01 ± 0.03

Table 2. Correlation coefficients of channel readings for various bands of the spatial-frequency spectrum

Channel shift Δn	$\Delta\theta$			
	4.16′–16.6′	2.08′–4.16′	1.04′–2.08′	0.52′–1.04′
1	0.549 ± 0.016	0.517 ± 0.015	0.533 ± 0.012	0.566 ± 0.008
	0.537 ± 0.017	0.506 ± 0.013	0.551 ± 0.010	0.583 ± 0.007
2	0.134 ± 0.025	0.108 ± 0.022	0.088 ± 0.016	0.121 ± 0.012
	0.136 ± 0.025	0.110 ± 0.019	0.116 ± 0.016	0.138 ± 0.011
3	-0.015 ± 0.026	-0.017 ± 0.022	-0.057 ± 0.016	-0.032 ± 0.013
	0.032 ± 0.026	-0.015 ± 0.020	-0.022 ± 0.015	-0.019 ± 0.011
4	-0.008 ± 0.026	-0.011 ± 0.022	-0.043 ± 0.018	-0.035 ± 0.013
	0.057 ± 0.025	-0.002 ± 0.021	-0.001 ± 0.016	-0.025 ± 0.011
5	0.008 ± 0.026	-0.034 ± 0.022	-0.042 ± 0.017	-0.028 ± 0.013
	0.044 ± 0.025	0.006 ± 0.021	0.015 ± 0.016	-0.026 ± 0.012
6	0.022 ± 0.024	-0.076 ± 0.021	-0.058 ± 0.016	-0.036 ± 0.013
	0.021 ± 0.025	-0.041 ± 0.022	0.004 ± 0.015	-0.038 ± 0.012
7	0.020 ± 0.021	-0.086 ± 0.020	-0.054 ± 0.015	-0.027 ± 0.013
	-0.004 ± 0.025	-0.055 ± 0.023	-0.020 ± 0.016	-0.023 ± 0.012
8	0.017 ± 0.025	-0.057 ± 0.023	-0.041 ± 0.016	-0.024 ± 0.013
	-0.029 ± 0.026	-0.051 ± 0.024	-0.046 ± 0.016	-0.004 ± 0.011
9	0.019 ± 0.023	-0.011 ± 0.023	-0.021 ± 0.016	-0.024 ± 0.012
	-0.037 ± 0.025	-0.048 ± 0.021	-0.052 ± 0.016	-0.002 ± 0.012
10	0.030 ± 0.023	0.005 ± 0.021	-0.013 ± 0.015	-0.029 ± 0.011
	-0.041 ± 0.025	-0.046 ± 0.021	-0.064 ± 0.017	-0.009 ± 0.013

The fact that the cloud occupies a redshift interval Δz means that, if it radiates or reflects emission locally in narrow lines, the emission will occupy a frequency range $\Delta\nu$:

$$(\Delta\nu/\nu)_{\rm H} = \Delta z/(1+z).$$

Consequently,

$$(\Delta\nu/\nu)_{\rm H} \approx \theta\varphi(z)[\Omega_m(1+z)^3 + \Omega_\Lambda]^{1/2}(1+z)^{-1}.$$

For large z and $\Omega_m = 0.3$, we obtain

$$(\Delta\nu/\nu)_{\rm H} \approx 1.3 \times 10^{-3}(\theta/1')[\varphi(z)/\varphi(20)](1+z)^{1/2}.$$

If we observe simultaneously using two receivers with a frequency difference $\Delta\nu$, we should see fluctuations with angular sizes greater than θ in both receivers. If the size of fluctuations is smaller, they will be detected in only one receiver, while there will be only background (or another object) detected by the other receiver at this point in the sky [12]. Thus, the correlation of these two observations will be zero on small scales to within the noise and nonzero on scales exceeding some scale. A pronounced turnover is possible only if all objects have the same size L. However, in reality, there will be some spectrum of scales. The effect we consider here demonstrates that the initial spectrum can be considerably distorted. The results of our attempts to reveal such effects are listed in Table 2. The two values of the correlation coefficient for each frequency shift and spatial interval correspond to the April 1999 and February 2000 observing sessions. Unfortunately, the accuracy of the correlation coefficients is insufficient to enable us to be confident that there was an appreciable increase in the anticorrelation (i.e., a negative correlation coefficient) at spatial frequencies from 1′ to 4′ for a frequency shift of six to eight channels. A more complete study of this problem is beyond the scope of this paper; however, it is already obvious that an analysis of the spectral and spatial fluctuations can yield additional information about the parameters of the matter and the redshifts z of most proto-objects.

The above estimate of the relationship between $(\Delta\nu/\nu)_{\rm H}$ and θ is valid if the cloud expansion follows the Hubble law. Taking into account self-gravitation at a certain stage radically changes this relationship. At the epoch when the expansion stops, we can effectively infer the presence of a gradient of the peculiar velocity along the line of sight [27]. This gradient changes sign when it crosses the center of the object; i.e., the near and far halves have negative and positive velocities (relative to the center), respectively. The accuracy of the compensation of the Hubble velocity can, in principle, reach a limit determined by the thermal or microturbulent velocity in the given object [8] and give a linewidth $(\Delta\nu/\nu)_T \approx 10^{-4}$. In this case, the effective optical depth increases by a factor of $N \approx (\Delta\nu/\nu)_{\rm H}/(\Delta\nu/\nu)_T$ [8, 27]. To obtain a limit for the abundance of molecules, we must take into account another line-intensity amplification factor, K_e, based on the luminescence effect [28]. For example, we have for the first rotational line of the LiH molecule and $\theta \approx 4'$

$$z = 6.2\ \text{cm}/0.0676\ \text{cm} - 1 = 90.7,$$

$$L = (\theta/15'')/(1+z)\ \text{Mpc} \approx 180\ \text{kpc},$$

$$N = 500.$$

This proto-object size corresponds to a baryon mass of approximately $10^{14} M_\odot$. According to [28], at such values of z, we have $K_e \approx 10^4$ for LiH. Adopting the corresponding constants for the optical depth and assuming a peculiar velocity of 60 km/s, we obtain the final estimate of the molecule abundance $\alpha_{\rm LiH} < 3 \times 10^{-14}$. This limit is approximately three orders of magnitude lower than the estimate of [21], and such a value is quite plausible from the viewpoint of nonequilibrium chemical kinetics in the presence of velocity and density gradients. However, definitive conclusions about the physical conditions in such objects require more accurate calculations. It is evident from these estimates that further improvement of the limit by one or two orders of magnitude should make it possible to determine the epoch at which the expansion of the first protoclusters ceased. Estimates for other molecules can be made in a similar way.

5. CONCLUSION

Thus, the presence of molecular clouds at early stages of the evolution of the Universe ($z > 100$) should lead to the formation of spectral and spatial fluctuations of the CMB. The magnitude of these fluctuations can reach 3×10^{-3} K in the case of simple scattering and can exceed this value in the presence of a sufficiently powerful early release of energy. Our results make it possible to address the question of detailed studies of these fluctuations. We have shown that, in principle, we can distinguish the effects of and identify primordial molecules. Furthermore, it should be possible to determine the interval of z in which these molecules exist and the parameter Ω_m.

REFERENCES

1. A. H. Jaffe, P. A. R. Ade, A. Balby, *et al.*, astro-ph/0007333.
2. J. A. Peacock, *Cosmological Physics* (Cambridge Univ. Press, Cambridge, 1999).
3. A. D. Sakharov, Dokl. Akad. Nauk SSSR **177**, 70 (1967) [Sov. Phys. Dokl. **12**, 1040 (1968)].
4. V. K. Dubrovich, Pis'ma Astron. Zh. **3**, 243 (1977) [Sov. Astron. Lett. **3**, 128 (1977)].
5. V. K. Dubrovich, Astron. Astrophys. **324**, 27 (1997).
6. V. K. Dubrovich, Gravitation and Cosmology **5**, 171 (1999).
7. V. K. Dubrovich, Izv. SAO **13**, 40 (1981).
8. V. K. Dubrovich, Astron. Astrophys. Trans. **5**, 57 (1994).
9. E. T. Vishniac, Astrophys. J. **322**, 597 (1987).
10. R. K. Sachs and A. M. Wolfe, Astrophys. J. **147**, 73 (1967).
11. Ya. B. Zel'dovich and R. A. Sunyaev, Astrophys. Space Sci. **4**, 301 (1969).
12. S. Lepp and J. M. Shull, Astrophys. J. **280**, 465 (1984).
13. R. Maoli, V. Ferrucci, F. Melchiorri, *et al.*, Astrophys. J. **457**, 1 (1996).
14. D. Puy, G. Alecian, J. LeBourlot, *et al.*, Astron. Astrophys. **267**, 337 (1993).
15. J. Silk, Astrophys. J. **151**, 459 (1968).
16. P. D. Stancil, S. Lepp, and A. Dalgarno, Astrophys. J. **458**, 401 (1996).
17. R. B. Partridge, E. A. Richards, E. B. Fomalont, *et al.*, Astrophys. J. **483**, 38 (1997).
18. V. K. Dubrovich and A. A. Lipovka, Astron. Astrophys. **296**, 301 (1995).
19. V. K. Dubrovich, in *Proceedings of HSRA* (Cambridge Univ. Press, Cambridge, 1997), p. 189.
20. D. Puy and M. Signore, Astron. Astrophys. **305**, 371 (1996).
21. P. De Bernardis, V. Dubrovich, P. Encrenaz, *et al.*, Astron. Astrophys. **269**, 1 (1993)
22. N. A. Esepkina, N. S. Bakhvalov, B. A. Vasil'ev, *et al.*, Izv. SAO **11**, 182 (1979).
23. A. M. Pilipenko and V. A. Prozorov, Preprint No. 114, SAO (St. Petersburg, 1995).
24. I. V. Gosachinskiĭand S. R. Zhelenkov, Preprint No. 96, SAO (St. Petersburg, 1993).
25. P. C. Gregory, W. K. Scott, K. Douglas, and J. J. Condon, Astrophys. J., Suppl. Ser. **103**, 427 (1996)
26. V. Sahni and A. Starobinsky, astro-ph/ 9904398 (1999).
27. Ya. B. Zel'dovich, Pis'ma Astron. Zh. **4**, 165 (1978) [Sov. Astron. Lett. **4**, 88 (1978)].
28. V. K. Dubrovich, Astron. Astrophys. **324**, 27 (1997).

Translated by G. Rudnitskiĭ

Astronomy Reports, Vol. 46, No. 7, 2002, pp. 551–566. Translated from Astronomicheskiĭ Zhurnal, Vol. 79, No. 7, 2002, pp. 610–626.

Parameters of Warm Molecular Clouds from Methyl Acetylene Observations

A. V. Alakoz [1], S. V. Kalenskiĭ[1], V. G. Promislov[1], L. E. B. Johansson[2], and A. Winnberg[2]

[1] *Astro Space Center, Lebedev Physical Institute, ul. Profsoyuznaya 84/32, Moscow, 117997 Russia*

[2] *Onsala Space Observatory, Onsala, S-439 92 Sweden*

Received October 15, 2001

Abstract—The results of a survey of 63 Galactic star-forming regions in the 6_K–5_K and 5_K–4_K methyl acetylene lines at 102.5 and 85.5 GHz are presented. Fourty-three sources were detected at 102.5 GHz, and twenty-five at 85.5 GHz. Emission was detected toward molecular clouds with kinetic temperatures of 20–60 K (so-called "warm clouds"). The CH_3CCH abundances in these clouds are about several $\times 10^{-9}$. Five sources (NGC 2264, G30.8–0.1, G34.26+0.15, DR 21(OH), S140) were mapped using the maximum-entropy method. The sizes of the mapped clouds fall in the range 0.1–1.7 pc, and the clouds have virial masses of 90–6200 $M_\odot$ and densities between 6×10^4 and 6×10^5 cm^{-3}. The CH_3CCH sources coincide spatially with the CO and CS sources. Chemical-evolution simulations show that the typical methyl acetylene abundances in the observed clouds correspond to ages of $\approx 6 \times 10^4$ years.

1. INTRODUCTION

Massive stars are known to form in so-called "warm" molecular clouds (Olmi *et al.*, [1]; Kalenskiĭ *et al.,* [2]), which have temperatures of 30–50 K, masses from hundreds to thousands of solar masses, and sizes of 0.1–3 pc. Therefore, investigations of such clouds are an important part of studies of star formation. Warm clouds have been fairly well studied in lines of CO, CS, NH_3, CH_3OH, and many other molecules. However, the CS, NH_3, CH_3OH, and CH_3CN emission is strongly affected by the contribution of compact regions of hot gas (hot cores), where the abundances of these and some other molecules are enhanced by several orders of magnitude owing to grain mantle evaporation.

To exclude the contribution of hot cores, we must observe warm clouds in lines of molecules for which the emission from hot cores is weak.

One such molecule is methyl acetylene. Its abundance is not enhanced in the Orion Hot Core [3] and, probably, is not enhanced in other hot cores as well. Since hot cores, which have sizes of approximately 0.05 pc, are much smaller than warm clouds, their contribution to the CH_3CCH emission is probably negligible.

The rotational lines of methyl acetylene are grouped in series of J_K–$(J-1)_K$ lines with closely spaced frequencies. Lines from the same series can be observed simultaneously with the same receiver, making it possible to obtain accurate ratios of their intensities. Methyl acetylene observations enable us to determine the gas kinetic temperature. Radiative transitions between different K ladders are prohibited by the selection rule $\Delta K = 0$; thus, the ratios of different K-ladders' populations are determined by collisions, and depend primarily on the gas kinetic temperature. Since methyl acetylene has a fairly small dipole moment 0.78 D [4], it is collisionally thermalized even at densities $\sim 10^4$ cm^{-3}. In addition, methyl acetylene lines in warm clouds that have been already observed have been optically thin [3]. These properties enable us to assume local thermodynamic equilibrium (LTE) and utilize simple analysis methods such as rotational diagrams, which produce fairly accurate temperature estimates in this case. The simulations of Askne *et al.* [5] showed that the methyl acetylene rotational temperatures are approximately equal to the gas kinetic temperatures.

2. OBSERVATIONS

The observations were carried out in May 1997[1] using the 20-m millimeter-wave radio telescope of the Onsala Space Observatory in Sweden. The frequency, line strength, and upper-level energy for each observed transition are given in Table 1. The pointing accuracy was checked using observations of SiO masers, and was no worse than 5″. The observations were performed in a dual-beam-switching mode with

[1] Sensitive observations of the four sources W3(OH), Orion KL, W51 E1/E2, and DR 21(OH) were conducted in 2000.

1063-7729/02/4607-0551$22.00

Table 1. Parameters of the observed methyl acetylene lines

Transition	Frequency, GHz	S	E_u/h, K
6_0–5_0	102547.984	6.00	12.315
6_1–5_1	102546.024	5.83	19.300
6_2–5_2	102540.144	5.33	40.258
6_3–5_3	102530.348	4.50	75.181
6_4–5_4	102516.573	3.33	124.060
6_5–5_5	102499.110	1.83	186.885
5_0–4_0	85457.272	5.00	8.209
5_1–4_1	85455.622	4.80	15.196
5_2–4_2	85450.730	4.20	36.153
5_3–4_3	85442.528	3.20	71.076
5_4–4_4	85431.224	1.80	119.956

a beam separation of 11′ and a switching rate of 2 Hz. The main beam's efficiency and full width at half power were 0.55 and 38″ at 102 GHz and 0.6 and 43″ at 85 GHz. A cooled low-noise SiS mixer was used for the observations at both frequencies. The system noise temperature corrected for atmospheric absorption, rearward spillover, and radome losses varied between 350 and 2000 K, depending on the weather conditions and source elevation. The data were calibrated using the chopper-wheel method. The backend consisted of two parallel filter spectrometers: a 256-channel spectrometer with 250 kHz resolution and a 512-channel spectrometer with 1 MHz resolution. Sixty-three sources were observed at 102 GHz. Thirty-two of these were also observed at 85 GHz. When fitting Gaussians to the lines, we assumed that different J_K–$(J-1)_K$ lines with the same J had identical radial velocities and widths. The five sources NGC 2264, G30.8–0.1, G34.26+0.15, DR 21(OH), and S140 were mapped at 102 GHz using the technique described below.

Forty-three sources were detected at 102 GHz and twenty-five at 85 GHz. The source coordinates and Gaussian parameters of the detected lines are presented in Table 2. The spectra of the detected sources are shown in Figs. 1, 2, and 3.

3. DATA ANALYSIS

The spectra in Figs. 1–3 demonstrate that, in most of the sources, only the $K=0$, $K=1$, and $K=2$ lines with low excitation energies (Table 1) were detected, with the $K=0$ and 1 lines usually being blended. Sometimes, the $K=3$ line can be distinguished from the noise. Only in the four sources observed in 2000 with high sensitivity were the very weak $K=4$ lines detected.

Figure 2 shows the 6_K–5_K methyl cyanide spectra of three sources observed by Kalenskiĭ *et al.* [6] with the same equipment and approximately the same sensitivity as the methyl acetylene lines. Like methyl acetylene, methyl cyanide (CH_3CN) is a symmetric top molecule, and its spectrum also consists of J_K–$(J-1)_K$ groups. The methyl acetylene and methyl cyanide spectra of NGC 7538S are similar (there are no lines with $K>3$ in either spectrum) and display the same radial velocities, so that it is reasonable to assume that the emission of both molecules arises in the same region. In W3(OH) and G34.26+0.15, the contribution of hot cores to the methyl cyanide emission is significant [6]. In these objects, high-energy lines are clearly detectable in the methyl cyanide spectra, but are not appreciable in the methyl acetylene spectra. The high-energy CH_3CN lines appear in the spectra of these sources due to the contribution of hot cores [6], and the absence of detectable emission in the analogous methyl acetylene lines suggests that the contribution of hot cores to the CH_3CCH emission is insignificant. In all the observed sources, high-energy CH_3CCH lines are either weak or not detected. Since many of the sources harbor hot cores, it is reasonable to assume that, as a rule, the contribution of hot cores to the methyl acetylene emission is small.

We constructed rotational diagrams for 40 sources at 102 GHz and 23 sources at 85 GHz (Fig. 4). The temperatures derived from the rotational diagrams are 20–60 K, typical of warm clouds, and agree within the errors with those derived from observations of ammonia, methanol, and methyl cyanide [2, 6–12]. The methyl acetylene column densities vary from 4×10^{13} cm^{-2} to 1.2×10^{15} cm^{-2}, being in the narrower range $(1-5)\times10^{14}$ cm^{-2} in most (about 70%) of the sources.

The observations of W3(OH), DR 21(OH), Orion KL, and W51 E1/E2, which resulted in the detection of a fairly large number of lines (up to $K=4$), were analyzed without assuming that the lines were optically thin. We calculated the ratios of the line brightness temperatures for different sets of gas temperatures and CH_3CCH column densities by assuming that the CH_3CCH level populations were thermalized. The temperature was varied from 10 to 200 K and the column density from 10^{11} to 10^{15} cm^{-2}, assuming the sources to be uniform. We then selected the models in best agreement with the observations according to a χ^2 criterion. The results are presented in Fig. 5, which shows that both optically thin models and models with opacities τ of the $K=0$ and $K=1$ lines of about unity can fit the observations. In the

Table 2. Gaussian parameters for detected CH_3CCH lines with 1σ errors. The parameters of 102 GHz and 85 GHz lines are presented in the upper and lower rows

Source	RA (1950) DEC (1950)	$\int T_A^* dV$, K km s^{-1}					V_{LSR}, km s^{-1}	FWHM, km s^{-1}
		$K=0$	$K=1$	$K=2$	$K=3$	$K=4$		
00338+6312	$00^h33^m53^s.3$	0.81(0.05)	0.66(0.04)	0.22(0.04)	0.15(0.04)	<0.12	−17.33(0.06)	2.74(0.1)
	63°12′33″.0	Not observed						
02232+6138	02 23 13.4	0.93(0.07)	1.06(0.08)	0.35(0.08)	<0.21	<0.21	−46.56(0.08)	2.79(0.1)
	61 38 44.8	Not observed						
W3(OH)	02 23 17.3	0.74(0.02)	0.55(0.02)	0.24(0.02)	0.18(0.02)	0.04(0.02)	−47.097(0.09)	5.43(0.10)
	61 38 58.0	0.64(0.02)	0.48(0.02)	0.28(0.01)	0.18(0.01)		−47.679(0.11)	6.74(0.12)
02575+6017	02 57 35.6	0.21(0.04)	0.17(0.04)	<0.12	<0.12	<0.15	−37.96(0.15)	1.75(0.24)
	60 17 22.6	Not observed						
L1527	04 36 49.3	0.22(0.03)	0.18(0.03)	<0.05			5.78(0.07)	1.21(0.10)
	25 57 16.0	0.16(0.05)	0.19(0.07)	<0.09			5.97(0.08)	0.74(0.14)
G174.20	05 27 32.2	0.16(0.04)	0.13(0.05)	<0.12			−2.39(0.35)	3.01(0.58)
	33 45 52.0	Not observed						
Orion S6	05 32 44.8	1.42(0.10)	0.95(0.09)	0.60(0.09)	<0.25		6.68(0.10)	3.22(0.13)
	−5 26 00.0	0.66(0.09)	0.40(0.08)	0.44(0.08)	<0.24		6.48(0.11)	2.26(0.16)
Orion KL	05 32 47.0	1.93(0.04)	1.46(0.04)	0.99(0.04)	0.79(0.04)	<0.13	9.13(0.06)	5.61(0.07)
	−5 24 20.0	2.06(0.10)	1.41(0.10)	1.08(0.06)	0.70(0.06)		9.43(0.16)	7.53(0.18)
OMC2	05 32 59.9	0.53(0.07)	0.39(0.06)	<0.18			11.46(0.08)	1.47(0.11)
	−5 11 29.0	0.34(0.05)	0.30(0.05)	<0.12			11.17(0.07)	1.31(0.11)
S231	05 35 51.3	0.45(0.05)	0.45(0.05)	0.20(0.05)	<0.15		−16.46(0.10)	2.43(0.15)
	35 44 16.0	0.45(0.05)	0.18(0.05)	0.16(0.05)	<0.15		−16.56(0.21)	3.38(0.22)
S235	05 37 31.8	0.21(0.03)	0.11(0.03)	0.13(0.03)	<0.09		−16.90(0.13)	2.08(0.16)
	35 40 18.0	0.14(0.03)	0.14(0.03)	<0.9				
S252A	06 05 36.5	0.52(0.14)	0.47(0.14)	<0.18			8.77(0.33)	2.78(0.30)
	20 39 34.0	Not observed						
S252	06 05 53.7	0.31(0.05)	0.25(0.05)	0.10(0.04)	<0.12	<0.12	2.74(0.13)	2.11(0.23)
	21 39 09.0	0.29(0.04)	0.27(0.04)	<0.12			2.94(0.15)	2.78(0.21)
06056+2131	06 05 41.0	0.40(0.06)	0.45(0.07)	0.18(0.06)	<0.15	<0.15	2.61(0.12)	2.21(0.21)
	21 31 32.2	Not observed						

Table 2. (Contd.)

Source	RA (1950) DEC (1950)	$\int T_A^* dV$, K km s^{-1}					V_{LSR}, km s^{-1}	FWHM, km s^{-1}
		$K=0$	$K=1$	$K=2$	$K=3$	$K=4$		
NGC 2264	06 38 24.9	0.75(0.05)	0.63(0.05)	0.18(0.04)	<0.12		8.06(0.05)	2.10(0.08)
	09 32 28.0	0.57(0.05)	0.68(0.05)	0.19(0.05)	<0.15		7.97(0.08)	2.47(0.11)
L483	18 14 50.6	0.22(0.07)	0.25(0.06)	<0.10	<0.10	<0.10	5.11(0.14)	0.96(0.12)
	−04 40 49.0	Not observed						
G29.95−0.02	18 43 27.1	0.71(0.08)	0.47(0.08)	0.31(0.08)	<0.21	<0.15	97.35(0.21)	3.78(0.21)
	−02 42 36.0	0.44(0.08)	0.44(0.08)	0.30(0.07)	<0.21			
G30.70−0.06	18 44 58.9	1.15(0.09)	0.95(0.09)	0.44(0.08)	0.33(0.08)	<0.24	91.27(0.19)	4.53(0.19)
	−02 04 27.0	Not observed						
G30.8−0.1	18 45 11.0	1.43(0.08)	1.36(0.08)	0.58(0.08)	0.52(0.07)	<0.6	98.00(0.00)	5.35(0.20)
	−01 57 57.0	1.49(0.15)	1.42(0.15)	0.85(0.14)	0.51(0.13)	<0.09	97.83(0.31)	6.01(0.37)
G34.26+0.15	18 50 46.1	2.32(0.12)	2.42(0.12)	1.27(0.10)	0.49(0.10)	<0.3	57.64(0.15)	6.02(0.17)
	01 11 12.0	2.26(0.12)	2.16(0.12)	1.03(0.11)	0.54(0.11)	<0.3	57.91(0.13)	4.75(0.15)
G35.19−0.74	18 55 40.8	1.52(0.07)	1.30(0.07)	0.62(0.03)	0.34(0.04)	<0.18	33.61(0.01)	3.37(0.08)
	01 36 30.0	0.98(0.09)	0.88(0.09)	0.43(0.08)	<0.24		33.63(0.01)	4.16(0.19)
W49N	19 07 49.9	0.79(0.88)	2.41(0.84)	0.73(0.14)	0.94(0.15)	<0.42	7.14(1.69)	13.49(0.77)
	09 01 14.0	Not observed						
G43.80−0.13	19 09 30.8	0.57(0.06)	0.44(0.05)	0.28(0.05)	<0.12	<0.12	44.41(0.28)	5.04(0.28)
	09 30 47.0	Not observed						
W51 E1/E2	19 21 26.2	2.70(0.19)	2.56(0.18)	1.49(0.07)	1.18(0.08)	0.23(0.07)	57.79(0.22)	9.93(0.16)
	14 24 43.0	2.89(0.36)	2.16(0.34)	1.26(0.10)	0.97(0.10)		59.85(0.43)	10.73(0.26)
W51 MET1	19 21 26.2	1.17(0.13)	0.97(0.13)	<0.36	<0.27	<.27	55.03(0.22)	3.92(0.24)
	14 23 32.0	1.31(0.15)	0.93(0.14)	<0.39				
W51 MET2	19 21 28.8	1.52(0.14)	1.54(0.15)	0.98(0.15)	<0.39	<0.39	54.64(0.19)	4.36(0.27)
	14 23 47.0	1.24(0.35)	1.15(0.30)	0.62(0.16)	0.64(0.10)	<0.21	55.53(0.87)	9.10(0.80)
W51 MET3	19 21 27.5	1.30(0.15)	1.50(0.15)	0.45(0.15)	<0.45		53.84(0.21)	3.50(0.00)
	14 23 52.0	2.42(1.41)	1.41(1.49)	0.85(0.20)	<0.48		55.91(2.89)	7.88(1.15)
W51 MET4	19 21 25.6	1.06(0.05)	0.81(0.05)	0.25(0.05)	0.30(0.05)	<0.15	61.77(0.12)	4.33(0.15)
	14 25 41.0	Not observed						
W51 MET5	19 21 20.5	2.25(0.05)	1.13(0.05)	0.75(0.05)	0.39(0.05)	<0.15	67.08(0.73)	9.34(0.73)
	14 24 12.0	Not observed						

Table 2. (Contd.)

Source	RA (1950) DEC (1950)	$\int T_A^* dV$, K km s^{-1}					V_{LSR}, km s^{-1}	FWHM, km s^{-1}
		$K=0$	$K=1$	$K=2$	$K=3$	$K=4$		
19410+2336	19 41 04.2	0.34(0.07)	0.34(0.05)	0.18(0.06)	<0.18	<0.18	22.55(0.13)	1.98(0.18)
	23 36 42.0	Not observed						
Onsala1	20 08 09.9	1.24(0.11)	1.18(0.10)	0.58(0.10)	0.39(0.10)	<0.27	11.17(0.12)	3.42(0.13)
	31 22 42.0	1.24(0.07)	0.98(0.07)	0.53(0.07)	0.31(0.07)	<0.21	11.05(0.09)	3.60(0.11)
20126+4104	20 12 40.96	0.55(0.03)	0.41(0.02)	0.15(0.02)	0.11(0.02)	<0.06	−3.64(0.04)	2.46(0.07)
	41 04 20.6	Not observed						
20188+3928	20 18 50.6	1.02(0.09)	0.87(0.08)	0.43(0.08)	0.35(0.08)	<0.24	1.46(0.07)	2.11(0.12)
	39 28 18.6	Not observed						
20286+4105	20 28 40.6	0.45(0.05)	0.45(0.05)	<0.15	<0.15	<0.15	−4.04(0.17)	3.36(0.20)
	41 05 38.1	Not observed						
W 75N	20 36 50.4	0.96(0.08)	1.05(0.08)	0.44(0.08)	<0.24		9.03(0.13)	3.71(0.14)
	42 27 23.0	0.68(0.05)	0.60(0.05)	0.16(0.05)	<0.12		9.34(0.13)	3.67(0.13)
DR 21 West	20 37 07.6	0.50(0.04)	0.45(0.04)	0.16(0.03)	<0.12		−2.39(0.06)	2.04(0.09)
	42 08 46.0	0.32(0.05)	0.21(0.05)	0.14(0.04)	<0.12		−2.16(0.23)	3.21(0.33)
DR 21(OH)	20 37 13.8	1.72(0.02)	1.45(0.02)	0.72(0.01)	0.43(0.01)	0.06(0.01)	−3.00(0.03)	5.87(0.03)
	42 12 13.0	1.59(0.03)	1.30(0.03)	0.60(0.02)	0.32(0.02)	<0.22	−4.11(0.08)	6.46(0.08)
S140	22 17 41.2	1.09(0.05)	1.07(0.05)	0.44(0.05)	0.16(0.05)	<0.15	−6.62(0.04)	2.46(0.06)
	63 03 43.0	1.00(0.06)	0.69(0.06)	0.29(0.05)	0.17(0.05)	<0.15	−6.74(0.07)	2.88(0.11)
Cep A	22 54 19.2	1.56(0.10)	1.26(0.10)	0.80(0.10)	0.34(0.09)	<0.27	−10.70(0.09)	3.35(0.11)
	61 45 47.0	0.89(0.07)	0.88(0.07)	0.43(0.07)	<0.21		−10.58(0.10)	3.19(0.11)
23032+5937	23 03 16.9	0.23(0.07)	0.29(0.07)	<0.18	<0.18	<0.18	−51.91(0.34)	2.99(0.43)
	59 37 38.9	Not observed						
23033+5951	23 03 19.7	0.48(0.06)	0.49(0.06)	<0.20	<0.20	<0.20	−52.94(0.13)	2.83(0.19)
	59 51 55.0	Not observed						
NGC 7538	23 11 36.6	0.55(0.03)	0.46(0.03)	0.21(0.03)	0.11(0.03)	<0.09	−57.19(0.08)	3.36(0.10)
	61 11 50.0	0.34(0.05)	0.24(0.05)	0.12(0.04)	<0.15		−57.53(0.18)	2.89(0.22)
NGC 7538S	23 11 36.1	1.73(0.07)	1.27(0.06)	0.60(0.06)	0.40(0.06)	<0.18	−55.99(0.10)	4.09(0.09)
	61 10 30.0	1.15(0.07)	0.67(0.07)	0.25(0.07)	0..32(0.07)	<0.20	−55.76(0.13)	3.50(0.00)
23133+6050	23 13 21.5	0.24(0.07)	0.12(0.05)	<0.15	<0.15	<0.15	−56.30(0.19)	1.90(0.39)
	60 50 45.6							

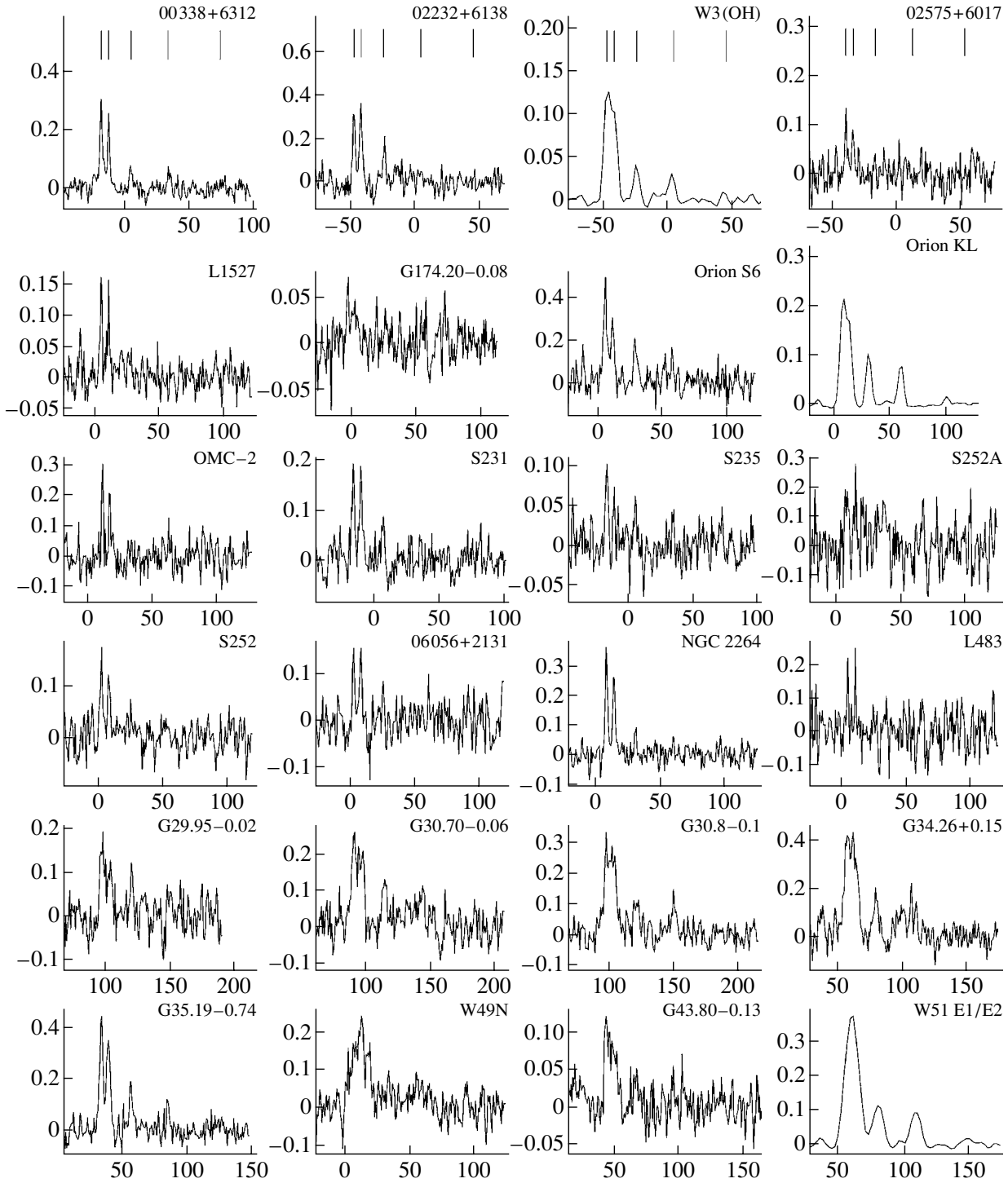

Fig. 1. Spectra of the sources detected in the 6_K–5_K lines. The horizontal and vertical axes plot the LSR velocity of the 6_0–5_0 line in km/s and the antenna temperature in Kelvins. The vertical lines in the upper row indicate the positions of various K components (the K values increase to the right from 0 to 4).

latter case, the line intensities are approximately an order of magnitude higher than the observed intensities; hence, models with $\tau \sim 1$ are possible only if the CH_3CCH emission is significantly diluted. Note that the gas temperatures derived from models with $\tau \sim 1$ are only slightly lower than those derived from the rotational diagrams. Below we will assume that the methyl acetylene lines are optically thin.

The last column of Table 3 presents the methyl acetylene abundances N_{CH_3CCH}/N_{H_2} derived using

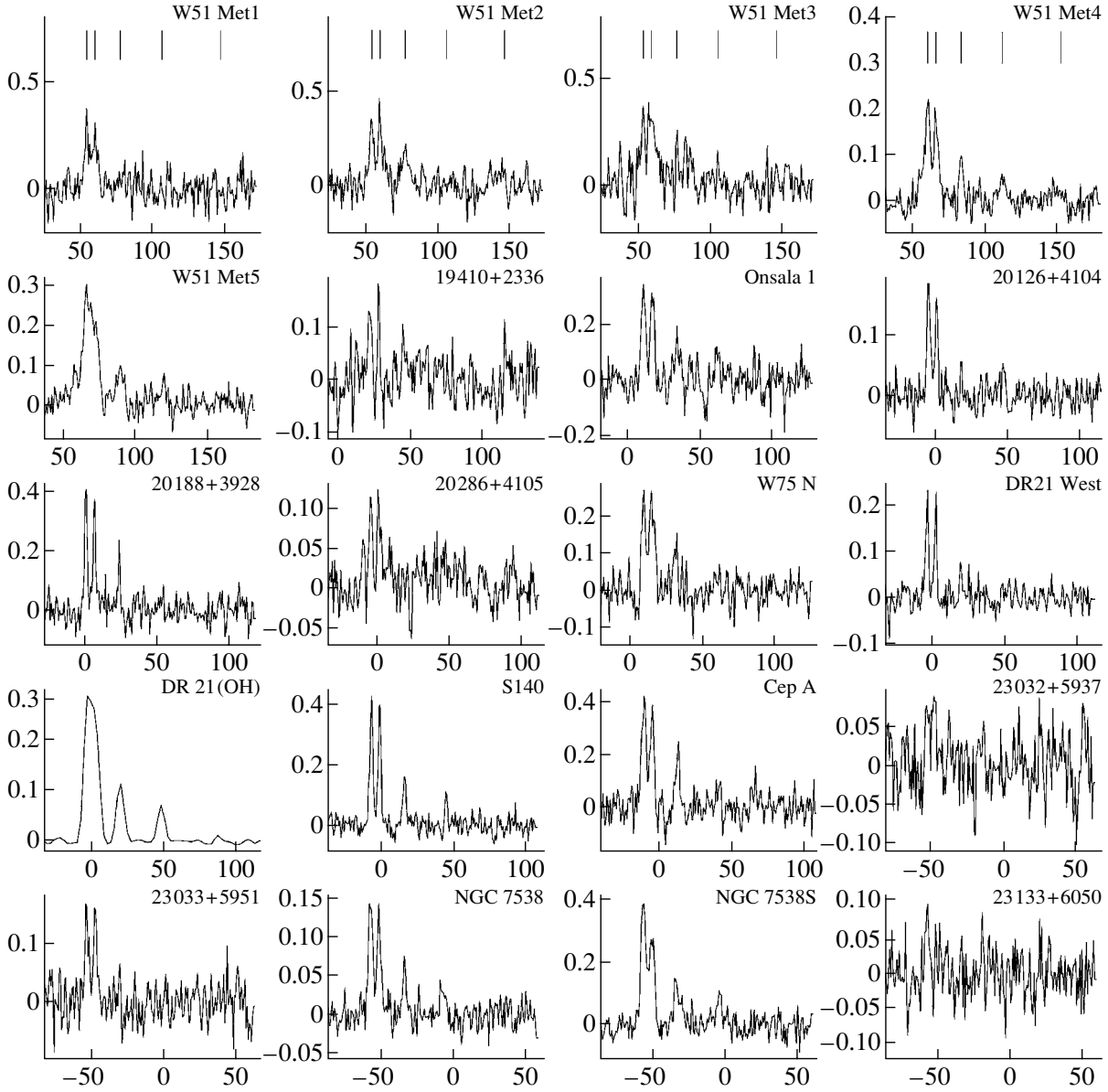

Fig. 1. (Contd.)

observations of the 1–0 ^{13}CO line at 110 GHz, also obtained at the Onsala Space Observatory [6]. The ^{13}CO and H_2 column densities were calculated assuming that the 1–0 ^{13}CO lines are optically thin, the gas temperatures are equal to the CH_3CCH rotational temperatures, and the ^{13}CO abundance is 1.7×10^{-6} [13].

3.1. The Mapping Technique

We mapped five methyl acetylene sources at 102 GHz: NGC 2264, G30.8–0.1, G34.26+0.15, DR 21(OH), and S140. In each, we observed 50–100 positions with 10 and 20 arcsec spacings in right ascension and declination. For each source, we tried to expand the observed area until the emission disappeared at the edges, but, due to our limited observing time, we could not observe sufficiently large areas toward G30.8–0.1 and DR 21(OH). Therefore, the maps of these two sources and the source parameters derived using these maps are somewhat unreliable.

Since the beam was fairly large (about 40″) and the signal-to-noise ratio was often fairly low, the obtained images were heavily smoothed by the beam and distorted by noise. Therefore, we reconstructed images of the sources using the maximum-entropy method.

The reconstruction of an image distorted by noise and smoothed by the beam is an ill-posed problem,

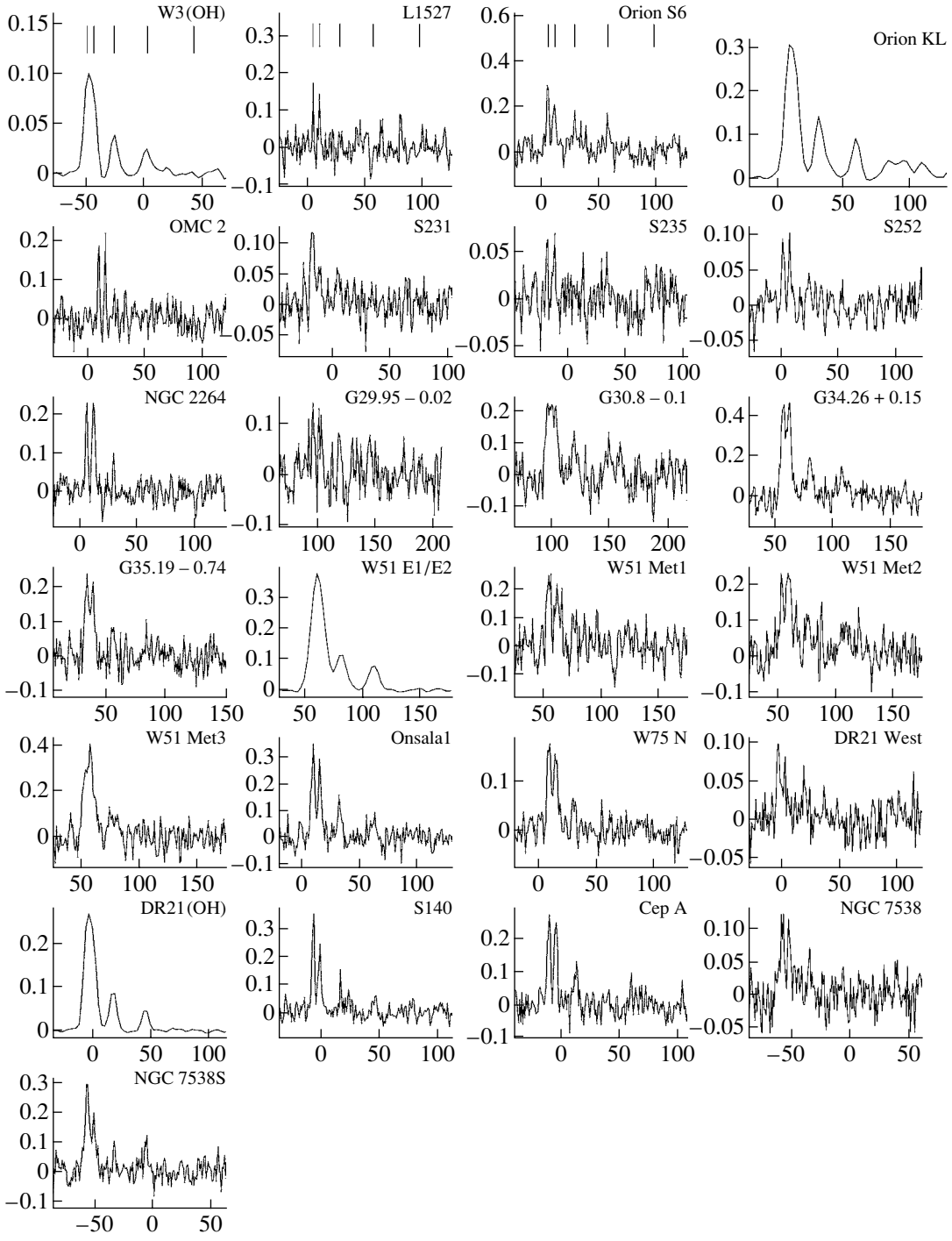

Fig. 2. Spectra of the sources detected in the 5_K–4_K lines. The horizontal and vertical axes plot the LSR velocity of the 5_0–4_0 line in km/s and the antenna temperature in Kelvins.

since high spatial frequencies are lost due to the limited spatial resolution, and there is no way to uniquely restore such an image (in other words, an infinite number of initial images can match the observed smooth image). The maximum-entropy method selects from the multitude of acceptable images with the maximum Shennon entropy

$$E(f) = -\sum_{i=1}^{N} f_i \log f_i, \qquad (1)$$

where f_i is the intensity of an element of the image. We used the version of the method described

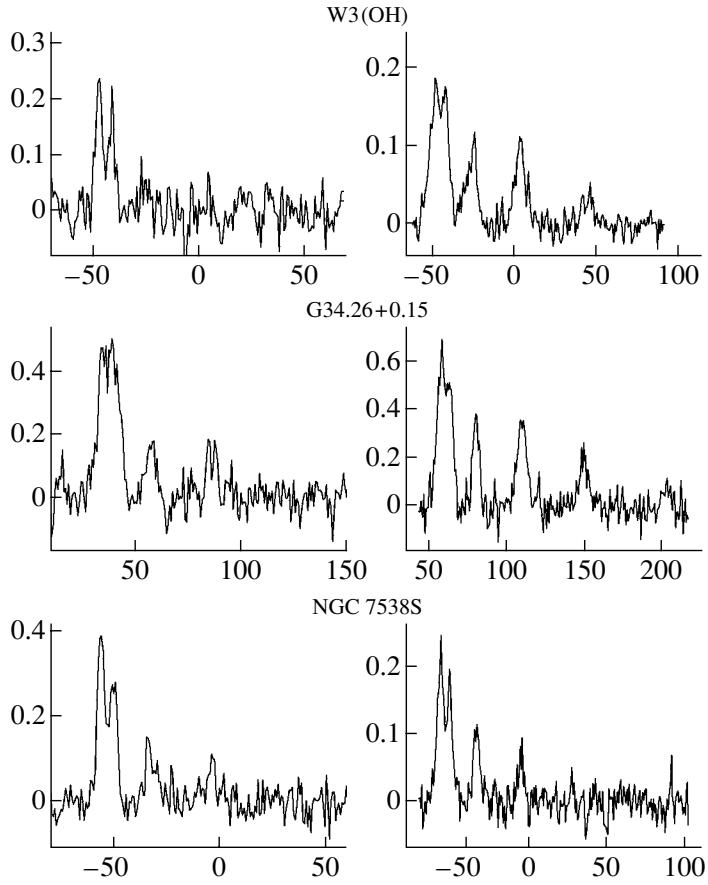

Fig. 3. Comparison of CH_3CCH and CH_3CN spectra (left and right columns, respectively).

by Wilczek and Drapatz [14], except for the computational algorithm used to solve the optimization problem. The evolutionary algorithm we employed is described by Promislov [15]. This algorithm is more computationally intensive than the algorithm of [14], but may converge in cases of poor signal-to-noise ratio or insufficient grid spacing for which the algorithm of [14] fails. Nevertheless, among the observed lines, only the blends of the 6_0–5_0 and 6_1–5_1 lines had sufficiently high signal-to-noise ratios to enable mapping. We mapped the intensity integrated over all the channels occupied by these blends (Fig. 6).

The resolution of the maps was estimated as follows. We subtracted the contribution of the source convolved with the beam at each point in the map, leaving only noise. We then added the contribution of a point source with the observed flux located at the peak of the reconstructed image convolved with the beam. Finally, we applied the image-reconstruction procedure to this map. The size of the resulting image was adopted as the map resolution. The resolutions of all the maps were about 15–25 arcsec, significantly less then the source sizes. Therefore, the angular diameters in Table 4 represent the real sizes of the sources.

3.2. Comments on Individual Sources

NGC 2264. The peak of the CH_3CCH emission coincides with the IR source IRS1 [24] and continuum sources at 130 and 70 μm [25]. The CH_3CCH source is slightly extended to the southwest of the peak, and approximately coincides with the CS, $C^{18}O$, CO, and CH_3OH sources [25]; however the second peak approximately 30″ to the southwest of IRS1 in the $C^{18}O$, CS, and CH_3OH maps is not present in our map.

G34.26+0.15. The CH_3CCH source is essentially circular, with a diameter of 50″. The emission peak coincides with an ultracompact HII region [26] and with the SO peak [27], but is shifted approximately 9″ to the southwest of the HCO^+ peak.

DR 21(OH). The methyl acetylene peak coincides with the continuum sources MM1 and MM2 [21] and the peaks of the H_2CO, $C^{18}O$, and CS emission [22, 23]. The methyl acetylene source is extended north–south by more than 2 arcmin, like the $C^{18}O$ source [21]. However, due to our limited observing time, we could not map the entire source, and the

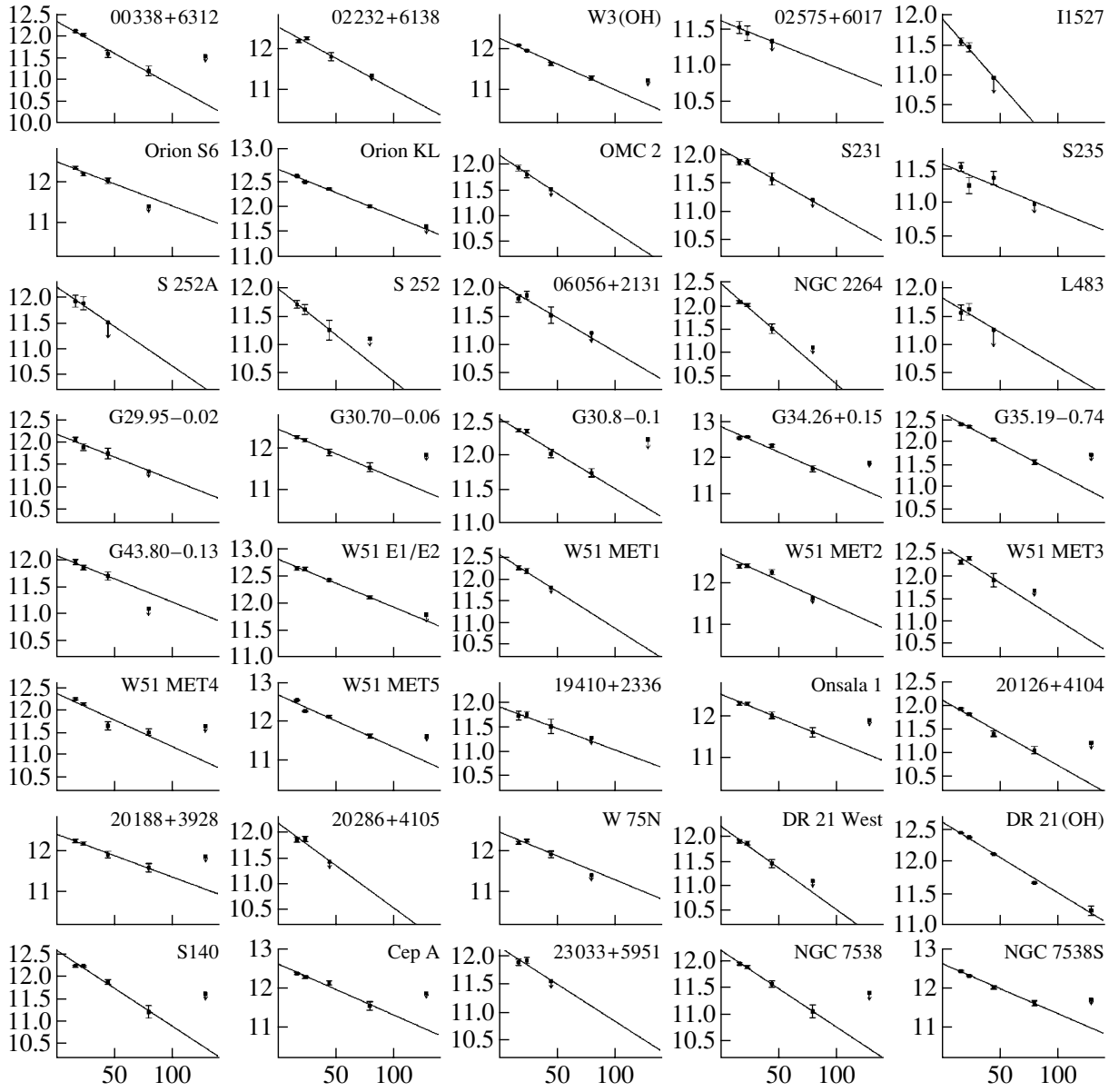

Fig. 4. Rotational diagrams for the 6_K–5_K lines. The horizontal axis plots the upper level energies divided by the Boltzmann constant, E_u/k, and the vertical axis the upper level populations divided by the statistical veights $\frac{\log(3kW)}{8\pi^3\nu_0 S\mu_{ul}^2 g_I g_k}$. The arrows denote upper limits to the upper level populations of undetected lines at the 3 σ level.

emission does not reach the background level at the northern edge of our map.

S140. This source is slightly extended northeast–southwest; the emission peak coincides with the IR source IRS1 [16]. Our map agrees fairly well with the ^{12}CO maps [17, 18], however, the peak of the CH_3CCH emission is 10–15 arcsec to the east of the ^{13}CO, C^{18}O, and HCO^+ peaks [19, 20].

3.3. Source Parameters Derived from the Maps

We derived the virial masses of the mapped sources by treating each source as a uniform, optically thin, nonmagnetized sphere with constant density. According to [28], under these assumptions, the virial mass can be calculated using the formula

$$M_{\rm vir} = 0.509d \times \mathbf{\Theta}_S \times \mathbf{\Delta}v_{1/2}^2, \qquad (2)$$

where Θ_S is the source angular diameter in arcsec, $\Delta v_{1/2}^2$ is the full width at half maximum (FWHM) in km/s, d is the source distance in kpc, and $M_{\rm vir}$ is the cloud virial mass in solar masses. The angular diameter of each source was estimated as follows. We first calculated the map area (in arcsec^2) within the contour corresponding to the intensity half-

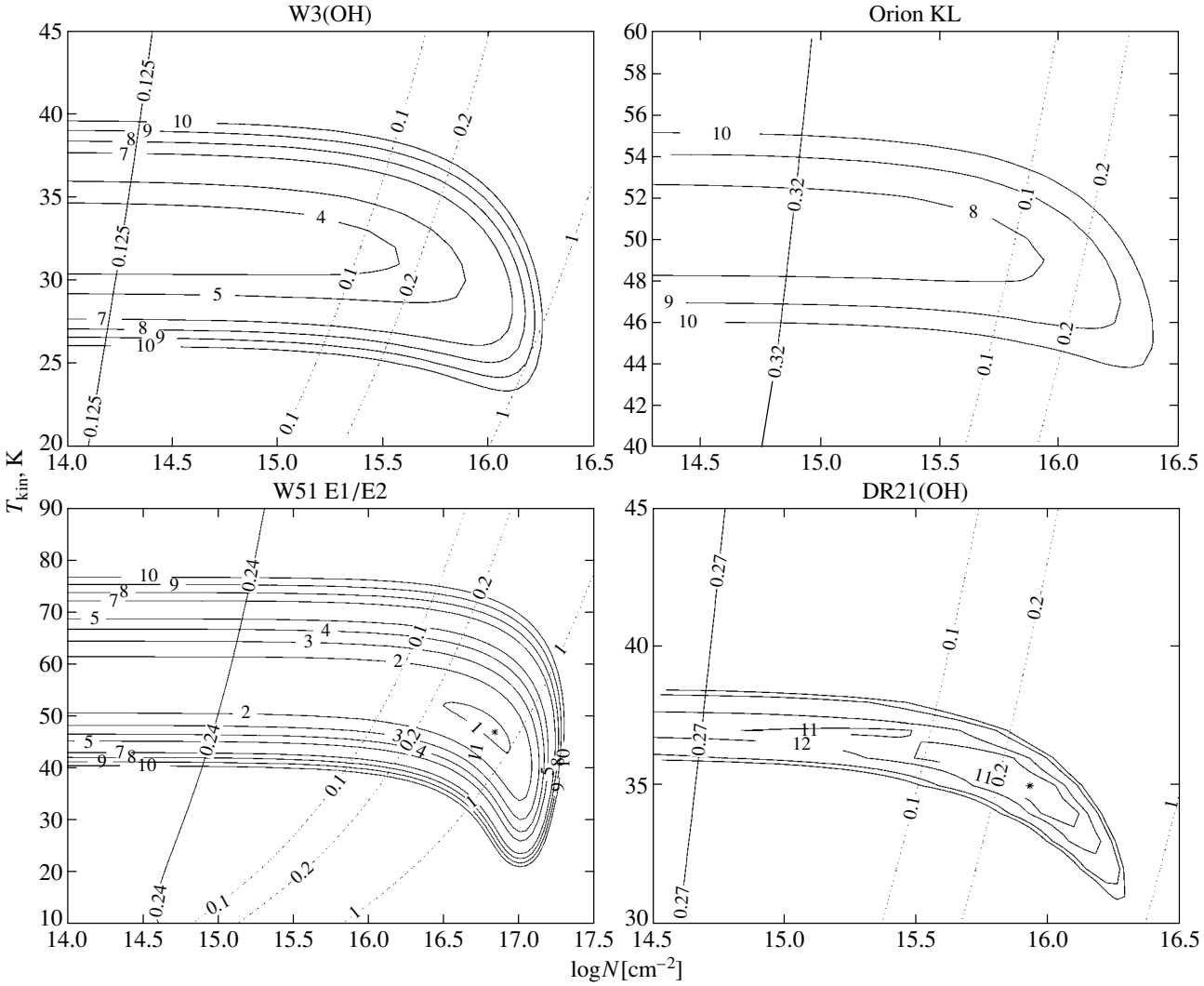

Fig. 5. Parameters of the sources determined by the χ^2 method. The contours show the derived χ^2 values, and the oblique solid lines correspond to parameter sets yielding brightness temperatures for the 6_0-5_0 line equal to the observed value. The dotted lines correspond to parameter sets for which the optical depths of the 6_0-5_0 line are 0.1, 0.2, and 1.

maximum. This area was multiplied by $\cos\delta$ to obtain the source area in the sky A. The angular diameter was calculated using the formula $\Theta^2 = 4A/\pi$, and then multiplied by 1.155 to obtain the diameter of the spherical source from the visual diameter [29]. The source distance was derived using the Galactic rotation curve of [30].

The masses determined from (2) are presented in Table 4. In addition, we estimated the masses of these same sources using the ^{13}CO column densities, assuming that the ^{13}CO and CH_3CCH sources are spatially coincident and the 1–0 ^{13}CO lines are optically thin. These masses are also presented in Table 4. For all sources except G34.26+0.15, the virial masses coincide with the masses derived from the ^{13}CO column densities within a factor of two. The comparison of the intensities of the ^{13}CO and C^{18}O lines of G34.26+0.15 presented in [31] leads to the conclusion that the ^{13}CO lines are not optically thin. Hence, the derived ^{13}CO column density and mass of this source are underestimated.

Since the two different methods yield similar mass estimates for four sources, we believe that these estimates are correct.

Assuming that the masses of the sources are equal to their virial masses and using the source sizes and methyl acetylene column densities from Tables 3 and 4, we estimated the gas densities and methyl acetylene abundances (Table 4). The densities are close to 10^5 cm^{-1}, and the methyl acetylene abundances are of the order of several $\times 10^{-9}$. Thus, the derived methyl acetylene abundances agree to within a factor of two with those in Table 3 in all sources except G34.26+0.15. We already mentioned that the ^{13}CO

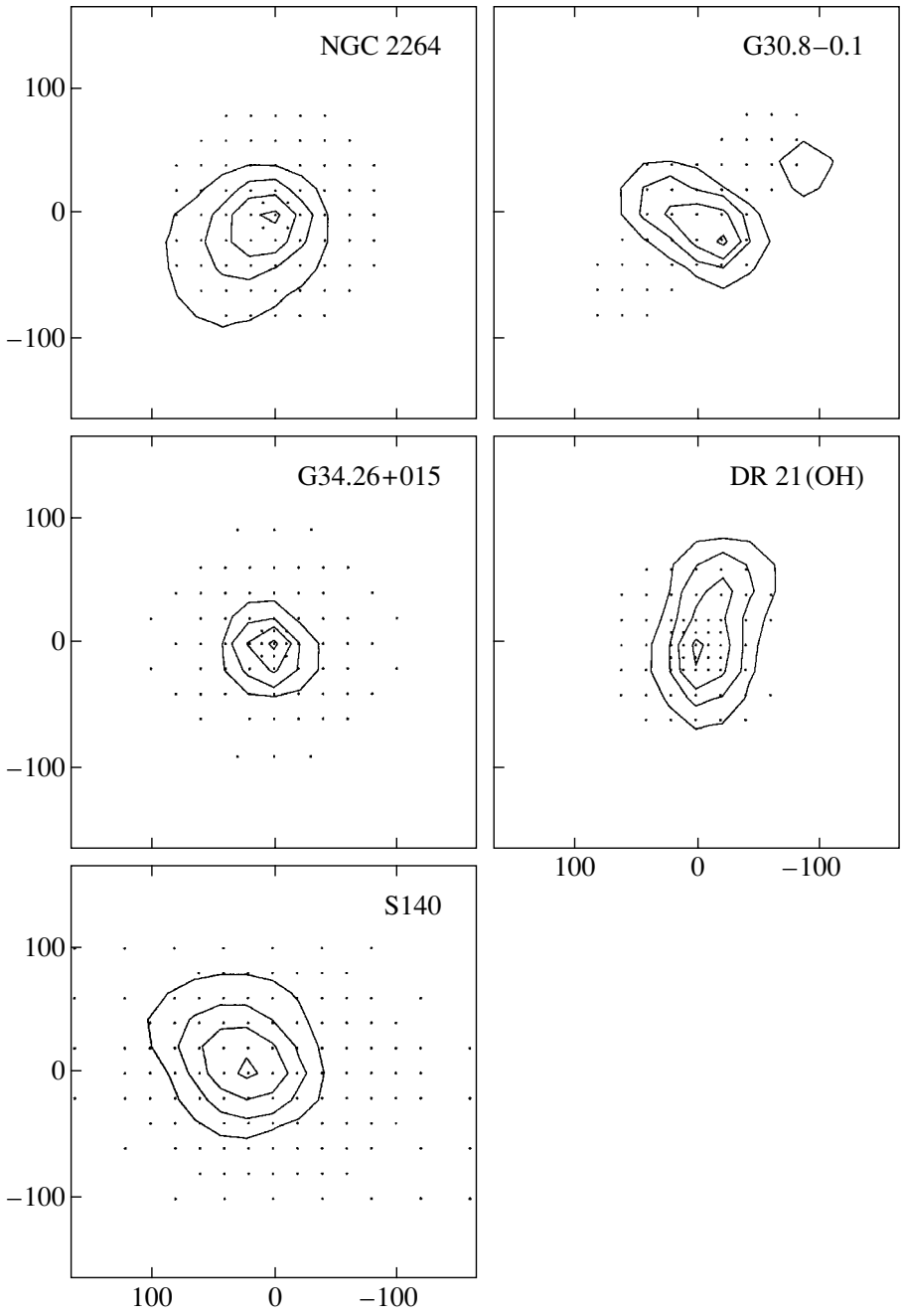

Fig. 6. Images of five sources reconstructed using the maximum-entropy method. The horizontal and vertical axes plot RA and DEC offsets in arcsec from the central positions presented in Table 1. The observed positions are marked by dots.

column density in this source is probably underestimated. In this case, the methyl acetylene abundance in Table 3 is overestimated, and the value of 3.6×10^{-9} presented in Table 4 is more correct.

Our methyl acetylene abundances are in agreement with abundance estimates for the warm gas in Orion [32, 34], Sgr B2 [33, 34], and S140 [34], and with the abundance estimate for the cold cloud TMC-1 based on $C^{18}O$ and methyl acetylene observations [35].

3.4. Simulations of Chemical Evolution

We used the derived gas temperatures and densities to model the chemical evolution of the mapped objects. The chemical reaction network corresponded to the so-called "new standard model" [36]. The code for the simulations was kindly provided by R. Terzieva (Ohio University). The model took into account only gas-phase chemistry, without allowance for dust grains. The initial set of chemical elements corresponded to a low metal abundance [36], and

Table 3. Rotational temperatures and column densities derived from the methyl acetylene observations. The CH_3CCH abundances were estimated from the column densities determined using the 6_K-5_K lines.

Source	102 GHz		85 GHz		CH_3CCH abundance, 10^{-9}
	T_{rot}, K	N_{CH_3CCH}, 10^{14}	T_{rot}, K	N_{CH_3CCH}, 10^{14}	
00338+6312	29(1)	1.9(0.2)			
02232+6138	29(3)	2.6(0.5)			
W3(OH)	35(0.7)	2.0(0.1)	42.5(2)	2.6(0.2)	2.3
02575+6017	<67(41)	<1.2(1.2)			
L1527	<20(3)	<0.4(0.1)			
ORI S6	41(6)	4.4(1.0)	<65 (22)	<4.5(2.3)	5.2
Orion KL	51(1)	8.0(0.3)	52 (4)	10.5(1.3)	
OMC2	<30(6)	1.3(0.4)	<34 (15)	<1.1(0.8)	4.1
S231	38(8)	1.5(0.5)	29 (11)	1.1(0.7)	4.8
S235	<61(11)	<1.0(0.3)			1.1
S252A	<28(10)	<1.3(0.9)			
S252	27(6)	0.7(0.3)	<42 (22)	<1.3(1.0)	2.1
06056+2131	36(10)	1.4(0.6)			
NGC 2264	20(1)	1.5(0.2)	46 (20)	3.1(2.0)	3.9
L483	<36(20)	0.8(0.7)			
G29.95−0.02	43(10)	2.3(0.9)	67 (25)	3.5(2.1)	2.0
G30.70−0.06	37(2)	3.5(0.4)			
G30.8−0.1	42(2)	5.1(0.5)	50 (10)	8.2(2.6)	5.7
G34.26+0.15	31(1)	7.2(0.5)	40 (4)	9.3(1.7)	16
G35.19−0.74	32(1)	4.3(0.3)	44 (14)	4.4(2.3)	8.5
G43.80−0.13	50(13)	2.3(1.0)			
W51 E1/E2	49(3.5)	12 (1.5)	48 (5.5)	13.3(2.7)	3.6
W51 MET1	<26(4)	<2.8(1.6)	<26 (9)	<3.1(1.7)	
W51 MET2	<34(2)	<6.5(2.2)	69 (19)	9.4(4.6)	
W51 MET3	26(4)	3.5(1.0)	34 (25)	7.4(9.8)	2.5
W51 MET4	37(1)	2.8(0.2)			
W51 MET5	32(0.5)	4.9(0.2)			
19410+2336	40(25)	1.5(1.3)			
Onsala 1	39(3)	4.2(0.6)	39 (5)	4.7(0.9)	6.1
20126+4104	31(1)	1.3(0.1)			
20188+3928	<42(3)	<3.6(0.5)			
20286+4105	<26(3.7)	<1.1(0.3)			
W 75N	38(6)	3.4(0.9)	29 (8)	1.9(0.9)	24
DR 21 West	26(3)	1.2(0.2)	41 (19)	1.2(0.9)	2.6
DR 21 (OH)	39(0.2)	5.4(0.1)	34 (1)	5.2(0.3)	4.5
S140	26(1)	2.8(0.2)	29 (3)	2.6(0.5)	4.5
Cep A	33(1)	4.6(0.4)	53 (18)	5.2(2.8)	5.7
23033+5951	<34(7)	<1.5(0.5)			
NGC 7538	31(1)	1.5(0.1)	32 (13)	1.0(0.7)	1.9
NGC 7538S	34(1)	4.6(0.3)	37 (5)	3.8(0.8)	5.2

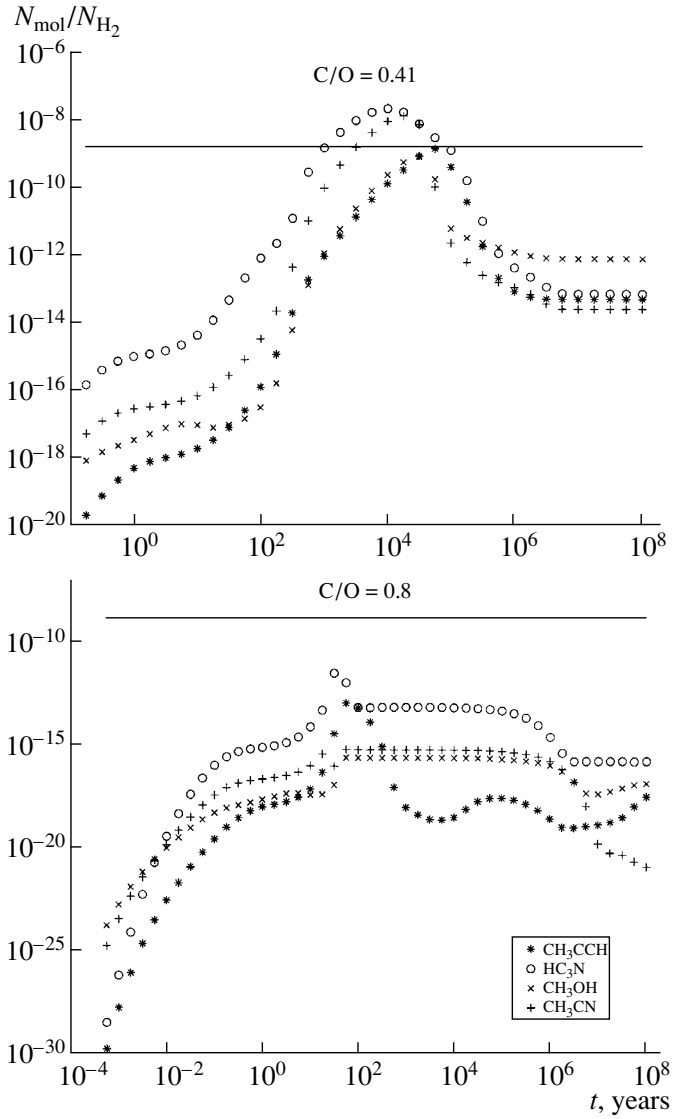

Fig. 7. The results of our chemical-evolution simulations for NGC 2264.

is presented in Table 5. We carried out simulations for the two C/O ratios 0.41 and 0.8. The results for NGC 2264 are shown in Fig. 7; the results for other sources are similar. For C/O = 0.41, the CH_3CCH abundance reaches its maximum at $t_m \sim 6 \times 10^4$ years after the beginning of the evolution; later, the abundance decreases by several orders of magnitude, reaching a steady state at $t \geq 10^7$ years. When the C/O ratio is increased to 0.8, both t_m and the maximum CH_3CCH abundance decrease. A comparison of the CH_3CCH abundance (Table 3) with the results of our simulations shows that the abundances arising near the peak at $t_m \sim 6 \times 10^4$ years correspond to those for the observed molecular clouds. The same time dependences are typical of many other molecules [36]. This implies the presence of a large amount of "chemically young" gas in giant molecular clouds.

In their study of dark clouds, Kuiper *et al.* [37] considered a model with chemically different shells, in which the source consists of a chemically more evolved core surrounded by a less evolved shell with high abundances of CH_3CCH and other molecules. Such differentiation could result from the accretion of rarefied gas. Chemical processes in the rarefied gas proceed much more slowly than in the core; in addition, ultraviolet radiation quickly destroys the molecules formed. Due to the stable influx of "chemically young" material, the shell chemical composition is characterized by high abundances of CH_3CCH and other molecules. However, in neither of the mapped sources could we find any signs of a shell structure. Apparently, this model is not applicable to warm

Table 4. Parameters of the mapped sources: (1) source name, (2) distance, (3) angular diameter, (4) linear diameter, (5) virial mass, (6) mass derived from ^{13}CO observations, (7) density estimated from virial mass, (8) CH_3CCH abundance estimated from virial mass and CH_3CCH column density.

Source	d, (kpc)	Θ	D, 10^{18} (cm)	M_{vir}, $M_\odot$	M_{CO}, $M_\odot$	n_{H_2}, 10^{-9} cm^{-3}	CH_3CCH, abundance 10^{-9}
NGC 2264	0.7	57″	0.6×10^{17}	89	40	4.8	1.6
G30.8−0.1*	6.3	53	5.0	6208	4919	0.56	4.7
G34.26+0.15	3.8	42	2.4	2332	528	1.9	3.6
DR 21(OH)*	3.0	56	2.5	1336	1941	0.96	7.7
S140	0.9	49	0.36	135	67	5.5	2.1

* Unreliable parameters (see description of the construction of the source maps in the text).

clouds. Note, however, that, in all sources except NGC 2264, it could be that we are not able to detect the shell structure due to insufficient spatial resolution.

Another possible explanation of this chemical age is related to the fact that luminous stars can form in the cloud cores over a time of $\approx 10^5$ years. The radiation of these stars leads to dissipation of the cores. Alternatively, it may be that some processes (e.g., eddy diffusion) increase the C and C^+ abundances in the clouds at late stages of their evolution, which, in turn, increases the abundances of various molecules. A review of these and some other possibilities is presented by Bergin *et al.* [38].

Table 5. Low-metallicity initial abundances of various elements relative to hydrogen (H_2)

Element	C/O = 0.41	C/O = 0.8
He	1.4000×10^{-1}	1.4000×10^{-1}
N	2.1400×10^{-5}	2.1400×10^{-5}
O	1.7600×10^{-4}	1.7600×10^{-4}
C^+	7.3000×10^{-5}	1.4080×10^{-4}
S^+	8.0000×10^{-8}	8.0000×10^{-8}
Si^+	8.0000×10^{-9}	8.0000×10^{-9}
Fe^+	3.0000×10^{-9}	3.0000×10^{-9}
Na^+	2.0000×10^{-9}	2.0000×10^{-9}
Mg^+	7.0000×10^{-9}	7.0000×10^{-9}
e	7.3107×10^{-5}	7.3107×10^{-5}
P^+	3.0000×10^{-9}	3.0000×10^{-9}
Cl^+	4.0000×10^{-9}	4.0000×10^{-9}

4. CONCLUSIONS

As a result of our survey of Galactic star-forming regions in the 6_K–5_K and 5_K–4_K methyl acetylene lines at 102 GHz and 85 GHz, we have detected 44 sources at 102 GHz and 25 sources at 85 GHz.

Using rotational diagrams, we estimated the gas kinetic temperatures and methyl acetylene abundances for the sources. The kinetic temperatures are 20–60 K and coincide within the errors with temperatures estimated from methanol, methyl acetylene, and ammonia observations. The methyl acetylene column densities for most of the sources lie in the range $(1-5) \times 10^{14}$ cm^{-3}. No emission of hot cores—compact massive regions with gas temperatures above 100 K—was found.

Using our maximum-entropy images of five sources, we estimated the sizes, masses, and densities of these sources. The sizes were about 0.1–1 pc, the masses were hundreds to thousands of solar masses, and the densities were about 10^5 cm^{-3}. Thus, we observed warm and dense clouds in the methyl acetylene lines.

Thus, warm (20–60 K), dense (10^5 cm^{-3} or higher) are observed in the methyl acetylene lines.

Our chemical-evolution simulations show that the characteristic methyl acetylene abundances in these clouds correspond to a chemical age for the gas of $\approx 6 \times 10^4$ years.

ACKNOWLEDGMENTS

The authors are grateful to the Onsala Observatory staff for help during the observations, R. Terzieva for making available the code for the simulations of the chemical evolution of molecular clouds, and Dr. V.I. Slysh for helpful discussions. This work was partially supported by the Russian Foundation for Basic Research, project nos. 98-02-16916 and 01-02-16902; the Radio Astronomy Educational and

Scientific Center, project 315; and INTAS, grant 97-11451. The Onsala Space Observatory is the Swedish National Facility for Radio Astronomy, and is operated by the Chalmers University of Technology, Göteborg, Sweden, with financial support from the Swedish Natural Science Research Council and the Swedish Board for Technical Development.

REFERENCES

1. L. Olmi, R. Cesaroni, R. Neri, and C. M. Walmsley, Astron. Astrophys. **315**, 565 (1996).
2. S. V. Kalenskiĭ, A. M. Dzura, R. S. Booth, *et al.*, Astron. Astrophys. **321**, 311 (1997).
3. T. Y. Wang, J. G. A. Wouterloot, and T. L. Wilson, Astron. Astrophys. **277**, 205 (1993).
4. A. Bauer, D. Boucher, J. Burie, *et al.*, J. Phys. Chem. Ref. Data **8**, 537 (1979).
5. J. Askne, B. Höglund, A. Hjalmarson, and W. M. Irvine, Astron. Astrophys. **130**, 311 (1984).
6. S. V. Kalenskiĭ, V. G. Promislov, A. V. Alakoz, *et al.*, Astron. Zh. **77**, 819 (2000) [Astron. Rep. **44**, 725 (2000)].
7. R. Mauersberger, C. Henkel, T. L. Wilson, and C. M. Walmsley, Astron. Astrophys. **162**, 199 (1986).
8. E. Churchwell, C. M. Walmsley, and R. Cesaroni, Astron. Astrophys., Suppl. Ser. **83**, 119 (1990).
9. S. Molinari, J. Brand, R. Cesaroni, and F. Palla, Astron. Astrophys. **308**, 573 (1996).
10. J. G. A. Wouterloot, C. M. Walmsley, and C. Henkel, Astron. Astrophys. **203**, 367 (1988).
11. K. Schreyer, T. Henning, C. Kompe, and P. Harjunpaä, Astron. Astrophys. **306**, 267 (1996).
12. T. L. Wilson and R. Mauersberger, Astron. Astrophys. **239**, 305 (1990).
13. R. Lucas and H. Liszt, Astron. Astrophys. **337**, 246 (1998).
14. R. Wilczek and S. Drapatz, Astron. Astrophys. **142**, 9 (1985).
15. V. G. Promislov, in *Advances in Soft Computing—Engineering Design and Manufacturing,* Ed. by R. Roy, T. Furuhashi, and P. K. Chawdhry (Springer-Verlag, London, 1999).
16. N. J. Evans, L. G. Mundy, M. L. Kutner, and D. L. DePoy, Astrophys. J. **346**, 212 (1989).
17. R. L. Snell, N. Z. Scoville, D. B. Sanders, and N. R. Erickson, Astron. Astrophys. **315**, 565 (1984).
18. N. R. Minchin, G. J. White, and R. Padman, Astron. Astrophys. **277**, 595 (1993).
19. N. R. Minchin, G. J. White, and D. Ward-Thompson, Astron. Astrophys. **301**, 894 (1995).
20. D. J. Wilner and W. J. Welch, Astrophys. J. **427**, 898 (1994).
21. S. Padin, A. I. Sargent, L. G. Mundy, *et al.*, Astrophys. J. **337**, L45 (1989).
22. K. J. Johnston, C. Henkel, and T. L. Wilson, Astrophys. J. **285**, L85 (1984).
23. J. G. Mangum, A. Wootten, and L. G. Mundy, Astrophys. J. **378**, 576 (1991).
24. A. I. Sargent, R. J. Van Duinen, H. L. Nordh, *et al.*, Astron. Astrophys. **135**, 377 (1984).
25. K. Schreyer, F. P. Helmich, E. F. van Dishoeck, and Th. Henning, Astron. Astrophys. **326**, 347 (1997).
26. J. M. Benson and K. J. Johnston, Astrophys. J. **277**, 181 (1984).
27. P. Carral, W. J. Welch, and M. C. H. Wright, Rev. Mex. Astron. Astrofis. **14**, 506 (1987).
28. R. Cesaroni, E. Churchwell, P. Hofner, *et al.*, Astron. Astrophys. **288**, 903 (1994).
29. N. Panagia and C. M. Walmsley, Astron. Astrophys. **70**, 411 (1978).
30. L. Brand and L. Blitz, Astron. Astrophys. **275**, 67 (1993).
31. L. T. Little, A. G. Gibb, D. B. Heaton, *et al.*, Mon. Not. R. Astron. Soc. **271**, 649 (1994).
32. G. A. Blake, E. C. Sutton, C. R. Masson, and T. G. Phillips, Astrophys. J. **315**, 621 (1987).
33. E. Churchwell and J. M. Hollis, Astrophys. J. **272**, 591 (1983).
34. T. B. H. Kuiper, E. N. Rodríguez Kuiper, D. F. Dickinson, *et al.*, Astrophys. J. **276**, 211 (1984).
35. P. Pratap, J. E. Dickens, R. L. Snell, *et al.*, Astron. Astrophys. **486**, 862 (1997).
36. H. H. Lee, R. P. A. Bettens, and E. Herbst, Astrophys. J., Suppl. Ser. **119**, 111 (1996).
37. T. B. H. Kuiper, W. D. Langer, and T. Velusamy, Astrophys. J. **468**, 761 (1996).
38. E. A. Bergin, P. F. Goldsmith, R. L. Snell, and W. D. Langer, Astrophys. J. **482**, 285 (1997).

Translated by S. Kalenskiĭ

Astronomy Reports, Vol. 46, No. 7, 2002, pp. 567–578. Translated from Astronomicheskiĭ Zhurnal, Vol. 79, No. 7, 2002, pp. 627–639.

H_2O and HDO Bands in the Spectra of Late-Type Dwarfs

Ya. V. Pavlenko

Main Astronomical Observatory, ul. Akademika Zabolotnogo 27, Kiev, 03680 Ukraine

Received September 5, 2001; in final form, October 23, 2001

Abstract—We discuss techniques and results of computations of the infrared spectra of late-type dwarfs. Our computations of the synthetic spectra and spectral energy distributions in the infrared ($\lambda\lambda$ 1–10 μm) were carried out assuming LTE, using the grids of M- and L-dwarf model atmospheres of Allard and Hauschildt (1995) and Tsuji (1998), taking into account the opacities due to H_2O and HDO absorption bands. We discuss the use of HDO bands formed in the infrared spectra of cool dwarfs to realize the "deuterium test" recently proposed for the identification of substellar-mass objects and large planets and to refine scenarios for the evolution of young stars and substellar objects. © *2002 MAIK "Nauka/Interperiodica".*

1. INTRODUCTION

1.1. Formulation of the Problem

The infrared spectra of many objects display H_2O absorption lines. These are formed at a wide range of temperatures and densities realized in the atmospheres of the Earth and other planets in the solar system, sunspots, comets, giant molecular clouds, flows of matter from star-forming regions, and active galactic nuclei (see references in [1]).

On the other hand, absorption by the H_2O molecule largely determines the character of long-wavelength blanketing in late-type stars on the oxygen sequence, i.e., in the region where their spectral energy distributions (SEDs) have their maxima. Thus, accurate account of H_2O absorption becomes a key issue in model atmosphere computations for these cool stars.

Until recently, it was believed that M dwarfs were the most numerous objects among late-type stars, comprising up to 80% of the total number of stars in the Galaxy (cf. [2]). However, the total number of low-mass objects is probably higher: recent discoveries of brown dwarfs and low-mass stars with $T_{\rm eff} < 2200$ K (Kelu1) [3], objects detected in the DENIS [4] and 2M [5] surveys have added significantly to our understanding of such ultra-cool objects. It was recently suggested to introduce a new spectral type L for objects with $T_{\rm eff} = 2200$–1200 K [5, 6]. The spectra of L dwarfs are characterized by the weakening or complete disappearance of TiO and VO molecular absorption bands. The optical SEDs of such stars are determined by very strong resonance potassium and sodium lines [7, 8], with H_2O bands dominating in the IR [9]. Methane absorption lines and bands are present in the spectra of still cooler objects with $T_{\rm eff} < 1200$ K, such as Gl 229B [10]. It has been proposed to introduce the spectral classification T for such objects [11]. There is no doubt that studies of the infrared spectra of M, L, and T dwarfs are of crucial importance for our understanding of their nature and evolution.

One task of the current study is to investigate the applicability of the "deuterium test" for the classification of low-mass objects in our Galaxy. The deuterium test is largely analogous to the so-called lithium test. It is currently believed that the rate of depletion of lithium and deuterium in the interiors of low-mass stars is primarily determined by the mass of the star or substellar object. For stars ($M > 75M_J$, where $M_J \approx 0.001\ M_\odot$ is the mass of Jupiter), the burning of lithium, Li (p, α) ^{4}He, becomes efficient at early evolutionary stages preceding the main sequence at interior temperatures of $T \sim 2.5 \times 10^6$ K [12]. Young, low-mass stars possess developed convective envelopes, so that lithium depletion in their central regions is manifest on relatively short time scales (several tens of million years) as a weakening or complete disappearance of lithium lines in their spectra. The temperatures in the interiors of lower-mass (i.e., substellar) objects—brown dwarfs ($M < 60M_J$)—are not high enough for lithium burning. Thus, in principle, their primordial lithium abundance should not change with time. This circumstance led to the idea of the lithium test [13], which essentially consists of searching for lithium absorption lines in the spectra of late M dwarfs as evidence of their substellar nature. The practical applicability of the lithium test was demonstrated in [14]. Subsequently, the lithium test was successfully used to prove the substellar nature of several late-type dwarfs [3, 15, 16].

1063-7729/02/4607-0567$22.00

The lithium abundances in the atmospheres of young stars are also of interest for other problems. In particular, the position of the line in the Hertzsprung–Russell diagram separating stars burning lithium from lower-mass objects that still have lithium in their atmospheres can be used to derive independent age estimates for young open clusters with ages $t < 150$ million years[1] [16–19]. The prospects for applying the lithium test to the identification of brown dwarfs among L dwarfs were studied by Pavlenko *et al.* [20].

In turn, deuterium is burned in stellar interiors in the reaction $^2\mathrm{D}(p,\gamma)^3\mathrm{He}$ at lower temperatures ($T > 8 \times 10^5$ K) than Li. This means that the temperatures in the interiors of substellar objects with $M < 13M_J$ are insufficient for deuterium burning. Their deuterium abundances have remained unchanged since their formation [21–23].

This fact makes it possible to define planets as objects with no deuterium burning (or lithium burning) in their interiors. Deuterium burns inside brown dwarfs, which distinguishes them from planets [21]. In higher-mass objects such as stars, deuterium burning is completed comparatively quickly ($t \sim 1$–3 million years) [12, 23] during the evolution prior to the star's period on the main sequence. Naturally, the deuterium depletion rate depends on the mass of the star or brown dwarf.

The deuterium test was suggested in [23, 24] to isolate planets among low-mass objects. In practice, it was proposed to search for absorption lines of molecules containing deuterium (HDO, CrD, FeD, etc.) in the spectra of low-mass objects.

The recent discovery of such objects in the solar neighborhood [25] increased interest in the idea of using these deuterium-containing molecules for the classification of extremely cool objects. It is not possible to observe lines of the deuterium atom itself (in absorption or emission, blended with the hydrogen L_α lines) due to the very nature of substellar objects: their photospheres are immersed in "coats" of cool matter [8] that effectively absorbs ultraviolet radiation. On the other hand, deuterium emission lines should arise at significant distances from these objects, where the matter may be enriched in deuterium from the interstellar medium.

Of course, in principle, the deuterium test can also be used to investigate other problems. For instance, the position of the line separating objects that still contain deuterium from those whose deuterium has all been burned can be used to determine the ages of open clusters within several million years. At these early stages of evolution, the luminosity of low-mass objects exhibits a strong time dependence [12, 23].

Thus, the deuterium test can be used in connection with at least three problems:

(1) identifying planets in samples of low-mass objects (naturally, this is possible only for very nearby objects with $T_{\mathrm{eff}} < 1000$ K);

(2) clarifying the evolutionary status of young objects in open clusters with ages of several million years;

(3) studying evolutionary changes of the deuterium abundances in low-mass substellar objects (such investigations can usefully be combined with the lithium test).

Overall, the practical realization of the deuterium test is much more complex than for the lithium test. These difficulties will be discussed in Section 3. Section 2 presents results of computations of H_2O absorption bands and a comparison with the bands observed in the spectrum of the M dwarf VB10 (M8V). In the first section, we present information on existing lists of water lines, and discuss some details of our computations of H_2O absorption lines and bands in the IR spectra of late-type dwarfs.

1.2. Lists of H_2O Absorption Lines

The concept of developing astrophysical applications for lists of H_2O absorption lines was suggested by Auman [26], who used the ensemble of known characteristics of this molecule's levels and transitions (line intensities, molecular constants, relative band intensities) to compute the opacity due to band absorption. His study was made possible by the publication of the laboratory data of Ludwig [27] and Ludwig *et al.* [28]. Auman [26] computed averaged (direct mean) absorption coefficients in H_2O bands in the IR. His use of relatively simple techniques to take into account the H_2O absorption was necessitated by the incompleteness of the existing data on the relevant molecular transitions, as well as computational limitations.

The appearance of more advanced techniques for taking opacity into account—such as sampling opacities and opacity distribution functions (see the review [29])—gave rise to the necessity for more refined computations using more complete lists of H_2O lines, so that their positions (and, ideally, intensities) would coincide with those measured in laboratory and/or stellar spectra [30].

*Line lists of J{o*rgensen. The first versions of the list [30] contained 85 000 lines originating from levels with energies below 30 000 cm^{-1}. They were computed using the assumptions of the MORBID theory [30]. The level energies were determined as

[1] This corresponds to the time needed for a solar-mass star to reach the main sequence.

sums of components describing physical characteristics of the rigidly rotating molecule and its deformations that brought the theoretical data and laboratory measurements into agreement. This list was used in model-atmosphere computations for late-type stars for a number of years [30].

A modification of Jørgensen's line list appeared in 2001 (see [31]; cf. also ftp://stella.nbi.dk/pub/scan). The complete list includes three billion lines; however, Jørgensen *et al.* [31] suggest that 100 million lines should be fully sufficient for most astrophysical problems. Thus far, this list has been used to reproduce the low-dispersion IR spectra of red giants. The list is probably not suitable for studies requiring a description of the fine structure of rotational–vibrational H_2O bands (Section 3.1; see also [32]).

The HITRAN line list. Work on composing a list of H_2O lines that is as complete as possible based on the experimentally measured characteristics of this molecule's levels and transitions is ongoing.

One source of such data is HITRAN [33]—a database containing absorption lines for many molecules, including H_2O. The latest version of the database includes up to 51 930 lines (cf. http://www.hitran.com; earlier versions are described in [34]). The HITRAN data are restricted to rotational quantum numbers $j < 20$ and level excitation energies $E'' < 6000$ cm^{-1}. This database was originally intended for analyses of telluric molecular lines formed at relatively low temperatures ($\approx$300 K). For this reason, HITRAN does not include transitions from levels with $j > 20$. Naturally, this leads to a deficiency of lines in the theoretical stellar spectra compared to observations [30].

The HITEMP line list. The HITEMP database is essentially a high-temperature analog of HITRAN. In particular, it contains information on H_2O lines formed in transitions between water levels at $T_{\rm eff} >$ 296 K.

Line list of Miller et al. The line list of Miller *et al.* [36] contains $\sim$6.4 million lines, and takes into account transitions from lower rotational levels with $j < 30$ and energies below 11 000 cm^{-1}. The computations used to compile this list applied approaches based on variational computations, claimed in [36] to be more accurate than extrapolation or approximation techniques [37]. Miller *et al.* [36] computed the H_2O energy levels, dipole moments, and wave function in the Born–Oppenheimer approximation using precisely such variational methods.

However, the above lists did not enable satisfactory reproduction of the observed H_2O bands in the IR spectra of M dwarfs [38].

Line list of Viti, Tennyson, and Polyansky. Attempts to compile a better list of H_2O lines were continued by Viti *et al.* [1]. This requires correct computation of the characteristics of rotational levels with large j quantum numbers, based on a correct determination of the potential energy surfaces [37]. Viti *et al.* [1] claim that the new version of their list includes all transitions from levels to 30 000 cm^{-1} ($\lambda > 0.2$ μm), with uncertainties $\sim$0.1 cm^{-1}.

Line list of Partridge and Schwenke (AMES). Prior to the new list of Jørgensen [31], the list of H_2O lines computed by Partridge and Schwenke [39] (AMES) was considered to be most complete (it contains 307 721 352 lines). This list was computed *ab initio*, using modified potential energy surfaces and theoretical dipole moments chosen so that the computed positions of the H_2O absorption lines coincided with the HITRAN data. Therefore, this list essentially includes the HITRAN list: 66% of the observed transitions were reproduced with accuracies better than 0.05 cm^{-1}. Moreover, the detailed analysis in [39] demonstrated that about 3% of all lines in HITRAN96 had incorrect wavelengths.

Partridge and Schwenke acknowledge the possible presence of imperfections in the AMES line list [39]. They note, in particular, the growth of computational uncertainties with increasing angular momentum. The data on the H_2O levels were derived by optimizing the potential energy surfaces for levels with $j < 5$. It is possible the existing uncertainties can be reduced via further refinement of the potential energy surfaces for higher j values.

In general, the AMES line positions demonstrate good agreement with the HITRAN data, though the line intensities can differ. However, the profiles of vibrational H_2O bands computed using these lists and averaged over the rotational structure show fairly good agreement. In Section 3.1, we present the results of applying the HITRAN [33], AMES [39], and Jørgensen *et al.* [31] line lists to compute the H_2O spectra. Synthetic spectra computed using the AMES, Miller *et al.* [36], and Viti *et al.* [1] lists have been compared by Jones *et al.* [32]. The AMES database [39] was used by Kurucz [40] to compile a list of H_2O lines suitable for model atmosphere computations.

The AMES database also contains data on HDO transition systems. These data were derived under the same assumptions as for H_2O, but the number of HDO levels taken into account was lower than the number of H_2O levels. This circumstance affects the computed sums over states of the HDO molecule (see Section 2.3). In addition, the positions of the HDO lines show poorer agreement with the HITRAN values: the rms error of the transition energies corresponding to the HDO lines is 0.25 cm^{-1} [39].

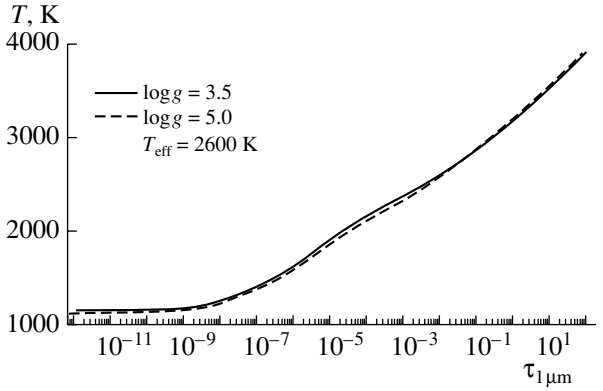

Fig. 1. Temperature in the 2600/3.5 and 2600/5.0 M-dwarf model atmospheres [43] as a function of the 1 μm optical depth.

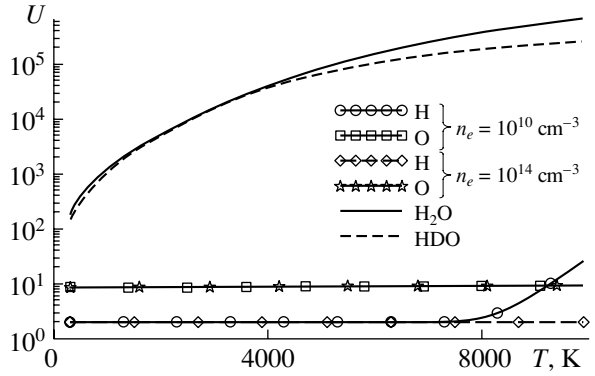

Fig. 2. Sums over states for hydrogen, oxygen, and the H_2O and HDO molecules.

2. COMPUTATIONAL METHOD

Our computations of synthetic spectra[2] for late-type dwarfs used the WITA6 code [41] and classical assumptions: LTE, with no energy sources or sinks in the plane-parallel medium. We took into account both absorption and scattering of photons when solving the equations of radiative transfer. The microturbulence velocity was assumed not to vary with depth: $v_t = 2$ km/s.

Individual lines were described using Voigt profiles. When computing the damping constant, we took into account natural damping, van der Waals broadening, and Stark broadening (cf. [42]). However, because of the low temperatures and electron densities involved, Stark broadening of the absorption lines formed in the atmospheres of cool dwarfs is negligible. The synthetic spectra were convolved with a Gaussian instrumental profile, $\exp(-(\Delta\lambda/\Delta\lambda_g)^2)/\sqrt(\pi)$.

2.1. Model Atmospheres

We used model atmospheres with $T_{\rm eff} < 3000$ K and $\log g = 3.5$–5 computed by Allard and Hauschildt [43] assuming LTE and solar composition [44] for the M dwarfs. Figure 1 shows the temperature distributions in the atmospheres of an M dwarf, $T_{\rm eff}/\log g = 2600/3.5$, and a subgiant, 2600/5.0, in terms of the optical depths $\tau_{1\mu{\rm m}}$[3].

For the L dwarfs, we used the model atmospheres computed by Tsuji [45] for conditions corresponding to the independent existence of dust and the gas components, i.e. for $r_* > r_{\rm crit}$, where r_* is the size (radius) of the dust grains and $r_{\rm crit}$ is their critical size, corresponding to the equilibrium state of the dust–gas phase transition. The existence of a dust component in the relatively cool ($T \sim 1000$ K) plasma of the L-dwarf atmospheres is due to the realization of a gas–dust phase transition for some molecular species at high pressures [46].

2.2. Ionization and Dissociation Equilibrium

We solved the system of equations for the ionization and dissociation equilibrium for a medium consisting of atoms, ions, and molecules. The computations took into account about 100 components. As in [41], we applied the technique implemented by Kurucz [47, 48] in his ATLASxx codes[4] when computing the chemical equilibrium in the atmospheres of late-type stars. In this approach, the equilibrium (LTE) number densities of a molecule consisting of atoms $x, y, \ldots z$ in the kth ionization state are computed using the Gouldberg–Waage relations:

$$n^{k+}_{xy\ldots z}/(n_x * n_y * \ldots n_z) \qquad (1)$$
$$= B_{xy\ldots z} * B^k_e/(B_x * \ldots * B_z) * \exp(-E_{xy\ldots z}/T_{ev}),$$

where M_i and n_i are the mass and number of particles in cm^{-3} of the ith component, $B_i = (2\pi M_i * kT/h^2)^{3/2}$, $B_e = 2 * (2\pi m_e * kT/h^2)^{3/2}$, and $E_{xy\ldots z}$ and T_{ev} are the molecule's dissociation potential and the temperature (in eV).

Equation (1) can be transformed to

$$n^{k+}_{xy\ldots z}/(n_x * n_y * \ldots n_z) \qquad (2)$$
$$= U_{xy\ldots z} * M^{3/2}_{xy\ldots z} * m_e^{k*3/2}/(U_x * \ldots * U_z$$

[2] In fact, our computations yielded the spectral energy distributions of the studied objects. However, we use the term "synthetic spectra" for the sake of clarity.

[3] At 1 μm, the monochromatic wavelength scale in the atmospheres of late-type dwarfs corresponds approximately to a scale in the Rosseland optical depths, $\tau_{\rm ross}$.

[4] Currently, at least six versions of the ATLAS code are known. For brevity, we use the notation ATLASxx for this family of codes.

Dissociation equilibrium constants of H_2O in (3)

D_o	$b, 10^2$	$c, 10^{-2}$	$d, 10^{-6}$	$e, 10^{-10}$	$f, 10^{-14}$	Source
9.500	0.9193	0.2550	0.4088	0.3893	0.1512	This paper
9.500	0.9430	0.3528	0.6966	0.6926	0.2485	Data from [49]
9.512	0.93179	2.6725	5.7830	8.5268	0.51311	[40]

$$* (M_x * \ldots * M_z)^{3/2} * (2\pi kT/h^2)^{3/2*(m-k-1)}) * \exp(-E_{xy\ldots z}/T_{ev}),$$

where U_i are sums over states for the ith component.

The input data for our dissociation-equilibrium computations were mainly taken from Tsuji [49]. For some molecules (TiO, VO, CN, CO, AlO), we recomputed these constants using tables from Gurvits *et al.* [51].

2.3. Sums over States and Chemical Equilibrium Constants for H_2O and HDO

The sums over states of the H_2O and HDO molecules computed using the data of Partridge and Schwenke [39] are a factor of three to four higher than those of other authors [49]. This is due to the degeneracies of the rotational–vibrational levels, which are taken into account by Partridge and Schwenke [39] for symmetrical and antisymmetrical levels: $g_s = 1$ and 3, respectively. In this case, the degeneracy of the ground state of the hydrogen atom is four (the degeneracies corresponding to the spins of both the electron and nucleus are equal to two), whereas the statistical weights of the levels and the oscillator strengths for the H_2O molecule are [50]

$$g = 2g_s * (2J_i + 1)/3 \text{ and } gf = g * w_m * X_{sect}.$$

Here, w_m is the angular frequency in atomic units, g_s the spin degeneracy, j_i the rotational quantum number of the lower level, and X_{sect} the dipole momentum in atomic units.

For the H_2O and HDO molecules, the dissociation potential is $E_{xyz} = 9.5$ eV [49], the ionization stage is $k = 0$, and $m = 3$; i.e., these molecules consist of three atoms. Figure 2 shows the temperature dependences of the sums over states for hydrogen, oxygen, and H_2O. Note that the sums over states for hydrogen, U_H, show a strong dependence on n_e at high temperatures ($T > 8000$ K) and low electron densities ($n_e < 10^{14}$ cm^{-3}). This is due to the higher contribution to U_H from higher hydrogen levels, since their populations increase in such conditions. However, when n_e increases, these levels are at distances above the Debye radius $r_D = 6.9 * (T/n_e)^{0.5}$, and they are not included in the sums over states.

The M- and L-dwarf model atmospheres used for our computations have temperatures not exceeding 4000 K, even at photospheric depths (Fig. 1), but electron densities reaching 10^{13} cm^{-3} and higher. Thus, we can neglect the dependence of U_H on n_e. Following Kurucz [47], we transform the complex expression containing a ratio of the sums over states for the components to

$$n_x * \ldots * n_z/n_{x\ldots z} = \exp(-E_{xy\ldots z}/T_{ev} + b - c * (T + d * (T - e * (T + f * T))) + 3/2(m - k - 1) * \ln T). \quad (3)$$

We determined the values of b, c, d, e, f via a least-squares fit. These constants for the H_2O molecule are collected in the Table, which also contains constants we computed using data from [49] and the constants used in [40].

The number densities of molecules in the atmospheres of late-type stars are known to demonstrate a strong dependence on the pressure, i.e., on $\log g$ [49]. Generally speaking, in most cases, $\log g$ can be determined for these stars only using indirect methods. A detailed discussion of this problem is beyond the scope of this paper. However, since the H_2O spectrum shows a dependence on $\log g$, we performed several numerical simulations to clarify the character of the relations. Our computations show that the molecular number densities of H_2O at a given optical depth increase with increasing $\log g$ in the atmosphere, but we must also consider variations in the continuum opacity in the IR. As a result, the intensities of the H_2O bands show a complex relation on $\log g$ (see Section 3.1).

2.4. Sources of Continuum Opacity

We used the list of continuum opacity sources presented in [20]. Note that, due to the low temperatures in the photospheres of stars with $T_{\text{eff}} < 3000$ K, the role of the H^- ions becomes considerably less compared to hotter stars. The role of other opacity sources increases in such conditions. In particular, at low temperatures and high densities, the role of absorption by molecular complexes consisting of H_2–H_2 and/or H_2–He is increased [52–54]. The role of this opacity in the formation of spectra of stars

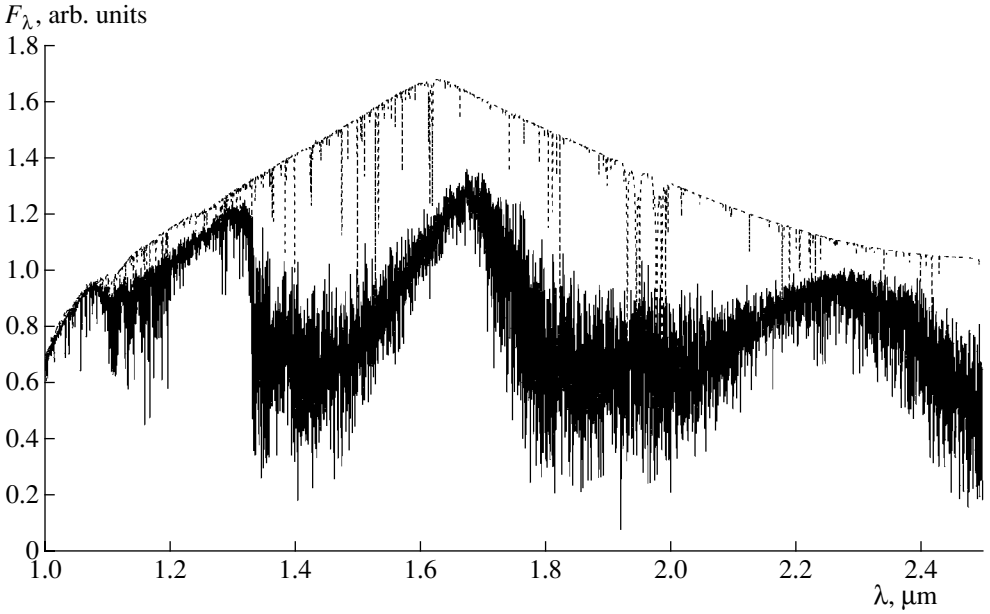

Fig. 3. Spectral energy distributions computed for the 2500/5.5 model atmosphere taking into account continuum, atomic, and H_2O absorption (solid curve), and taking into account only continuum and atomic absorption (dashed curve).

of different spectral types has been considered in a number of studies (for example, cf. [55]). We took into account opacities using cross sections obtained from the Internet: http://www.astro.ku.dk/~aborysow. We added programs to compute the corrsponding opacities to the WITA6 code.

2.5. Accounting for Absorption by Atoms and Other Molecules

The lists of atomic and ionic absorption lines were taken from the VALD database [56]. In principle, atoms absorb a relatively small fraction of the IR energy emerging from the atmospheres of M and L dwarfs compared to the absorption in H_2O bands (Fig. 3). As is noted above, the optical SEDs of M dwarfs are largely determined by absorption by electronic systems of the TiO and VO bands [57], while those of L dwarfs are determined by absorption by KI and NaI resonance lines [20, 46].

We took into account absorption by other (diatomic) molecules in the Just Overlapping Approximation (JOLA), i.e., without taking into account the rotational structure of their bands [59]. The spectroscopic constants used in our computations are described in [20].

3. RESULTS

3.1. H_2O Bands in the Spectra of M Dwarfs

We computed synthetic spectra for fairly broad wavelength ranges. In contrast to stars of earlier spectral types, the IR spectra of M and L dwarfs have virtually no intervals of continuum (Fig. 3). Therefore, a quantitative analysis of their spectra is possible (and useful) only using normalized SEDs[5].

The observed spectra of M dwarfs have their maximum fluxes at $\lambda\lambda$ 1.25, 1.68, and 2.3 μm. Absorption by H_2O bands is minimal in this region (Fig. 3). Here, individual atomic absorption lines "break through" the H_2O bands, though, in general, the atomic spectrum is much weaker than the H_2O molecular bands, and only certain subordinate metallic lines (such as the potassium doublet at $\lambda\lambda$ 1243.2273, 1252.2134 nm) have especially strong intensities.

Comparison of spectra computed for a number of M-dwarf model atmospheres from the grid [43] with the observed SED of the M dwarf VB10 (M8V, $T_{\rm eff} = \approx 2600$ K [43]) demonstrates a good qualitative agreement (Fig. 4).

Note that, in this case, the computed and observed SEDs were compared on a linear flux scale. The use of a logarithmic scale [43, 58] appears to lead to a somewhat better agreement. On the linear flux scale, deviations between the computed and observed fluxes from 1.6 to 1.8 μm do not exceed 40%. Differences in the shapes of the observed and computed SEDs in this range can be explained by incompleteness of the existing lists of water-vapor lines (Section 1.2), as well as by absorption by other molecules that are not taken into account. The fundamental systems

[5] In the sense that we compare the observed and computed fluxes reduced to an equal value at a given wavelength.

of the CO, CH, OH, CN bands are known to be an important source of opacity in the IR spectra of cool stars [61]. We will study their role in subsequent papers. In general, the H_2O bands undoubtedly dominate over a wide wavelength range in the spectra of L and M dwarfs.

The intensities of H_2O absorption bands in the IR depend on several parameters: the star's effective temperature $T_{\rm eff}$, surface gravity $\log g$, and metallicity μ. However, we assume that the elemental abundances in the atmospheres of the studied stars do not differ from the solar values. Indeed, most known low-mass objects are in the solar neighborhood, and belong to the disk population of the Galaxy.

If the effective stellar temperature changes, the relative intensities of individual H_2O absorption bands, and eventually the shape of the infrared SED, will also change (Fig. 4). At the same time, the dependence of the IR spectra of low-mass objects on $\log g$ is much less strong.

Naturally, it is especially important for the realization of the deuterium test to be able to reproduce fine details of the observed spectra for comparisons with theoretical spectra computed using various lists of H_2O lines. As indicated above, there are already more than five such line lists. Thus, such comparisons can also be used to evaluate the quality of line lists and their suitability for various problems. Of course, this requires the solution of complex problems associated with the acquisition and reduction high-quality IR spectra, which are beyond the scope of our study (see, however, [32]). Here, we are most interested in estimating the suitability of the H_2O line lists specifically for computations of reliable theoretical spectra. This question has already been investigated for some of the line lists available (see Section 1.2).

The AMES [39] and Jørgensen *et al.* [31] lists of H_2O lines are currently the most complete. To estimate their quality in the context of interpreting late-dwarf spectra, we compared spectra computed at $\lambda\lambda$ 2.4–3.1 μm for the 3100/5.5 model atmosphere. Jones *et al.* [32] were able to reproduce the observed spectra of several M dwarfs (GJ 406, GJ 699, GJ 191) in this range with fairly good accuracy using the AMES list. H_2O bands dominate in this region of the spectrum. Bands of the first overtone ($\Delta v = 2$) of the CO molecule can appear in the spectra of cool stars at $\lambda < 2.6$ μm, and begin to influence the spectra of M dwarfs at $\lambda < 2.4$ μm [32]. Figure 5 also shows the synthetic spectrum computed using the HITEMP line list. As is noted above, this list was compiled using laboratory measurements of the characteristics of the H_2O transitions.

The following results were obtained from comparisons of the H_2O lists:

(1) Fluxes in the theoretical spectra computed using the HITEMP and AMES line lists differ considerably, due to two factors:

(a) The AMES list contains more lines. The numerous weak H_2O lines form a kind of quasi-continuum, which acts as a background for the formation of stronger lines. This biases the visible line spectrum toward lower fluxes.

(b) The HITEMP H_2O lines have lower gf values. We noted above that this was due to differences in the way the quantum degeneracy of the transitions is taken into account in the AMES and HITRAN lists [50]. Nevertheless, the structure of the rotational bands computed with these line lists reproduces the observed fluxes well (see also [32]).

(2) The results for the line list of Jørgensen *et al.* [31] are worse: even the shape of the SED differs from those computed using the AMES and HITEMP line lists (Fig. 5). Moreover, the structure of the water bands does not agree with either the observations [32] or the computations using the HITRAN and AMES lists. The absolute fluxes computed using the line lists of AMES and Jørgensen *et al.* averaged over the rotational structure of the molecular bands show a good agreement [31].

We base our analysis below solely on computations with the AMES line list.

3.2. Prospects for the Deuterium Test

In addition to the strong H_2O bands, HDO bands can also be observed in the infrared. Of course, these bands should be much weaker than the H_2O bands (the cosmic ratio of the deuterium and hydrogen abundances is D/H $\sim 2 \times 10^{-5}$ [60]). Naturally, this hinders realization of the deuterium test. On the other hand, the HDO bands should be displaced relative to the H_2O bands due to the isotopic shift. In this context, spectral regions where the heads of HDO bands coincide with minimal H_2O absorption are of special interest.

Figure 6 shows the computed SEDs for a 2850/5.0 M dwarf and a 1200/5.0 L dwarf. Computations were carried out for matter consisting of H_2O (D/H = 0), HDO (D/H = 1), and for the sequence D/H = 2×10^{-5}, 1×10^{-4}, 1×10^{-3}.

Note that only the case D/H = 2×10^{-5} is of direct interest for our study. The computations with different D/H values were intended only to investigate the behavior of spectra with varying D/H ratios. An examination of different hypotheses concerning the formation and existence of objects with high D/H ratios is beyond the scope of this paper.

We briefly summarize our findings below:

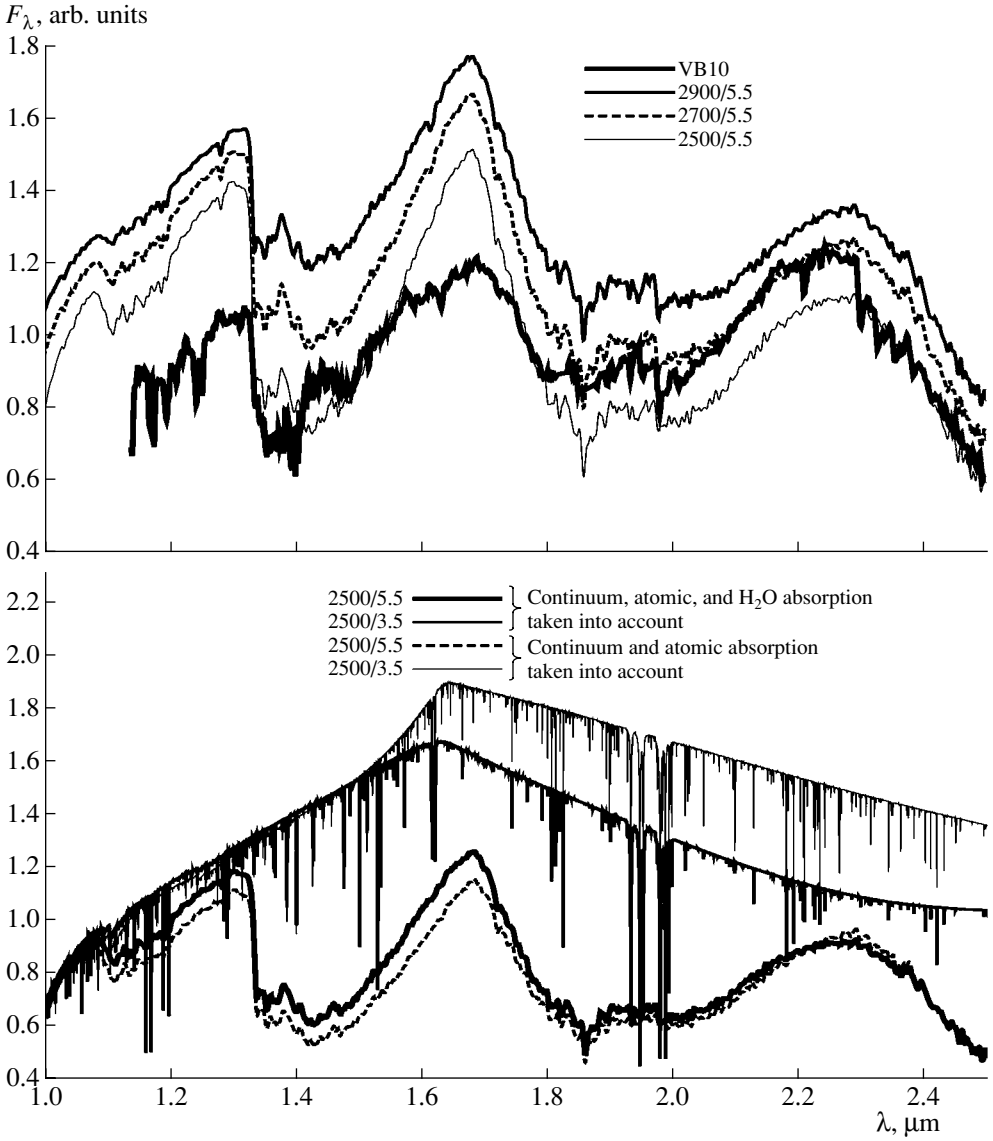

Fig. 4. Top: relation between the intensities of H_2O bands formed in the atmospheres of M dwarfs and their effective temperatures. The theoretical spectra were convolved with a Gaussian with width $\Delta_g = 40$ Å. For comparison, the observed SED of the M dwarf VB10 (M8V) [58] is shown. Bottom: dependence of the theoretical M-dwarf spectra on the surface gravity. Radiation fluxes computed without taking into account absorption in the H_2O bands are also shown.

—other things being equal, the intensities of the HDO and H_2O bands are comparable;

—the HDO molecular bands are displaced relative to the H_2O bands, with the displacement increasing toward the red;

—in the spectra of stars with $T_{\rm eff} < 2000$ K, the radiation fluxes emerging from the atmosphere at λ 1.5–3.5 μm are lower due to collisionally induced absorption by the H_2-H_2, H_2-He pairs.

Nevertheless, comparing the relative positions and intensities of the HDO and H_2O absorption bands, we can identify the spectral ranges that are most suitable for the deuterium test and determinations of the D/H isotopic ratio: 3.5–4, 5, and 6–7 μm (Fig. 6). Note also that the HDO absorption lines are able to penetrate through the H_2O spectrum when $D/H = 2 \times 10^{-5}$, though their relative intensities do not exceed several percent [23]. In general, the realization of the deuterium test is much more complicated than in the case of the lithium test.

4. DISCUSSION

The trustworthiness of our results is limited by our assumptions and the model simplifications used, as well as by the completeness of the line lists used.

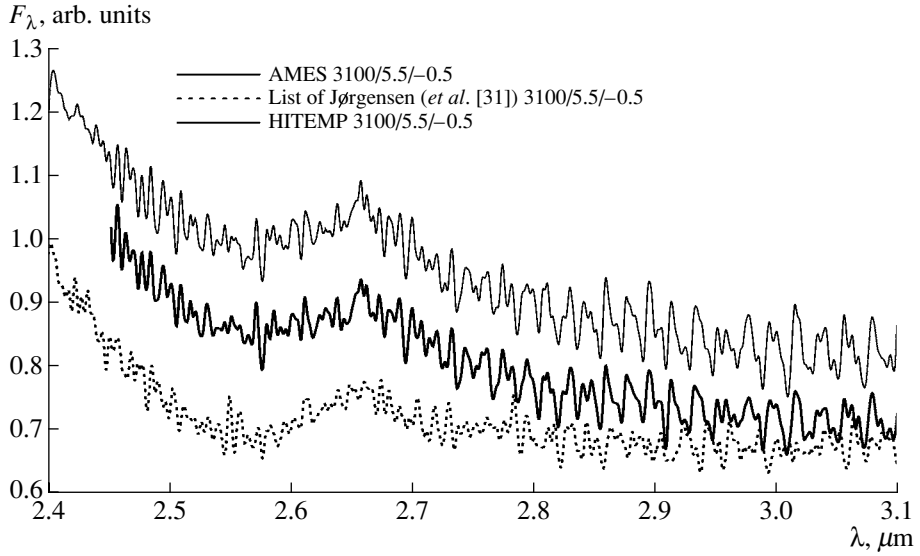

Fig. 5. Comparison of radiation fluxes, F_λ, computed for the 3100/5.5/−0.5 model atmosphere from the grid of Allard and Hauschildt [43]. The theoretical spectra were convolved with a Gaussian with width $\Delta_g = 8$ Å. We subtracted 0.1 from the radiation fluxes computed using the list of Jørgensen *et al.* [31] to simplify the figure.

Several important factors that should be taken into account in more refined studies include the following:

(1) *Model atmospheres*. The M-dwarf model atmospheres we have used were computed by Allard and Hauschildt [43] using classical assumptions. In these models, the temperature gradually decreases with depth in the atmosphere. However, for most cool dwarfs, observations provide evidence for the presence of relatively hot outer envelopes where H_α emission lines are formed. The formation of such high-temperature regions is usually thought to be a consequence of the dissipation of waves formed by the strong convective envelopes of these stars.

On the other hand, the H_2O and HDO spectrum is formed in relatively deep layers, which are probably not influenced by the hot chromospheric radiation. In fact, due to the decreasing opacity at lower $T_{\rm eff}$, there is no doubt that the photospheres of cool stars are situated under a "blanket" of cool matter with temperatures $\leq$1500 K, while the formation of emission (chromospheric) spectra is possible (by definition) at low densities. Thus, the photospheric and chromospheric layers should be more strongly separated in this case than for hotter stars (for example, the Sun).

(2) *Dust*. When $T_{\rm eff}$ drops below 2600 K, dust grains, which are a source of additional opacity, appear in the atmospheres of low-mass objects. Unfortunately, our understanding of the formation of dust grains in the atmospheres of M and L dwarfs is far from complete. Obviously, this must be a dynamical process involving the convective envelopes of these stars, in which the dust grains are effectivly dissolved. There is no doubt that a key problem in modeling dust effects is that the cross sections for the interaction of dust grains with the radiation field are determined by their chemical composition, as well as their shape. The nature of these effects is understood only qualitatively, and computations have been restricted to relatively simple models; the addition of virtually any more complex assumption to the previously adopted simplified models makes the computations exponentially more difficult. This problem may prove to be even more complex than that of interpreting non-LTE effects in stellar atmospheres.

(3) *Absorption by other molecules*. Our computations took into account absorption only by atoms and H_2O and HDO molecules. We noted above that the infrared range also contains rotational–vibrational bands of other molecules, in particular, of OH, CN, and CO [61]. Absorption in these bands can be significant in both the near-IR (CN bands) and far-IR (CO bands).

However, our study was intended to address the restricted problem of computing H_2O and HDO absorption bands in the IR spectra of late dwarfs, and of determining these molecules' intensity ratios for various D/H isotopic ratios. In other words, we were primarily concerned with differential effects, which are less dependent on the assumptions. It is also very likely that chromospheric effects and variations of the temperature structure of the model atmospheres due to dust effects also influence the H_2O and the HDO bands to comparable degrees.

Nevertheless, our results show that the spectra of ultra-cool dwarfs at $\lambda > 3$ μm possess spectral regions suitable for the deuterium test. Three such

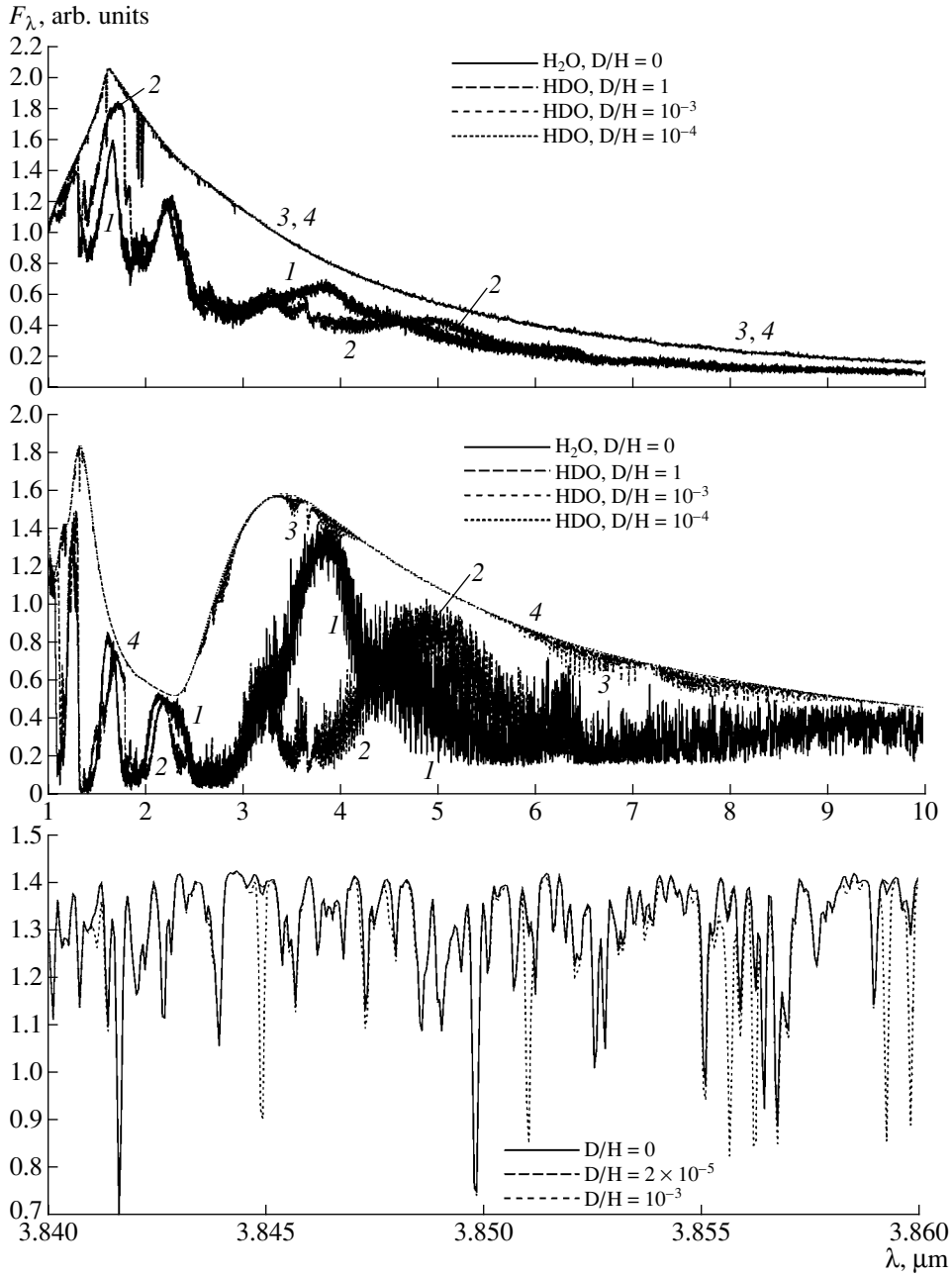

Fig. 6. SEDs for the 2600/5.0/0 [43] (upper panel) and 1200/5.0 [45] (middle panel) model atmospheres, taking into account absorption by the H_2O and HDO bands (for various isotopic ratios, D/H). The theoretical spectra were convolved with a Gaussian with width $\Delta_g = 10$ Å. The bottom panel shows the range $\lambda\lambda$ 3.84–3.86 μm for the 1200/5.0 dwarf in more detail ($\Delta_g = 0.5$ Å).

spectral regions stand out: ~3.5–4, ~5, and ~6–7 μm (Fig. 6). At these wavelengths, minimal H_2O absorption overlaps with maximum HDO absorption.

The situation is made even more difficult by the fact that the spectra of dwarfs with $T_{\rm eff} < 1500$ K should exhibit bands of CH_4 and/or other polyatomic molecules. This significantly complicates the use of HDO absorption bands and lines for the deuterium test. On the other hand, we can also expect the presence of CDH_3 lines and bands in such spectra, which can, in principle, also be used for the deuterium test. Naturally, this approach requires computations of line lists for this molecule (as well as for CH_4). A detailed analysis of this problem is beyond the scope of this paper.

Other deuterium-containing molecules (HD, CrD, FeD) can also be used to search for corresponding

lines (bands) in the spectra of celestial bodies. The use of CrD is preferable, since the spectrum of CrH has strong (0,0) bands at 8600 Å [62] whose intensity increases with decreasing $T_{\rm eff}$. At the same time, the adjacent FeH and FeD bands are blended with the CrH bands. In addition, the intensities of the FeH bands decrease at lower $T_{\rm eff}$ values.

Note that, in principle, the isotopic shifts of the CrH–CrD and FeH–FeD molecular bands should be large; these molecules have low reduced masses ($\mu \sim 1$). Moreover, the strongest CrH band is in the near-IR, and is observable with the largest currently available telescopes.

Thus, the detection of HDO absorption lines in the spectra of low-mass objects is a strong challenge for the most skilled observers. On the one hand, such observations are crucial for improving our knowledge of the nature and evolution of low-mass objects. On the other hand, we must admit that the detection of weak HDO lines with residual fluxes of several percent (at best!) is problematic, even for the largest existing telescopes. However, in principle, the deuterium test can be realized using the absorption lines (bands) of other molecules. We intend to pursue this problem in subsequent papers.

ACKNOWLEDGMENTS

The author is grateful to Dr. Victor Béjar and to Prof. Rafael Rebolo (Institute of Astrophysics, Tenerife) for useful discussions and their assistance with this study. I thank Dr. David Schwenke (NASA) for the lists of H_2O and HDO lines, Dr. Hugh Jones (University of Liverpool) for providing IR spectra of late dwarfs, and Dr. Serena Viti (University of London) for technical assistance. I am also grateful to the anonymous referee for useful remarks and to L. Yakovin (Main Astronomical Observatory, National Academy of Sciences of Ukraine) for his large contribution to improving the paper's presentation. This study was supported by a Small Research Grant of the American Astronomical Society.

REFERENCES

1. S. Viti, J. Tennyson, and O. L. Polyansky, Mon. Not. R. Astron. Soc. **287**, 79 (1997).
2. *Very Low Mass Stars and Brown Dwarfs,* Ed. by R. Rebolo and M. R. Zapatero Osorio (Cambridge Univ. Press, Cambridge, 2000), p. 1.
3. M. T. Ruiz, S. K. Leggett, and F. Allard, Astrophys. J. **491**, L107 (1997).
4. X. Delfosse, C. G. Tinney, T. Forveille, *et al.*, Astron. Astrophys. **327**, L25 (1997).
5. J. D. Kirkpatrick, I. N. Reid, J. Liebert, *et al.*, Astrophys. J. **519**, 802 (1999).
6. E. L. Martín, X. Delfosse, G. Basri, *et al.*, Astron. J. **118**, 2466 (1999).
7. Ya. V. Pavlenko, Astron. Zh. **75**, 888 (1998) [Astron. Rep. **42**, 787 (1998)].
8. Ya. V. Pavlenko, Astron. Zh. **78**, 172 (2001) [Astron. Rep. **45**, 144 (2001)].
9. F. Allard, P. H. Hauschildt, and D. Schwenke, Astrophys. J. **540**, 1005 (2000).
10. T. Nakajima, B. R. Oppenheimer, S. R. Kulkarni, *et al.*, Nature **378**, 463 (1995).
11. M. A. Strauss, X. Fan, and J. E. Gunn, Astrophys. J. **522**, L61 (1999).
12. F. D'Antona and I. Mazzitelli, in *Brown Dwarfs and Extrasolar Planets,* Ed. by R. Rebolo, E. Martín, and M. R. Zapatero Osorio, Astron. Soc. Pac. Conf. Ser. **134**, 442 (1998).
13. R. Rebolo, E. L. Martín, and A. Magazzù, Astrophys. J. **389**, L83 (1992).
14. Ya. V. Pavlenko, R. Rebolo, E. L. Martín, and G. García López, Astron. Astrophys. **303**, 807 (1995).
15. R. Rebolo, E. L. Martín, G. Basri, *et al.*, Astrophys. J. **469**, L53 (1996).
16. E. L. Martín, G. Basri, J. E. Gallegos, *et al.*, Astrophys. J. **499**, L61 (1998).
17. J. Stauffer, G. Schultz, and J. D. Kirkpatrick, Astrophys. J. **499**, L199 (1998).
18. J. Stauffer, D. Barrado y Navascues, J. Bouvier, *et al.*, Astrophys. J. **527**, 219 (1999).
19. G. Basri and E. L. Martín, Astrophys. J. **510**, 266 (1999).
20. Ya. V. Pavlenko, M. R. Zapatero Osorio, and R. Rebolo, Astron. Astrophys. **355**, 245 (2000).
21. D. Saumon, W. B. Hubbard, A. Burrows, *et al.*, Astrophys. J. **460**, 993 (1996).
22. A. Burrows, M. Marley, W. B. Hubbard, *et al.*, Astrophys. J. **491**, 856 (1997).
23. G. Chabrier, I. Baraffe, F. Allard, and P. Hauschildt, Astron. Astrophys. **542**, L122 (2000).
24. V. J. S. Bejar, M. R. Zapatero Osorio, and R. Rebolo, Astrophys. J. **521**, 671 (1999).
25. M. R. Zapatero Ozorio, V. J. S. Bejar, R. Rebolo, *et al.*, Science **290**, 103 (2000).
26. J. R. Auman, Astrophys. J., Suppl. Ser. **14**, 171 (1967).
27. C. B. Ludwig, Technical Report GDC-DBE 67-021 (Space Science Laboratory, 1967), p. 1.
28. C. B. Ludwig, W. Malkmus, J. E. Reardon, and J. A. L. Thomson, *Handbook of Infrared Radiation from Combustion Gases* (NASA, Washington, 1973), NASA SP-3080, p. 1.
29. D. Michalas, *Stellar Atmospheres* (Freeman, San Francisco, 1980).
30. U. G. Jørgensen, Rev. Mex. Astron. Astrofis. **23**, 49 (1992).
31. U. G. Jørgensen, P. Jensen, G. O. Sorensen, and B. Aringer, Astron. Astrophys. **372**, 249 (2001).
32. H. Jones, Ya. Pavlenko, S. Viti, and J. Tennyson, Mon. Not. R. Astron. Soc. **330**, 675 (2002).
33. L. S. Rothman, R. R. Gamache, A. Goldman, *et al.*, Appl. Opt. **26**, 4058 (1987).

34. L. S. Rothman, R. R. Gamache, R. H. Tipping, *et al.*, J. Quant. Spectrosc. Radiat. Transf. **48**, 469 (1992).
35. J. H. Scryber, S. Miller, and J. Tennyson, J. Quant. Spectrosc. Radiat. Transf. **53**, 373 (1995).
36. S. Miller, J. Tennison, H. R. A. Jones, and A. J. Longmore, in *IAU Colloquium 146,* Ed. by U. G. Jørgensen (Springer-Verlag, Berlin, 1994), p. 296.
37. O. J. Polyansky, P. Jensen, and J. Tennyson, J. Chem. Phys. **101**, 7651 (1994).
38. H. R. A. Jones, S. Viti, J. Tennyson, *et al.*, Astron. Soc. Pac. Conf. Ser. **109**, 717 (1996).
39. H. Partrige and D. Schwenke, J. Chem. Phys. **106**, 4618 (1997).
40. R. Kurucz, http://cfaku5.harvard.edu/molecules/H_2O/ (1999).
41. Ya. V. Pavlenko, Astron. Zh. **77**, 254 (2000) [Astron. Rep. **44**, 219 (2000)].
42. Ya. V. Pavlenko and A. V. Shavrina, Kinematika Fiz. Nebesnykh Tel **2** (6), 54 (1986).
43. F. Allard and P. H. Hauschildt, Astrophys. J. **445**, 433 (1995).
44. E. Anders and N. Grevesse, Geochim. Cosmochim. Acta **53**, 197 (1989).
45. T. Tsuji, *Very Low Mass Stars and Brown Dwarfs,* Ed. by R. Rebolo and M. R. Zapatero Osorio (Cambridge Univ. Press, Cambridge, 2000), p. 126.
46. Ya. V. Pavlenko, Astron. Zh. **75**, 888 (1998) [Astron. Rep. **42**, 787 (1998)].
47. R. L. Kurucz, *ATLAS: A Computer Program for Calculating Model Stellar Atmospheres* (Smithsonian Astrophysical Observatory, Cambridge, 1970), Smithsonian Astrophys. Obs. Spec. Rept. No. 309.
48. R. L. Kurucz, CD ROM #9 (Smithsonian Astrophysical Observatory, Cambridge, 1993).
49. T. Tsuji, Astron. Astrophys. **23**, 411 (1973)
50. http://george.arc.nasa.gov/∼dschwenke (1999)
51. L. V. Gurvits, I. V. Veĭts, V. A. Medvedev, *et al., Thermodynamic Properties of Individual Substances* [in Russian] (Nauka, Moscow, 1979).
52. A. Borysow and L. Frommhold, Astrophys. J. **341**, 549 (1989).
53. A. Borysow and L. Frommhold, Astrophys. J. **348**, L41 (1990).
54. Ch. Zheng and A. Borysow, Astrophys. J. **441**, 960 (1995).
55. A. Borysow, U. G. Jørgensen, and Ch. Zheng, Astron. Astrophys. **324**, 185 (1997).
56. N. E. Piskunov, F. Kupka, T. A. Ryabchikova, *et al.*, Astron. Astrophys., Suppl. Ser. **112**, 525 (1995).
57. Ya. Pavlenko, Astrophys. Space Sci. **253**, 43 (1997).
58. H. R. A. Jones, A. J. Longmore, R. F. Jameson, and C. M. Mountain, Mon. Not. R. Astron. Soc. **267**, 413 (1994).
59. S. E. Nersisyan, A. V. Shavrina, and A. A. Yaremchuk, Astrofizika **30**, 249 (1989).
60. *IAU Symposium 198: The Light Elements and Their Evolution,* Ed. by L. da Silva, M. Spite, and J. R. De Medeiros, 590 (2000).
61. T. Tsuji, Astrophys. J. **538**, 801 (2000).
62. Ya. V. Pavlenko, Astron. Zh. **76**, 847 (1999) [Astron. Rep. **43**, 748 (1999)].

Translated by N. Samus'

Astronomy Reports, Vol. 46, No. 7, 2002, pp. 579–590. Translated from Astronomicheskiĭ Zhurnal, Vol. 79, No. 7, 2002, pp. 640–652.

The Outer Scale of Solar-Wind Turbulence from GALILEO Coronal-Sounding Data

A. I. Efimov [1], I. V. Chashei [2], L. N. Samoznaev [1], V. E. Andreev [1], M. K. Bird [3], P. Edenhofer [4], D. Plettemeier [4], and R. Wohlmuth [4]

[1] *Institute of Radio Engineering and Electronics, Russian Academy of Sciences, Mokhovaya ul. 11, Moscow, 101999 Russia*

[2] *Lebedev Physical Institute, Russian Academy of Sciences, Leninskiĭ pr. 53, Moscow, 117924 Russia*

[3] *Radio Astronomy Institute, Bonn University, Bonn, Germany*

[4] *Institute for High-Frequency Engineering, Bochum University, Bochum, Germany*

Received November 10, 2001; in final form, February 1, 2002

Abstract—Radio sounding experiments on of the solar plasma were carried out by the GALILEO spacecraft using S-band (2295 MHz) signals in 1995–1996 a period of minimum solar activity. Equatorial regions at heliocentric distances of 7–80 solar radii were studied. The frequency of the received signal was detected by three ground stations. By carrying out continuous observations of unprecedented duration and processing the data using spectral and correlation methods, we have obtained reliable information on large-scale inhomogeneities of the solar-wind density for the first time. The outer turbulence scale increases with heliocentric distance, the dependence being close to linear. We estimate the outer turbulence scale and analyze its dependence on distance from the Sun and local plasma parameters for a model in which the outer scale is formed due to competition between the linear amplification of Alfven waves in the irregular, moving solar-wind plasma and the nonlinear transfer of turbulent energy to higher frequencies. A comparison of predictions for various specific cases of this model with the observational data suggests that the main nonlinear processes responsible for the formation of the inertial range of the spectrum on the investigated scales are three-wave decay processes involving Alfven and magnetoacoustic waves.

1. INTRODUCTION

Studies of frequency fluctuations of radio signals used to sound the near-Sun plasma have been conducted using a number of spacecraft whose trajectories have taken them behind the Sun from the point of view of a terrestrial observer [1–5]. Analyses of such data have yielded much information on the characteristics of the solar wind in regions that cannot be investigated using direct methods. The most recent radio-sounding observations were carried out using the GALILEO satellite, which has been operating for a number of years in orbit around Jupiter [6, 7]. A high-stability, on-board oscillator transmitted a carrier signal in the S band, at a frequency $f =$ 2295 MHz. This signal was received and its frequency measured at the three tracking stations of the NASA Deep Space Network in Goldstone (USA), Tidbinbilla (Australia), and Madrid (Spain). An important feature of the experiments was that the ground stations were able to conduct continuous observations of the GALILEO satellite signal and, thus, to continuously detect frequency fluctuations for up to several tens of hours. Here, we analyze data on frequency fluctuations of the GALILEO signal detected from December 1995 to January 1996, when solar activity was low. Our aim is an experimental and theoretical investigation of large-scale inhomogeneities of the solar wind in the spectral interval near the outer turbulence scale.

2. THEORY OF FREQUENCY FLUCTUATIONS FOR RADIO SIGNALS PROPAGATING THROUGH THE NEAR-SUN PLASMA

In accordance with [8], we assume that the spatial spectrum of inhomogeneities of the electron density can be written in the form

$$\Phi_N(q,r) = C_N^2(r)\frac{\exp\left(-\frac{q^2}{q_m^2}\right)}{(q_0^2+q^2)^{p/2}}, \qquad (1)$$

where r is heliocentric distance, q the spatial wavenumber, q_m the wavenumber corresponding to the inner turbulence scale $\ell_m = 2\pi/q_m$, q_0 the wavenumber corresponding to the outer turbulence scale $L_0 =$

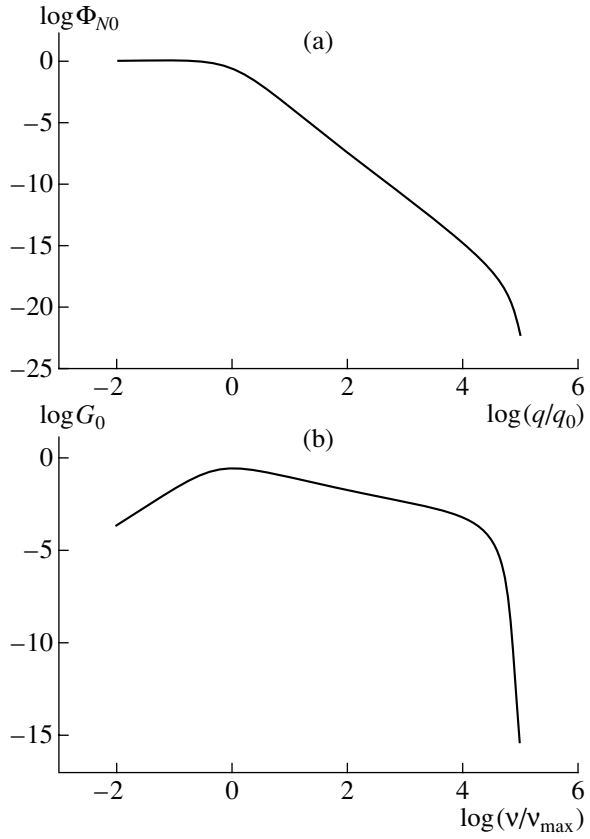

Fig. 1. (a) Normalized spatial spectrum of the electron density inhomogeneities and (b) temporal energy spectrum of the frequency fluctuations.

$2\pi/q_0$, p the spectral index of the spatial turbulence spectrum and $C_N^2(r)$ a factor characterizing the intensity of electron-density fluctuations. The maximum value of Φ_N occurs when $q = 0$: $\Phi_{N\max} = C_N^2/q_0^p$. The spatial spectrum of electron-density inhomogeneities normalized to its maximum value takes the form

$$\Phi_{N0}(q) = \frac{\exp\left(-\frac{q^2}{q_0^2}A^2\right)}{\left(1+\frac{q^2}{q_0^2}\right)^{p/2}}, \qquad (2)$$

where $A = \frac{q_0}{q_m} = \frac{\ell_m}{L_0}$ is a quantity varying from 10^{-5} (at small distances from the Sun, where $\ell_m = 10$ km, $L_0 = 10^6$ km) to 3×10^{-4} (at large distances, where $\ell_m = 100$ km, $L_0 = 3\times10^6$ km) [3]. A normalized spatial spectrum on a double logarithmic scale is drawn in Fig. 1a for the case $p = 11/3$ (Kolmogorov–Obukhov turbulence) and $A = 10^{-5}$. This spectrum is characterized by a sharp decrease in the spectral density with increasing q at $q \geq q_m$ and a flattening at $q \leq q_0$. In the inertial interval $q_0 < q < q_m$, the spectral density decreases according to a power law, as q^{-p}.

If the turbulence is frozen into the outward-convected solar wind, then the energy spectrum of the frequency fluctuations can be written [8] as

$$G(\nu) = F\left(v_c^{-\alpha}\cdot\pi\right)^{-1} L_0^{-\alpha}\nu^2 \times \exp\left(-\frac{\nu^2\ell_m^2}{v_c^2}\right)\left(L_0^{-2}+\frac{\nu^2}{v_c^2}\right)^{-\frac{2+\alpha}{2}}, \qquad (3)$$

where $\alpha = p-3$, $F = (p-3)r_e^2\lambda^2\sigma_N^2 L_e$, $r_e = 2.82\times10^{-13}$ cm is the classical electron radius, L_e is the effective thickness of the scattering screen, v_c is the convective velocity of inhomogeneities crossing the signal ray path, λ is the radio wavelength, and σ_N^2 is the variance of the electron-density fluctuations. Differentiating (3) with respect to ν and using the inequality $L_0 \gg \ell_m$, we find that the spectral density $G(\nu)$ possesses a maximum at the fluctuation frequency

$$\nu_{\max} = \frac{v_c\sqrt{2/\alpha}}{L_0}. \qquad (4)$$

It follows from (4) that $\nu_{\max}$ can be used to determine the outer turbulence scale if the convective velocity v_c and the spectral index of the fluctuations α are known. The value of v_c can be derived from the position of the maximum of the cross-correlation function of the frequency fluctuations detected simultaneously by two spaced stations. It is also possible to derive this information using data on the propagation of a radio signal from the Earth to the spacecraft and back, when the satellite transponder is driven by the uplink (i.e., coherent operation mode) [5, 9, 10]. The spectral index α is equal to the slope of the energy spectrum $G(\nu)$ in the inertial interval.

The energy spectrum normalized to its maximum value can be derived from (3) and (4):

$$G_0(\nu) = \frac{\nu^2}{\nu_{\max}^2}\left[\frac{1+\frac{\nu^2}{\nu_{\max}^2}\cdot\frac{2}{p-3}}{(p-1)(p-3)}\right]^{\frac{1-p}{2}} \times \exp\left[\frac{2}{p-3}A^2\left(1-\frac{\nu^2}{\nu_{\max}^2}\right)\right]. \qquad (5)$$

The temporal energy spectrum as a function of $\nu/\nu_{\max}$ for the same values $A = 10^{-5}, p = 11/3$ is shown on a double logarithmic scale in Fig. 1b. This spectrum possesses a maximum at $\nu = \nu_{\max}$, and the spectral density decreases with increasing ν as a power law with index $\alpha = p-3$ in the inertial interval. The spectral density rapidly tends to zero at $\nu > \frac{v_c}{\ell_m}$ due to the influence of the inner turbulence scale.

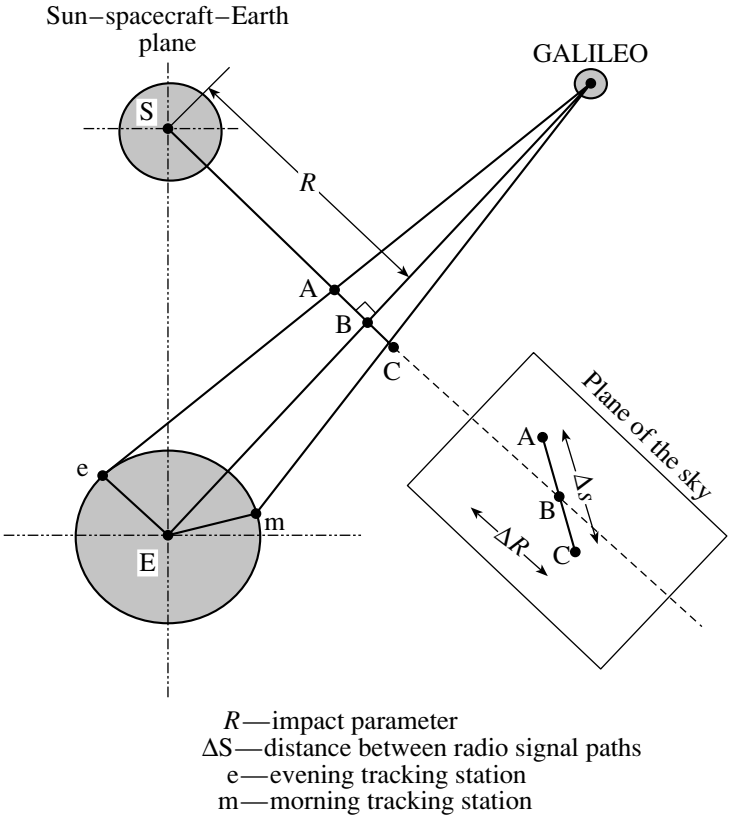

Fig. 2. Geometrical configuration of a solar-plasma radio-sounding experiment using GALILEO spacecraft.

3. FREQUENCY FLUCTUATION DATA FROM RADIO SOUNDING OF THE NEAR-SUN PLASMA

Figure 2 depicts the geometrical configuration of the experiment. In the Sun–satellite–Earth plane, S is the center of the Sun; E the center of the Earth; R the impact parameter of the radio signal, which we will express in solar radii R_s; e and m are two ground tracking stations; Δs the distance between the signal paths in the plane perpendicular to the line of sight to the spacecraft (the plane of the sky) in the region of maximum scattering of the radio signals; $\Delta s \approx \frac{\Delta r \cdot L_1}{L_1+L_2}$ (where L_1 is the distance from the spacecraft to the Sun, L_2 the distance from the Sun to the ground stations, and Δr the distance between the stations on the Earth's surface); and ΔR is the projection of Δs onto the direction of motion of the solar wind, which is approximately radial.

A series of radio sounding experiments of the near-Sun plasma was carried out during the solar occultation of the GALILEO spacecraft from December 2, 1995, to December 17, 1995 (ingress) and from December 21, 1995, to January 14, 1996 (egress). The impact parameter R varied in this period from 7 to 78.4 R_s. The three ground stations involved in the experiment recorded the frequency of the received signal once per second; the signal was transmitted by GALILEO in an automated mode. There were 51 sessions when the signal frequency could be detected simultaneously by two ground stations. The preliminary data reduction yielded prolonged uninterrupted sets of frequency measurements made up of tens or even hundreds of thousands of one-second values. We describe the reduction procedure using as an example three sessions conducted successively by the three stations on December 12–13, 1995, when the average impact parameter was $17.1R_s$.

The first session was carried out by the Madrid station from $08^h44^m08^s$ UT to $16^h27^m06^s$, the second by the Goldstone station from $15^h59^m54^s$ to $23^h47^m13^s$ UT, and the third by the Tidbinbilla station from $23^h06^m14^s$ to $08^h30^m53^s$ UT (December 13). The signals were detected simultaneously by two stations in the intervals from $15^h59^m34^s$ to $16^h27^m06^s$ UT and from $23^h06^m14^s$ to $23^h47^m13^s$ UT. We approximated the slowly varying behavior of the frequency (linear trend) separately for each of the three sessions using a least-squares method and subtracted it from the initial data. The residual frequency fluctuations for the three successive sessions are shown in Fig. 3. Intervals in which the observations overlap are marked by the pairs of vertical lines *1* and

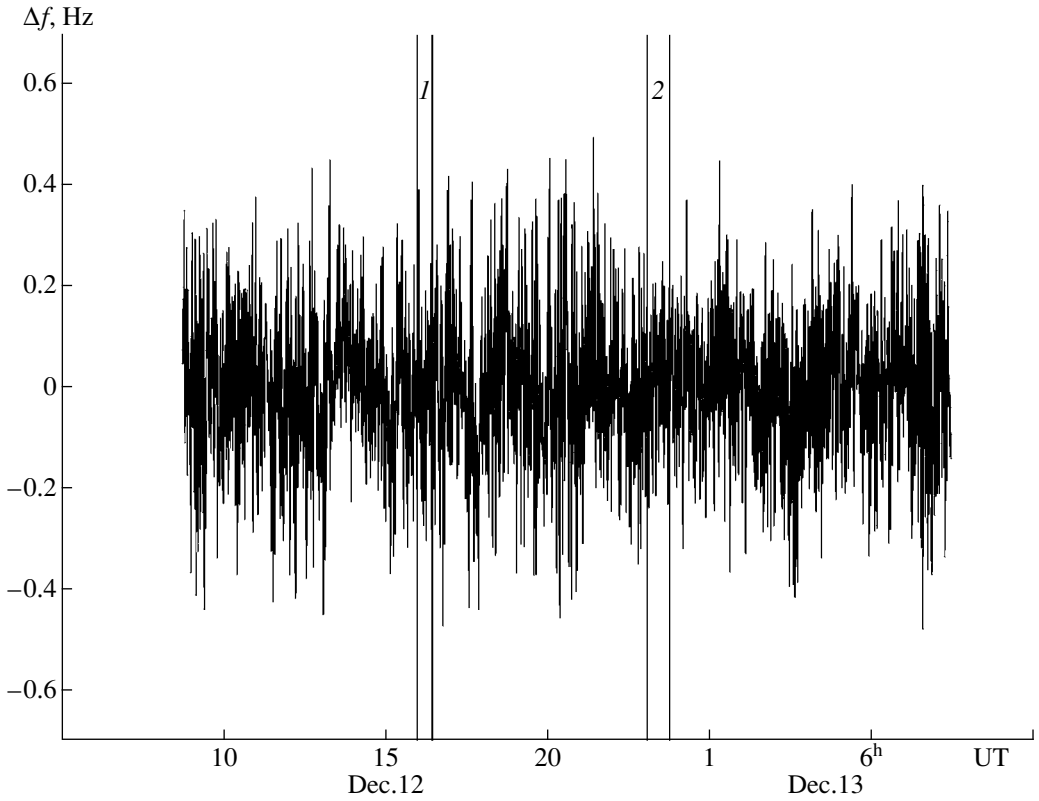

Fig. 3. Frequency fluctuations detected by the three stations on December 12–13, 1995.

2. The data sets in these sections correspond to the earlier session. The total time of continuous frequency measurements was about one day ($23^{\rm h}46^{\rm m}45^{\rm s}$ or 85 506 readings). The subsequent reduction of the frequency data sets included calculation of the temporal energy spectra and cross-correlation functions of the frequency fluctuations measured simultaneously by two stations. We obtained the temporal spectra using a Fast Fourier Transform (FFT) with the number of readings being $2^{15} = 32\,768$ and $2^{16} = 65\,536$. Figure 4 shows the three FFT-32 768 spectra for the frequency recording presented in Fig. 3 on a double logarithmic scale. The first, second, and third spectra were derived from the first, second, and third sets of 32 768 readings. The frequency interval covered by the spectrum is constrained on the left by the duration of the time interval in which the spectrum was determined and on the right by the Nyquist frequency, which is equal to 0.5 Hz in this case. In general, the experimental spectra are similar to the theoretical spectra. One important feature is the presence of a maximum at $\nu = \nu_{\max} \approx 1.2 \times 10^{-4}$ Hz, which confirms the existence of an outer turbulence scale for the near-Sun plasma. The spectral density decreases with increasing ν approximately as a power law, $\nu^{-\alpha}$, above the maximum. The value of α averaged over all three spectra is 0.728. The effect of the inner scale is not visible in the observational spectra, since the expected frequency of the "knee" $\nu \approx v_c/\ell_m$ is substantially higher than the Nyquist frequency, 0.5 Hz.

Another spectrum, derived from the first 65 536 frequency-fluctuation readings, is presented in Fig. 5. For comparison, a theoretical spectrum calculated using (5) with $\nu_{\max} = 10^{-4}$, $\alpha = 0.8$, and the maximum spectral density $G_{\max} = 5\ \mathrm{Hz}^2/\mathrm{Hz}$ is also plotted. A comparison of all the curves in Figs. 4 and 5 shows that the spectral maximum is stable, and the value of $\nu_{\max}$ does not depend on the duration of the series. This is confirmed by spectral analysis of many other sessions carried out for various heliocentric distances.

We calculated the cross-correlation function of the frequency fluctuations detected simultaneously by two stations using the well-known formula [11, 12]

$$K(\tau) = \frac{\langle \Delta f_1(t) \cdot \Delta f_2(t+\tau) \rangle}{\sigma_1 \sigma_2}, \qquad (6)$$

where τ is the temporal shift, Δf_1 and Δf_2 are the frequency fluctuations detected in the first joint session by the Madrid (Δf_1) and Goldstone (Δf_2) stations and in the second joint session by the Goldstone (Δf_1) and Tidbinbilla (Δf_2) stations, and σ_1 and

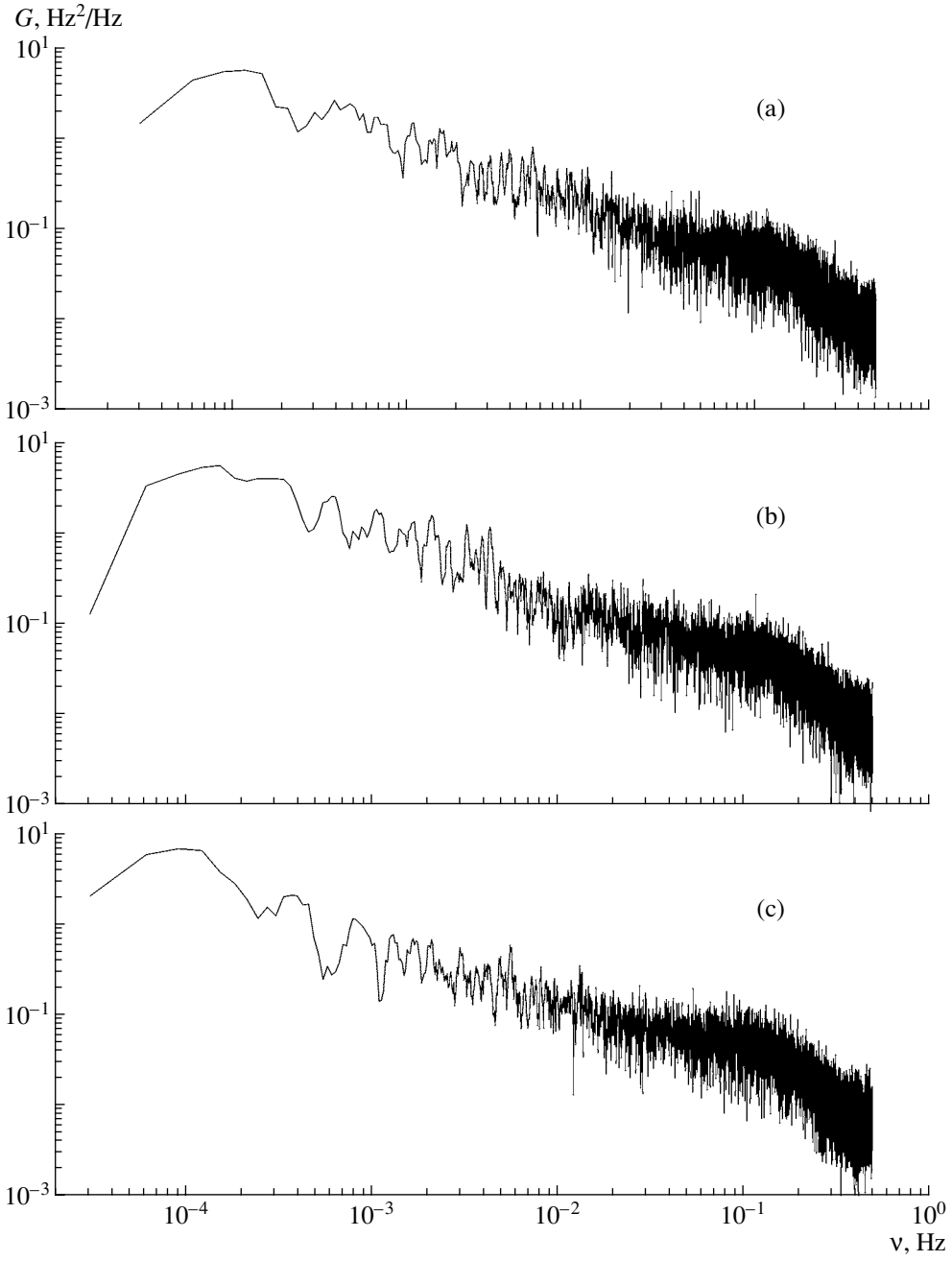

Fig. 4. Temporal spectra of the frequency fluctuations for the session of December 12–13, 1995.

σ_2 are the rms frequency fluctuations for the corresponding stations. The averaging time for the product $\Delta f_1(t) \cdot \Delta f_2(t+\tau)$ was specified by the duration of the intervals of simultaneous observations and was 1600 s for the first session and 2400 s for the second session. To determine the time of the maximum of the cross-correlation function $\tau_{\max}$ more accurately, the data sets Δf_1 and Δf_2 were averaged over a time Δt, which varied from 1 to 13 s. The maximum value $K(\tau)$ increases rapidly with increasing Δt up to the time $\Delta t = 13$ s, which is the value we used in our calculations.

Figures 6a, 6b present the cross-correlation functions derived from simultaneous frequency measurements in the two time intervals 1 and 2 in Fig. 3. In the first interval, when the measurements were carried out by the Madrid and Goldstone stations, $\tau_{\max} = -26$ s and $K_{\max} = 0.70$. For the second combination of ground stations (Goldstone and Tidbinbilla), these values were -24 s and 0.61. The minus indicates that the GALILEO–Madrid radio-signal path was further

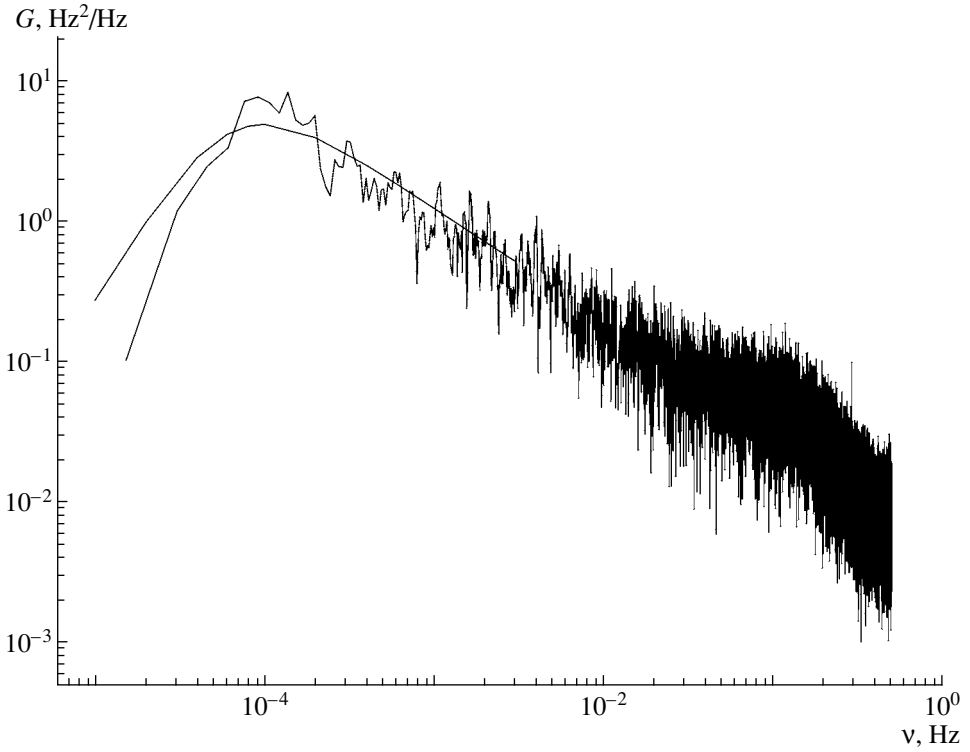

Fig. 5. Temporal spectrum of the frequency fluctuations for a set of 65 536 readings.

from the Sun than the GALILEO–Goldstone path. In the second interval, the GALILEO–Tidbinbilla radio-signal path was closer to the Sun. The function $K(\tau)$ derived from the Madrid and Goldstone measurements is narrower, and its maximum is more pronounced. This observed effect is due to the differences in the distance between the paths Δs and the angles ψ between the baseline direction and the velocity of motion of the plasma inhomogeneities. (The angles ψ were 10° and 50°, respectively.) For the first interval, $\Delta s = 7020$ km, while this quantity was substantially larger for the second interval—$\Delta s = 8490$ km.

The quantity $\tau_{\max}$ is related to the convective velocity of motion of inhomogeneities through the radio-signal path [10–12]:

$$\tau_{\max} = \frac{\Delta R}{v_c} = \frac{\Delta R}{v \pm v_R}, \qquad (7)$$

where v is the solar-wind velocity and v_R is the rate of change of the impact parameter, which was 24 km/s in our experiments (a plus sign refers to motion of the spacecraft behind the Sun, and a minus sign to motion out from behind the Sun). The quantity ΔR was 6900 km and 5430 km for the first and second intervals, respectively. Using the experimental values of $\tau_{\max}$, v_R, and ΔR, we obtained the convective velocity $v_c = 245$ km/s and solar-wind velocity 221 km/s averaged over the two sessions. Further, using the values for $\nu_{\max}$ and α presented above, we find the outer turbulence scale to be $L_0 = 5.56\ R_s$.

4. RADIAL DEPENDENCE OF THE SOLAR-WIND CHARACTERISTICS

The behavior of the outer turbulence scale L_0, spectral index α, and solar-wind velocity v for various distances of the radio-signal paths from the Sun derived from GALILEO data for 1995–1996 are presented in Fig. 7. The outer turbulence scale, whose values vary from 1 to $15R_s$, is given in the top panel (Fig. 7a). This scale increases with increasing R. This figure also contains a least-squares line fitted to the experimental points. The equation of this line is $L_0(R) = a\,(R/R_s)^m$, where $a = 0.242R_s$ and $m = 0.796$. The index α of the energy spectrum of the frequency fluctuations is presented in the middle panel (Fig. 7b). The values of α cluster near 0.67, which corresponds to Kolmogorov–Obukhov turbulence. Finally, the solar-wind velocity is shown in the bottom panel (Fig. 7c). The leftmost three values, for the smallest heliocentric distances, were obtained previously by radio-sounding measurements made using signals emitted by the VENERA-15 and VENERA-16 spacecraft. We plot them here because they were also used to find the outer turbulence scale. We could not find the velocity v at such small distances R using the GALILEO data, since there

was no correlation between the frequency fluctuations detected at two stations. The velocity of the solar wind increases with R, from 100 to 300–400 km/s [13]. The GALILEO data confirm this conclusion for the more restricted interval $R > 15R_s$. The importance of information about the solar-wind velocity is associated with the fact that energy spectra of the frequency fluctuations were obtained simultaneously at very low frequencies ($\nu < 10^{-4}$ Hz). The combined data on the velocity and spectra enabled us to determine the radial dependence of the outer turbulence scale of the near-Sun plasma.

5. MECHANISM FOR THE FORMATION OF THE OUTER TURBULENCE SCALE

Let us consider a possible physical mechanism for the formation of the outer turbulence scale in inner regions of the solar wind. We assume that most of the energy of solar-wind perturbations is concentrated in Alfven waves, which are initially excited at the base of the corona and then propagate from the Sun. When considering the energy spectrum of the Alfven waves and its radial evolution, we must take into account linear effects associated with motion and the smooth nonuniformity of the background solar wind, as well as nonlinear effects associated with local interactions between the waves, which lead to the excitation of magnetoacoustic waves and, accordingly, density fluctuations [17–20]. The propagation of Alfven waves in a quasi-stationary medium can be described by the equation [19, 20]

$$\mathrm{div}\left(\frac{3\mathbf{v}}{2}+\mathbf{v}_A\right)W_k - \mathbf{v}\mathrm{grad}\left(\frac{W_k}{2}\right) = -\frac{\partial}{\partial k}F_k, \quad (8)$$

where k is the wavenumber, W_k is the one-dimensional energy spectrum (spectral density) of the Alfven waves, F_k is the cascade energy function, and $\mathbf{v}$ and $\mathbf{v}_A$ are the solar-wind velocity and Alfven velocity, which is directed along the regular magnetic field. Linear effects dominate for sufficiently low wave frequencies. In this case, the right-hand side of (8) is negligible compared to the left-hand side, which is of the order of W_k/t_l, where $t_\mathrm{l} = \frac{r}{v+v_A}$ is the characteristic time for propagation through a distance of the order of the heliocentric distance r. On the other hand, nonlinear effects, described by the right-hand side of (8), dominate at high frequencies. In this case, the left-hand side is negligible compared to the right-hand side, which is of the order of W_k/t_nl, where t_nl is the characteristic time for nonlinear interactions, which depends on the particular form of the cascade function F_k (which is different in different turbulence models).

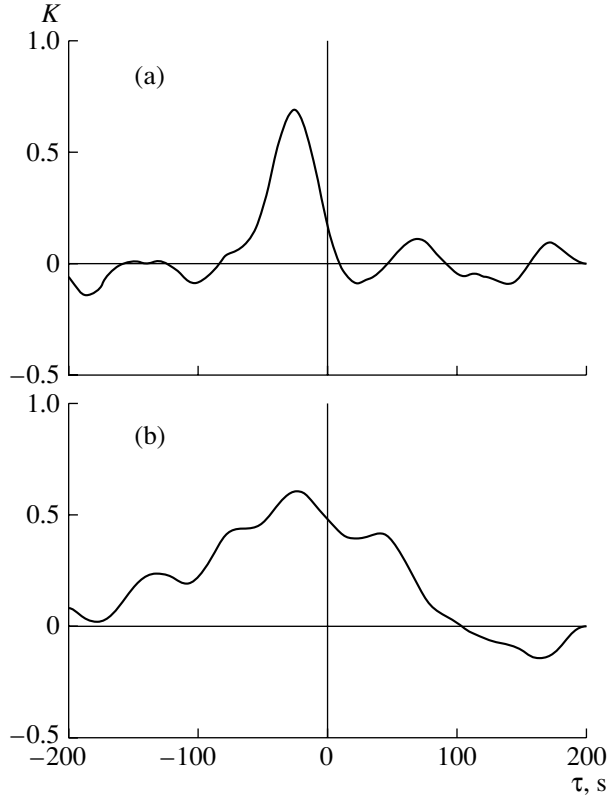

Fig. 6. Cross-correlation functions of the frequency fluctuations detected by two distinct stations: (a) Madrid–Goldstone and (b) Goldstone–Tidbinbilla.

The wavenumber k_0 for which the rates of the linear and nonlinear processes are approximately equal will represent physically the main scale for Alfven turbulence (and the corresponding spatial fluctuations of the magnetic field), since the turbulent energy is transferred by cascade processes from regions with scales of the order of k_0 to spectral regions with smaller scales. Fluctuations whose scales are below k_0^{-1} are generated locally, while those with scales exceeding k_0^{-1} are a source of turbulent energy and are associated with waves in a regime of direct linear propagation. We can determine the outer scale k_0^{-1} from the relation

$$t_\mathrm{l}(k_0) = t_\mathrm{nl}(k_0) \quad (9)$$

for the cascade functions F_k corresponding to various possible models for the turbulence, we consider the dependences of k_0 on distance from the Sun (i.e., radial dependence) and on local parameters, in particular, the solar-wind velocity (i.e., parametric dependences).

Let us specify the one-dimensional spatial spectrum of low-frequency Alfven waves in the form of a power function:

$$W_k = Ck^{-\gamma}, \quad (10)$$

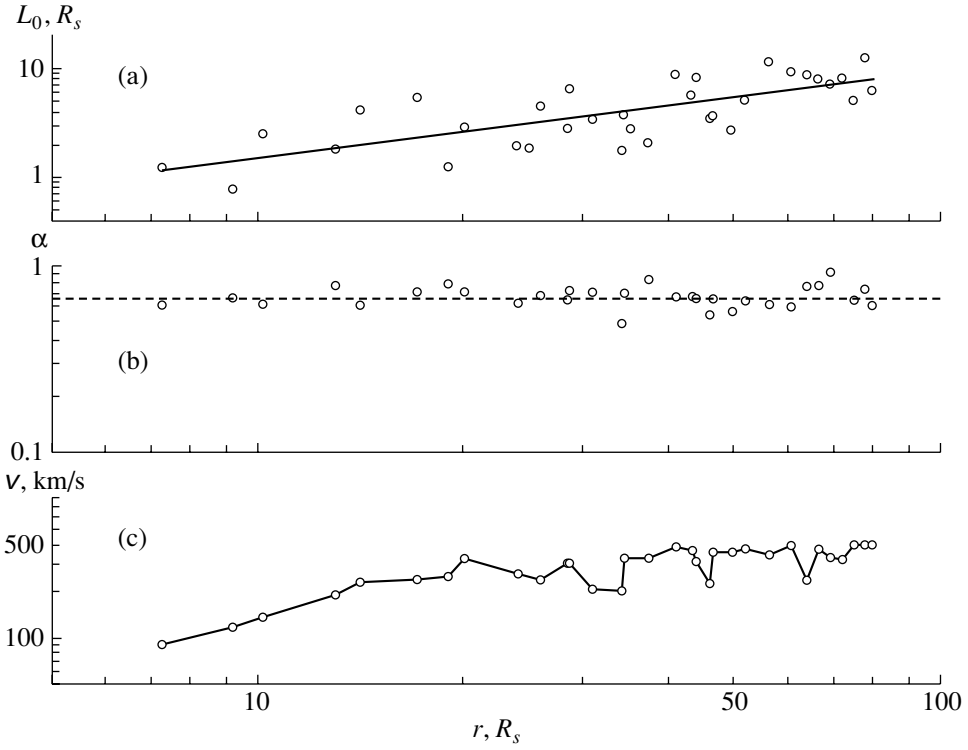

Fig. 7. Radial dependences of the (a) outer turbulence scale, (b) spectral index of the frequency fluctuations, and (c) solar-wind velocity.

where $C = C(r)$ is a structure constant whose radial dependence can be found if nonlinear effects are neglected. Assuming the magnetic field is strong and $\beta = (v_S/v_A)^2 \ll 1$ (where v_S is the sound speed), we adopt the following model representation for the cascade function F_k:

$$F_k = \epsilon v_A k^2 W_k \left(\frac{kW_k}{B^2}\right)^n, \qquad (11)$$

where $\epsilon \approx 0.1 = \text{const}$, B is the local magnetic induction, and the exponent $n = n_{1,\,2,\,3}$ is different for different mechanisms for the formation of the turbulent spectra at $k > k_0$. Namely, $n = n_1 = 1/2$ for strong turbulence [19, 20], $n = n_2 = 1$ for weak turbulence in which three-wave decay processes are the main type of interaction [17], and $n = n_3 = 2$ for weak turbulence dominated by four-wave processes [21]. The corresponding scaling turbulence spectra W_k at $k > k_0$ are determined by the condition $F_k = \text{const}$, and have the power-law form

$$W_k = Ck_0^{\alpha-\gamma} * k^{-\alpha}, \qquad (12)$$

where the indices α are $\alpha_1 = 5/3$ (a Kolmogorov spectrum), $\alpha_2 = 3/2$ (a Kraichnan spectrum), and $\alpha_3 = 4/3$, respectively. We adopt below the natural assumption that $\alpha > \gamma$.

Substituting (10) and (11) into (9), we obtain the relation for k_0

$$k_0^{1+n(1-\gamma)} = \left(\frac{B^2}{C}\right)^n \frac{v + v_A}{\epsilon r v_A}, \qquad (13)$$

which describes the dependence of the outer turbulence scale on heliocentric distance and the local plasma parameters. In regions sufficiently close to the Sun, where the flow is sub-Alfvenic ($v \ll v_A$), the structure constant $C \sim \rho^{1/2}$ (where ρ is the plasma density) [22], and the dependence (13) takes the form

$$k_0^{1+n(1-\gamma)} = \left(\frac{B^2}{\rho^{1/2}}\right)^n \frac{1}{r}. \qquad (14)$$

In the case of practical importance of a steady super-Alfvenic flow with $v \gg v_A$ (where $v = \text{const}$) and an approximately radial magnetic field, we can take $B \sim r^{-2}$ and $v_A \sim r^{-1}$. Then, $C \sim r^{-3}$ [22], and the radial dependence of the outer scale will be specified by the first coefficient on the right-hand side of (13):

$$k_0^{1+n(1-\gamma)} \sim r^{-n}. \qquad (15)$$

We can easily see that the dependences (14) and (15) for k_0 are decreasing functions of r. As a result, the outer turbulence scale k_0^{-1} should increase with distance from the Sun. Let us write the radial dependences k_0^{-1} (15) for specific values of the exponent n

adopted in (11):

$$k_0^{-1} \sim r^m, \tag{16}$$
$$m_1 = \frac{1}{3-\gamma} \quad \text{for} \quad n = \frac{1}{2},$$
$$m_2 = \frac{1}{2-\gamma} \quad \text{for} \quad n = 1,$$
$$m_3 = \frac{1}{3-2\gamma} \quad \text{for} \quad n = 2.$$

Let us consider the dependence of the outer turbulence scale on the local parameters of the solar-wind plasma in more detail. This parametric dependence is due to both the explicit presence of v, v_A, and B in (13) and the dependence of the structure constant C on the plasma parameters. Following the model for the formation of the solar wind developed in [23–25], we assume that the solar wind is accelerated primarily by the nonlinear dissipation of Alfven waves with the spectrum (10) passing through the inner corona. The continuity equation is

$$\rho_* v_* S_* = \rho v S, \tag{17}$$

where ρ is the plasma density, S the cross section of the flux tube, and the asterisks denote quantities at the coronal base ($v_{A^*} \gg v_*$)). Taking this equation into account, we can write the approximate relation

$$\rho_* \frac{v_* v^2}{2} \approx \int_{k_{0*}}^{k_{m^*}} C_* v_{A^*} k_*^{-\gamma} dk_* \tag{18}$$
$$\approx C_* v_{A^*} (k_{m^*})^{1-\gamma},$$

where k_{m^*} is the maximum wavenumber of Alfven waves with the spectrum (10) passing through the base of the corona, and k_{0^*} is the characteristic wavenumber k_0 at the coronal base ($k_{m^*} \gg k_{0^*}$).

For low-frequency Alfven waves propagating in a quasi-stationary, nonuniform, moving medium, we can use the conservation of the wave flux in differential form [22]

$$C_* v_{A^*} S_* k_*^{-\gamma} dk_* = C(v + v_A)^2 v_A^{-1} S k^{-\gamma} dk, \tag{19}$$

where we have used the inequality $v_* \ll v_{A^*}$ and the condition for frequency conservation

$$k_* v_{A^*} = k(v + v_A), \tag{20}$$

which specifies the relation between k and k_*. Combining (18)–(20), we obtain the formula for the local value of the structure constant:

$$C = \left(\frac{\rho v v_A}{2}\right) \left(\frac{v}{\Omega_{m^*}}\right)^{1-\gamma} \left(\frac{v}{v + v_A}\right)^{1+\gamma}, \tag{21}$$

which has no explicit dependence on the cross section of the flux tube S and, in the region of steady flow with $v \gg v_A$, simplifies to

$$C = \left(\frac{\rho v v_A}{2}\right) \left(\frac{v}{\Omega_{m^*}}\right)^{1-\gamma}. \tag{22}$$

In (21) and (22), $\Omega_{m^*} = k_{m^*} v_{A^*}$ is the frequency of Alfven waves emerging from the corona and corresponding to the maximum wavenumber k_{m^*}. According to the estimates of [23, 24], $\Omega_{m^*} = 2 * 10^{-2}$ s^{-1}, which corresponds to Alfven waves with periods of about 5 min.

Substituting (22) into (13), we can easily show that the characteristic turbulence scale k_0 possesses a parametric dependence only on the local solar-wind velocity v and Alfven velocity v_A. In the particular case of $\gamma = 1$ (a flicker spectrum), k_0 depends only on the Alfven Mach number $\mathrm{M}_A = v/v_A$. The dependence $k_0(v, v_A)$ for the steady solar wind with $\mathrm{M}_A \gg 1$ is

$$k_0^{1+n(1-\gamma)} \sim v^{1-n(2-\gamma)} v_A^{n-1}. \tag{23}$$

Further, we use the well-known property of the approximate conservation of the mass-flux density in the steady solar wind ($\rho v \approx$ const) [26]. Assuming that variations of the magnetic-field induction are small, we obtain the relation $v_A \sim v^{1/2}$. In this case, we can derive the following dependence of the characteristic scale k_0 on the solar-wind velocity v from (23):

$$k_0^{1+n(1-\gamma)} \sim v^{\frac{1+n(2\gamma-3)}{2}}. \tag{24}$$

For the specific values $n = 1/2$, 1, and 2, which correspond to different types of nonlinear interactions, we find from (24) that

$$k_0^{-1} \sim v^{\mu}, \tag{25}$$
$$\mu_1 = \frac{1-2\gamma}{2(3-\gamma)} \quad \text{for} \quad n = \frac{1}{2},$$
$$\mu_2 = \frac{1-\gamma}{2-\gamma} \quad \text{for} \quad n = 1,$$
$$\mu_3 = \frac{5-4\gamma}{2(3-2\gamma)} \quad \text{for} \quad n = 2.$$

It is interesting that, when $\gamma = 1$, the character of the parametric dependence of the outer turbulence scale (25) turns out to be different for different types of nonlinear interactions: a decreasing dependence $k_0^{-1}(v)$ for Kolmogorov turbulence ($\mu_1 = -1/4$), the absence of any dependence $k_0^{-1}(v) = \text{const}$ for Kraichnan turbulence ($\mu_2 = 0$), and an increasing dependence $k_0^{-1}(v)$ for turbulence dominated by four-wave processes ($\mu_3 = 1/2$).

Strictly speaking, the outer turbulence scale k_0^{-1} specified by (13) refers to the spatial energy spectrum

of magnetic-field fluctuations associated with Alfven waves. Since decay processes are prohibited inside the Alfven regime by the conservation laws, magnetoacoustic waves associated with density fluctuations are excited by the nonlinear interactions of the Alfven waves forming the quasi-stationary turbulence spectrum. The energy spectra of the Alfven and magnetoacoustic waves in the inertial wavelength interval are similar; this follows both from the solutions of the corresponding kinetic equations for the waves [18] and from numerical modeling of the generation of density fluctuations by Alfven turbulence [27, 28]. The outer turbulence scales for the spatial energy spectra of density fluctuations (corresponding to magnetoacoustic waves) and magnetic-field fluctuations (corresponding to Alfven waves) will also be similar. Indeed, the frequencies of interacting Alfven and slow magnetoacoustic waves are considerably different in individual decay processes in the low-pressure plasma, but the corresponding wavenumbers differ by no more than a factor of two. If the Alfven waves decay during interactions with fast magnetoacoustic waves with approximately the same phase velocity, the frequencies and wavenumbers of the two types of waves will, on average, both be close to each other. Accordingly, we shall use the above estimates of the outer turbulence scale (13) together with its radial (16) and parametric (25) dependencies to interpret the data on fluctuations of the received radio frequency due to fluctuations of the solar-wind plasma density.

6. COMPARISON OF THE MODEL WITH OBSERVATIONAL DATA

Let us compare the model estimates of the outer turbulence scale with the observational data on the shape of the energy spectra of the frequency fluctuations for the GALILEO sounding radio signals presented in Figs. 4 and 5. These data demonstrate that the outer turbulence scale increases monotonically with heliocentric distance, in qualitative agreement with the model. Apart from the three inner points, the data in Fig. 7c correspond to the region of steady flow, where the velocity is almost independent of distance from the Sun. Consequently, we can use the model dependences (16) for the parameter $L_0 = 2\pi/k_0$ presented in Fig. 7a. The observed dependence $L_0(r)$ in Fig. 7a is almost linear ($m_{\rm obs} \approx 0.8$). Substituting this value of m into (16), we find $\gamma = \gamma_1 \approx 7/4$ for Kolmogorov turbulence, $\gamma = \gamma_2 \approx 3/4$ for Kraichnan turbulence, and $\gamma = \gamma_3 \approx 1/4$ for turbulence associated with four-wave processes.

As is known from observations, the one-dimensional energy spectra of magnetic-field fluctuations at low frequencies are characterized by the exponent $\gamma_{\rm obs} \approx 1$ [29–31]. Comparing this value with the above estimates γ_{123}, we conclude that the model with $n = 1$ ($\gamma_2 \approx 3/4$), whose turbulence spectrum in the inertial interval is formed by three-wave decays, is in the best agreement with the low-frequency flicker spectrum. The small excess of the value $m_2 = 1$, corresponding to $n = 1$, over the measured value $m_{\rm obs} \approx 0.8$ could reflect the fact that the assumptions $v = {\rm const}$ and $v \gg v_A$ adopted when deriving the asymptotic dependence (16) are not completely satisfied in the inner part of the interval of heliocentric distances considered. The estimate $\gamma_1 \approx 7/4$ ($n = 1/2$) implies that there is essentially no characteristic scale in the turbulence energy spectrum, since $\gamma_1 \approx \alpha = 5/3$. The value $\gamma_3 \approx 1/4$ ($n = 2$) differs appreciably from the expected value of γ. On the other hand, the measured index $\alpha_{\rm obs} = 0.68 \pm 0.087$ for the inertial interval is closer to the Kolmogorov index $\alpha_1 = 5/3$. On average, these values are slightly higher than the value $\alpha = 1/2$, corresponding to $n = 1$. This disagreement may be due to the fact that taking into account the nonlinear dissipation of Alfven waves via interactions with magnetoacoustic waves increases α to values $\alpha \geq 1.6$ [18]. Including nonlinear dissipation in the initial equation (8) will not change our estimate (13) for the characteristic scale of the spectrum k_0.

Extrapolating the observed radial dependence of the outer turbulence scale to the heliocentric distance $r = 1$ AU leads to the value $L_0 \approx 20 R_S$. This is in a good agreement with the data of [32–34] on the characteristic scale for correlations between magnetic-field fluctuations, if we take into account the fact that the scale $L_0' \approx (1\text{–}2) \times 10^{11}$ cm determined in [32–34] corresponds to $L_0' \approx k_0^{-1} = \frac{L_0}{2\pi}$. Moreover, according to the results of [34], the outer turbulence scale increases with heliocentric distance, also in agreement with our conclusions. Note that there are no trustworthy data on the outer scale of density fluctuations, even near the Earth's orbit, to say nothing of the inner solar wind.

Let us now use the values for the outer turbulence scale L_0 to estimate the fractional level of Alfven turbulence, which coincides with the value $\frac{\rm C}{\rm B^2}$ when $\gamma \approx 1$. Inserting $\gamma \approx n \approx 1$ into (13), we find when $v \gg v_A$ that

$$\frac{\rm C}{\rm B^2} \approx \frac{L_0}{2\pi\epsilon r} * \frac{v}{v_A}. \qquad (26)$$

For definiteness, we will consider the heliocentric distance $r = 50 R_S$, where measurements show that we can assume that $L_0 \approx 5 R_S$ and $v \approx 400$ km/s. In addition, we take $v_A \approx 200$ km/s (for a constant solar-wind velocity and approximately radial magnetic field, this corresponds to the typical value $v_A \approx$

50 km/s at $r \approx 1$ AU) and $\epsilon \approx 0.15$ (this coefficient is known only to order of magnitude [20]). Then, formula (26) gives $C/B^2 \approx 0.3$ at $r = 50R_S$ and $C/B^2 \approx 0.3(r/50R_S)$ at $30R_S \leq r < 1$ AU. These estimates are in reasonable agreement with local measurements made by the HELIOS spacecraft [20] in this range of heliocentric distances and suggest a fairly high level of Alfven turbulence in the steady solar wind. On the other hand, the radial dependence of the fractional level of magnetic-field fluctuations at 0.41–0.65 AU is weaker than linear [34]. This is probably due to the fact that the magnetic-field fluctuations are in a saturation regime with $C/B^2 \approx$ const at heliocentric distances of about 0.4–0.5 AU.

7. CONCLUSIONS

The spectrum of turbulence in the solar plasma is characterized by the power of fluctuations of the electron density σ_N^2, the spectral index of the spatial spectrum of the turbulence p, and the inner ℓ_m and outer L_0 scales of the turbulence. The parameters σ_N, ℓ_m, and p have been studied in numerous radio-sounding experiments carried out during various levels of solar activity and at various heliocentric distances, heliolatitudes, and longitudes. Data on the outer turbulence scale were previously limited to the rough estimates of [3, 14]. We have derived here the radial dependence of the outer turbulence scale, which is described by a power law with its exponent m being close to unity.

It was established earlier that the inner turbulence scale ℓ_m increases with heliocentric distance, also according to a power law, $\ell_m \propto (r/R_s)^{1.4\pm0.4}$ at $r < 80R_s$ [13–15]. The dependence $\ell_m(r)$ may flatten at $r > 60R_s$, and, at larger distances ($r > 150R_s$), the inner scale reaches the value 200 km and becomes independent of r [16]. Our data show that the outer scale monotonically increases with r out to heliocentric distances $r = 100R_s$. It is likely that the mechanisms for the formation of the solar-wind turbulence differ near the inner and outer turbulence scales at different distances from the Sun. It is worthwhile to continue studies of the outer scale via prolonged, continuous observations of the electron density using instruments on spacecraft.

The observational data analyzed here correspond to the slow, low-latitude solar wind in a period of minimum solar activity. Figure 7c shows that this solar wind is accelerated quite slowly, and achieves a well-established regime with $v =$ const at heliocentric distances exceeding $20R_S$.

In the theoretical model considered here, the main turbulence scale delineates spectral regions dominated by linear and nonlinear effects. The outer scale is increased by a shift of the inner boundary of the inertial (nonlinear) spectral interval toward lower fluctuation frequencies as the turbulence is carried away by the solar wind. Among the mechanisms for cascade energy transfer considered here (strong Kolmogorov interactions, three-wave and four-wave processes), the three-wave decays of energetic Alfven waves with the participation of magnetoacoustic waves gives the best description of the observed radial evolution of the outer turbulence scale. This same process also provides a natural explanation for the local generation of solar-wind density fluctuations. Estimates based on the observed values of the outer turbulence scale demonstrate that the fractional level of Alfven turbulence (and the corresponding magnetic-field fluctuations) increases in the antisolar direction, becoming fairly high even in inner regions of the established solar wind, and may tend to become saturated at a level near unity (strong turbulence) at heliocentric distances of about 0.5 AU. In subsequent studies of nonlinear wave processes in the turbulent solar wind, it will be very interesting to measure the dependence of the outer turbulence scale (22)–(24) on local plasma parameters (such as the solar-wind and Alfven velocities). This analysis will require considerably more extensive observational data, which should enable us to compare the outer turbulence scales in flows with substantially different velocities at approximately the same distances from the Sun. This could be realized through simultaneous (or nearly simultaneous) radio sounding at high and low heliolatitudes in a period of minimum solar activity.

ACKNOWLEDGEMENTS

This work was supported by the Russian Foundation for Basic Research, project nos. 00-02-17665 and 00-02-17845; the Program of Binational Cooperation between the RFBR and DFG (Germany), project code 00-02-04022; and the "Astronomiya" Federal Scientice and Technology Program.

REFERENCES

1. O. I. Yakovlev, B. P. Trusov, V. A. Vinogradov, *et al.*, Kosm. Issled. **12** (4), 600 (1974).
2. R. Woo, Astrophys. J. **219**, 727 (1978).
3. M. K. Bird and P. Edenhofer, in *Remote Sensing Observations of the Solar Corona, Physics of the Inner Heliosphere,* Ed. by R. Schwenn and E. Marsch (Springer-Verlag, Heidelberg, 1990).
4. A. I. Efimov and O. I. Yakovlev, *Electromagnetic Waves in Atmosphere and Space* [in Russian] (Nauka, Moscow, 1986).
5. P. Janardhan, M. K. Bird, P. Edenhofer, *et al.*, Sol. Physics **184** (1), 157 (1999).
6. H. T. Howard, V. R. Eshleman, D. P. Hinson, *et al.*, Space Sci. Rev. **60** (2), 565 (1992).

7. R. Wohlmuth, D. Plettemeier, P. Edenhofer, M. K. Bird, and S. W. Asmar, in *The Three Galileos: The Man, The Spacecraft, The Telescope,* Ed. by C. Barbieri *et al.* (Kluwer, Dordrecht, 1997), p. 421.
8. N. A. Armand, A. I. Efimov, and O. I. Yakovlev, Astron. Astrophys. **183** (1), 135 (1987).
9. R. Wohlmuth, D. Plettemeier, P. Edenhofer, *et al.*, Radio Sci. **32** (2), 617 (1997).
10. V. P. Yakubov, *Doppler Very Long Baseline Interferometry* [in Russian] (Tomskiĭ Gos. Univ., Tomsk, 1997).
11. A. I. Efimov, O. I. Yakovlev, V. K. Shtrykov, *et al.*, Radiotekh. Elektron. (Moscow) **26** (2), 311 (1981).
12. O. I. Yakovlev, A. I. Efimov, V. P. Yakubov, *et al.*, Izv. Vyssh. Uchebn. Zaved., Radiofiz. **32** (5), 531 (1989).
13. O. I. Yakovlev, A. I. Efimov, V. M. Razmanov, and V. K. Shtrykov, Astron. Zh. **57** (4), 790 (1980) [Sov. Astron. **24**, 454 (1980)].
14. P. S. Callahan, Astrophys. J. **199** (1), 227 (1975).
15. J. K. Harmon and W. A. Coles, Astrophys. J. **270** (2), 748 (1983).
16. P. K. Manoharan, S. Ananthakrishnan, and A. P. Rao, in *Solar Wind Six: Proceedings of the 6th International Solar Wind Conference,* Ed. by V. J. Pizzo *et al.* (1988), p. 55.
17. I. V. Chasheĭ and V. I. Shishov, Pis'ma Astron. Zh. **7** (8), 500 (1981) [Sov. Astron. Lett. **7**, 276 (1981)].
18. I. V. Chasheĭ and V. I. Shishov, Geomagn. Aeron. **25** (1), 1 (1985).
19. C. Y. Tu, Z. Y. Pu, and F. S. Wei, J. Geophys. Res. **89**, 9695 (1984).
20. C. Y. Tu and E. Marsch, Space Sci. Rev. **73**, 1 (1995).
21. I. V. Chasheĭ and V. I. Shishov, Geomagn. Aeron. **17** (6), 984 (1977).
22. J. W. Belcher and L. Davis, J. Geophys. Res. **76**, 3534 (1971).
23. I. V. Chasheĭ and V. I. Shishov, Astron. Zh. **65** (1), 157 (1988) [Sov. Astron. **32**, 81 (1988)].
24. I. V. Chasheĭ, Geomagn. Aeron. **29** (5), 718 (1989).
25. Y. Q. Hu, S. R. Habbal, and X. Li, J. Geophys. Res. **104**, 24819 (1999).
26. I. V.Chasheĭ, Astron. Zh. **74** (1), 93 (1997) [Astron. Rep. **41**, 85 (1997)].
27. D. Montgomery, M. Brown, and W. H. Matthaeus, J. Geophys. Res. **92**, 282 (1987).
28. G. P. Zank and W. H. Matthaeus, Phys. Fluids A **5**, 257 (1993)
29. W. H. Matthaeus and M. L. Goldstein, Phys. Rev. Lett. **57**, 495 (1986).
30. A. A. Ruzmaikin, B. E. Goldstein, and E. J. Smith, in *Solar Wind Eight*, Ed. by D. Winterhalter *et al.* (American Inst. of Physics Press, Woodbury, 1996), AIP Conf. Proc. **382**, 225 (1996).
31. I. V. Chashei, A. I. Efimov, L. N. Samoznaev, *et al.*, Adv. Space Res. **25** (9), 1973 (2000).
32. J. R. Jokipii and P. J. Coleman, J. Geophys. Res. **73** (17), 5495 (1968).
33. W. H. Matthaeus and M. L. Goldstein, J. Geophys. Res. **87** (A8), 6011 (1982).
34. R. Bruno and M. Dobrowolny, Ann. Geophys. **4** (1), 17 (1986).
35. U. Villante, J. Geophys. Res. **85** (A12), 6869 (1980).

Translated by Yu. Dumin

Astronomy Reports, Vol. 46, No. 7, 2002, pp. 591–596. Translated from Astronomicheskiĭ Zhurnal, Vol. 79, No. 7, 2002, pp. 653–658.

Plasma Motion in Crossed Fields and Halo-Type Coronal Mass Ejections

M. M. Molodenskiĭ and N. S. Shilova

Institute of Terrestrial Magnetism, Ionosphere, and Radio Wave Propagation, Russian Academy of Sciences, Troitsk, Moscow oblast, 142190 Russia

Received September 5, 2001; in final form, October 19, 2001

Abstract—Halo-type motions of plasma in the solar corona—so-called coronal mass ejections (CME)—are considered. This type of CME is relatively rare due to the requirement for a particular orientation of the magnetic-moment vector **M** (parallel to the line of sight). Variations in $|\mathbf{M}|$ may be due to the rapid motion of filaments with a characteristic time scale $\cong 10^3$ s. The drifts in the crossed fields have speeds of $\cong$200–1000 km/s and can account for the basic features of the CME geometry. © *2002 MAIK "Nauka/Interperiodica".*

1. OBSERVED FEATURES OF HALO CMEs

Regions of enhanced white-light coronal emission surrounding the occulting disks of the LASCO C2 and C3 coronagraphs of SOHO over 360° or slightly smaller position angles are called halo coronal mass ejections (CMEs). A full halo is present in the first and a partial halo in the second case. Such CMEs are believed to propagate from the Sun radially nearly toward or away from the Earth. Statistical investigations [1, 2] confirm the high geomagnetic efficiency of such coronal transients. According to [1], 90% of geomagnetic storms follow halo events. However, only two-thirds of halos are accompanied by increases in geomagnetic activity.

Halo CMEs are appreciably less frequent than other types of transients. In their analysis of halo CMEs occurring in 1966 and 1997, Webb *et al.* [2] noted that such CMEs occurred once every 22 days in 1966 and once every 4 days in 1997. Let us consider the list of LASCO CMEs (available via the Internet).

On average, halo CMEs occurred once every 5 days in 1998 and 1999. At the same time, during years of solar-activity maximum, other types of CMEs occur more often than once per day. Thus, halo-type transients are much less frequent than other types of transients, and the number of halos is extremely small in years of solar minimum.

In many cases, investigators cannot associate the emergence of a halo with manifestations of activity on the visible solar disk. For instance, 532 CMEs were observed from February 5–August 31, 1999, and only 40 among them were halo CMEs. Only five of these halo CMEs can be attributed to events on the visible solar disk; the sources for 13 are not known, and 22 halo CMEs may be related to events on the back side of the Sun. At the same time, attempts to identify the remaining, non-halo CMEs have been quite successful (since movies of the disk are at the disposal of EIT and Yohkoh observers). Only 3 out of 492 non-halo events must be attributed to phenomena on the back side of the Sun.

This means that halos form the only class of CMEs for which a usual source (flare or disappearance of a filament) cannot be found in many cases, so that one must invoke events on the back side of the Sun. A similar situation was observed in 1998. Difficulties with identifying the sources of halos are also connected with the fact that pairs of halos on a single day or two successive days occur very frequently. Observers seek different sources for them, although a common, or at least partially common, source is very likely.

It is interesting that solar activity has frequently been weak even in cases of highly geomagnetic-efficient halos (e.g., on January 10–11, 1997). This raises the problem of the lack of signatures for eruptive solar activity on the solar surface concurrent to the appearance of halos. The impression is formed that, unlike usual coronal transients, halo-type transients may result not from individual solar events, but from combinations of several events with relatively low efficiency (in terms of CME formation) localized in a particular position angle, such as a large number of subflares. In particular, both a full and a partial halo were observed on August 9 and 10, 2000.

The first halo was accompanied by a magnetic storm near the Earth on August 11. At that time, the complex of active regions 9114 and 9115 was located at the center of the visible hemisphere of the Sun, with an arcade of EIT loops SE of the complex, related to a filament that had disappeared: August 8, 2000, 09:30–23:36 UT S32W40. Apart from the disappearance of the filament, three subflares in region 9114 (at

1063-7729/02/4607-0591$22.00

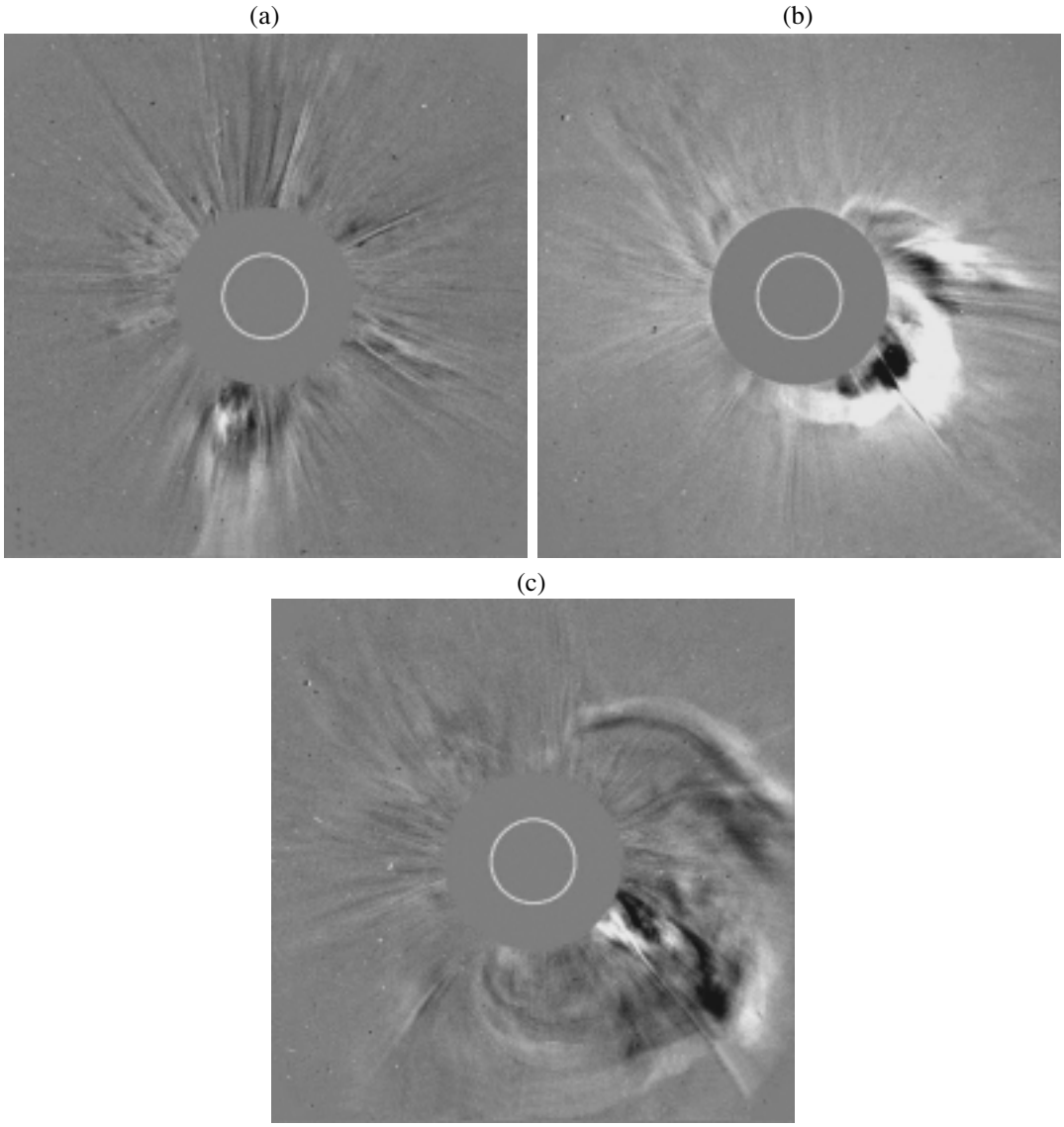

Fig. 1. Difference filtergrams of the LASCO C2 halo events of (a) December 29, 1999, at 01:31 UT and November 23, 2000, at (b) 08:30, and (c) 09:54 UT.

17:35, 18:04, 18:17 UT) could be associated with the observed halo, but none dominated over the others. Since no especially distinguished event was observed on either August 9 or 10, the halo of August 9 in the LASCO list of CMEs was tentatively assigned to activity associated with active region 9114, and the halo of August 10 to some events on the visible side of the Sun. Identification of the source of a halo CME becomes much less reliable when a large number of subflares are observed on the disk. In particular, in the afternoon of August 12, 2000, the emission in the field of view of C3 was extended over about 150° in position angle, and 22 subflares were present over the disk on that day. It is highly probable that the partial halo of August 12 was induced by a series of subflares.

The structure of the heliospheric current sheet is seen in outline only when a halo CME appears. Let us consider difference filtergrams from the C2 coronograph, e.g., for the halo of December 29, 1999 (Fig. 1a). Any halo initially exhibits a transient that appears in the field of view of C2, after which weaker emission at different position angles attaches itself to this transient (Figs. 1b, 1c). We do not consider here the structure of the region of most intense emission and focus our attention on the structure of the moderate-intensity background. Obviously, the heliospheric current sheet contains a multitude of rays, which have sizes of no more than 2×10^4 km at a heliocentric distance of 2.5 solar radii. This means that the transverse scale of the heliospheric current sheet network is close to the size of supergranules or chromospheric magnetic-field structures.

2. CHANGES IN THE DIPOLE MAGNETIC MOMENT OF THE SUN AS THE ORIGIN OF HALOS

A loop with a bright core and fragments of a prominence resembling a twisted rope inside is known to be the most likely configuration for coronal mass ejections. The electric-current energy in such a "rope" exceeds the energy of the potential magnetic field and is transformed into the kinetic energy of the CME. We distinguish the drift velocity of the plasma in the crossed electric and magnetic fields from the velocity of the material as a whole.

We already considered a mechanism for the rapid motion of a filament, with a stable configuration formed by the (not-too-large) current of the filament interacting with the field of the active region and with the field of the current reflected from the photospheric surface [3, 4]. In this situation, the field is potential, and equilibrium is possible at two points, being stable at one point (the potential minimum) and unstable at the other (a saddle). As the filament current increases, these points approach each other, and, at a certain critical current, the potential surface smoothens out and the extremum (equilibrium) points disappear. In mathematics, this situation is called an assembly-type catastrophe.

It is important in this case that the filament current, whose dipole moment is comparable to that of the active region, is set in rapid motion. The characteristic time for this process, R/V, is $\sim 10^3$ s for $R = 7 \times 10^{10}$ cm and $V = 500$ km/s.

Observations with the Great Coronagraph at the Mountain Astronomical Station of the Main Astronomical Observatory in June and July 1989 [3] were used to compare the parameters of eruptive prominences with finite and infinite motions. If the disappearance of a filament is observed at the limb, a prominence is ejected, with a characteristic rising time of about half an hour (10^3 s). This time scale seems to characterize the rate of variation of the magnetic moment.

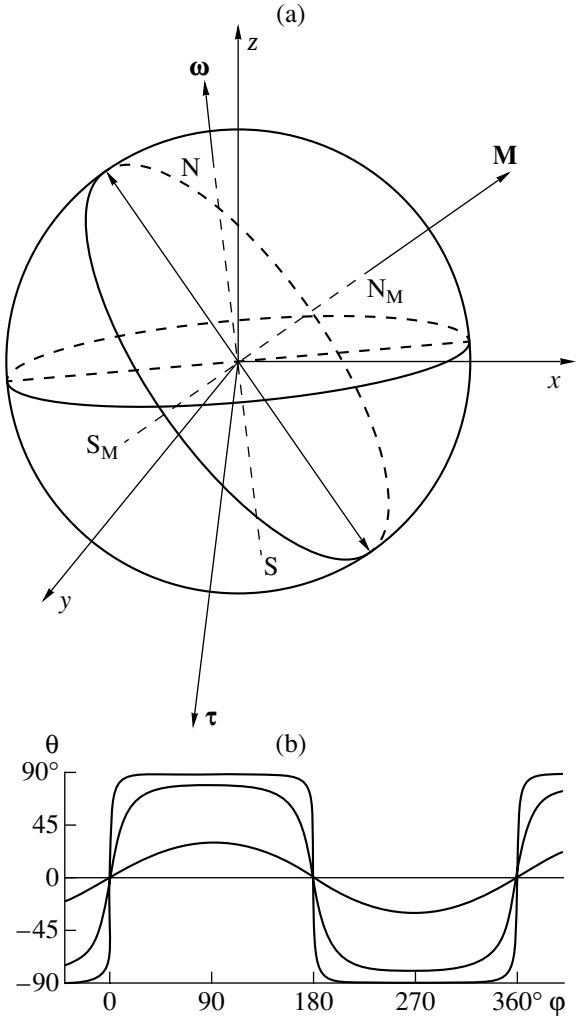

Fig. 2. (a) The three vectors ω, $\mathbf{M}$, and τ determining the positions of the solar (geographic and magnetic) poles and equators, as well as the center and limb of the Sun (the vector τ). (b) Schematic of a synoptic map with a sinusoidally shaped magnetic equator corresponding to a dipole for $M_e/M_z < 1$ and a meandering equator for $M_e/M_z > 1$.

3. ORIENTATION OF THE HELIOSPHERIC CURRENT SHEET RELATIVE TO AN EARTH-BASED OBSERVER DURING A HALO CME

The preferred position angles for the appearance of CMEs have been studied many times. For example, Hundhausen [5] considered SMM data for transients occurring in 1984 and showed that they preferentially originated near the magnetic equator. Later, Shilova and Vanyarkha [6] and Ivanov *et al.* [7] used data obtained in 1979–1985 to confirm that most white-light CMEs move away from the source surface into space near the neutral line of the source-surface field. Gulyaev and Vanyarkha [8] studied regularities in the variations of the orientation of a heliospheric current sheet in the course of the solar cycle. In their analysis, they abstracted themselves from the actual configuration of the sheet and considered a smoothed configuration, introducing the concept of the midplane of the heliospheric layer as the plane that passes through the Sun's center and is closest to the observed configuration of the layer near the Sun. However, they noted that the angle between the magnetic axis and the Sun's rotational axis for the epoch of solar-activity maximum had not been determined. We attempt to do this here.

Heliographic latitudes are measured from the he-

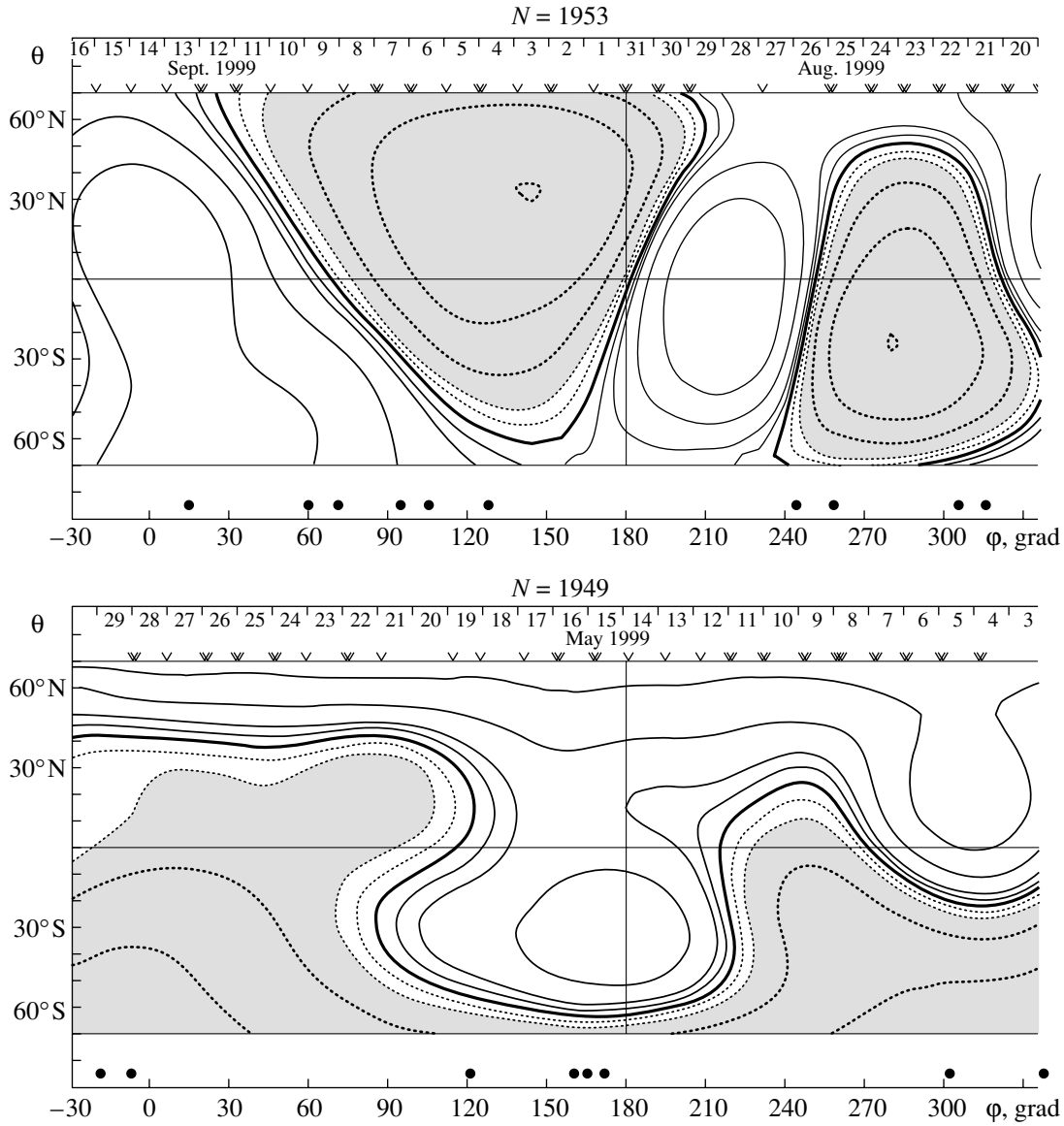

Fig. 3. Field at the source surface ($2.5R_0$) according to the Wilcox Observatory data for Carrington rotations 1949 and 1953. Times of halos are marked by the points on the longitude axis. The variation scale is 0, ±0.5, ±1.0, ±2.5, ±5.0, ±10.0.

liographic equatorial plane in both the round maps published in *Solar Geophysical Data* and synoptic maps of the configuration of the heliospheric current sheet—Hoeksema curve (see [9]). For convenience, this projection is used in Earth-based observations when the ON direction coincides with the direction of the Sun's rotational axis (O is the center of the sphere and N is the northernmost point) and the plane normal to ON coincides with the heliographic equatorial plane.

In fact, three vectors are used: the angular-velocity vector ω, the magnetic-moment vector $\mathbf{M}$, and the unit vector along the line of sight τ. The heliographic poles N and S, the magnetic poles N_M and S_M, and the heliographic and magnetic equator are defined accordingly. The vector τ is directed from the Sun's center toward the observer (Fig. 2a).

The heliographic equator is inclined to the plane of the Earth's orbit by only 7.5°, and we can assume to sufficient accuracy that $(\omega\tau) = 0$. The dipole axis $\mathbf{M}$ can have various directions. Accordingly, the magnetic equator (i.e., the line $B_r = 0$) will look different in a $B_r(r, \theta, \varphi)$ map. We write

$$\mathbf{M} = \mathbf{e}_x M_x + \mathbf{e}_y M_y + \mathbf{e}_z M_z \qquad (1)$$

and the position vector in spherical coordinates

$$\mathbf{r} = \mathbf{e}_x r \sin\theta \sin\varphi + \mathbf{e}_y r \sin\theta \cos\varphi + \mathbf{e}_z r \cos\theta, \quad (2)$$

where θ and φ are latitude and longitude, respectively. We replace the spherical coordinates with heliocentric

coordinates (making the substitution $\theta \to \pi/2 - \theta$) and impose the condition that $\mathbf{r}$ lies in the magnetic-equator plane, i.e., $(\mathbf{Mr}) = 0$, to obtain

$$M_x r\cos\theta\sin\varphi + M_y r\cos\theta\cos\varphi + M_z r\sin\theta = 0. \quad (3)$$

Using this formula to express θ in terms of φ, we find

$$\theta = -\arctan\frac{M_X\sin\varphi + M_Y\cos\varphi}{M_Z}. \quad (4)$$

We then assume that $M_\mathrm{e} = \sqrt{M_x^2 + M_y^2}$, $M_x/M_\mathrm{e} = \sin\varphi_0$, and $M_y/M_\mathrm{e} = \cos\varphi_0$, thus obtaining

$$\theta = -\arctan\left[\frac{M_\mathrm{e}\cos(\varphi - \varphi_0)}{M_z}\right].$$

Curves of $\theta(\varphi)$ for various M_e/M_z are shown in Fig. 2b. They are sinusoidal for $M_\mathrm{e}/M_z < 1$ and meandering for $M_\mathrm{e}/M_z > 1$.

An actual magnetic-field map obtained at the Wilcox Observatory in which the $B_r = 0$ curve has precisely this form is shown in Fig. 3. Times when halos appeared are marked by points in this figure. We can see that these are concentrated near high-latitude positions of the magnetic equator, and never occur when the magnetic equator intersects the heliographic equator.

Thus, an ideal halo corresponds to times when the magnetic equator is at the solar limb.

The drift velocity can be expressed in terms of the vector potential $\mathbf{A}$ and the magnetic field $\mathbf{B}$ as

$$\mathbf{V} = \frac{[\mathbf{B}\dot{\mathbf{A}}]}{B^2}, \quad (6)$$

where $\dot{\mathbf{A}} = \dfrac{\partial\vec{A}}{\partial t}$. For a dipole,

$$\mathbf{A} = \{0, 0, A_\varphi\}, \quad A_\varphi = \frac{M\sin\vartheta_1}{r^2}, \quad (7)$$

and

$$\mathbf{B} = \mathbf{e}_r\frac{2M\cos\vartheta_1}{r^3} + \mathbf{e}_\theta\frac{M\sin\vartheta_1}{r^3}. \quad (8)$$

Substituting (7) and (8) into (6) yields

$$\mathbf{V} = \frac{\dot{M}}{M}\frac{r\sin\theta_1}{f(\theta_1)}(\mathbf{e}_r\sin\theta_1 - \mathbf{e}_\theta 2\cos\theta_1), \quad (9)$$

$$f(\theta_1) = 4\cos^2\theta_1 + \sin^2\theta_1.$$

where θ_1 is the angle of the spherical coordinate system related to the dipole moment $\mathbf{M}$. The modulus of this quantity is maximum when $\theta_1 = 90°$. Obviously, in projection onto the plane of the sky, the brightness variation in the halo pattern will be the same: as the position angle around the Sun is varied, a maximum is reached, and the velocity and brightness of the CME decrease with recession from this maximum. If the disappearance of a filament is observed at the limb, a prominence is ejected, with a characteristic rising time of about half an hour [3]. This time scale seems to characterize the rate of variation of the magnetic moment.

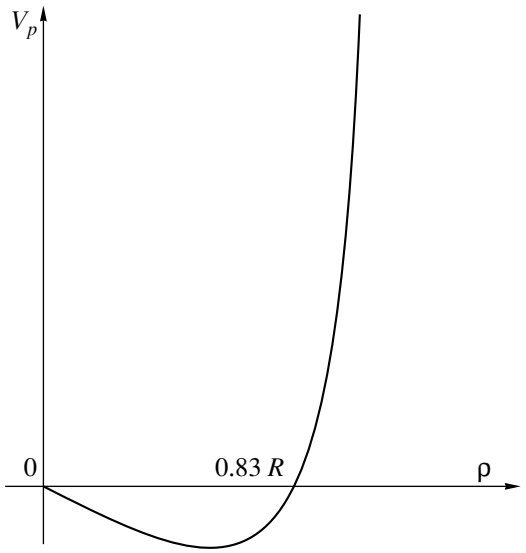

Fig. 4. Velocity of the shell projected onto the plane of the sky as a function of the distance ρ (see text).

Thus, we find from (5) that $V = 200$ km/s at $1R_\odot$ and $V = 1000$ km/s at $5R_\odot$, and the mechanism described above yields values that have quite acceptable absolute magnitudes. The velocity histogram for halo CMEs in the field of view of the SOHO coronagraphs has a maximum at 800–1000 km/s [10].

It is the velocity component normal to the line of sight that is observable. Therefore, $\mathbf{V}$ in (9) should be projected onto the plane of the sky. If the dipole is $\mathbf{M} \parallel \tau$, then

$$V_\rho = V_r\sin\theta_1 + V_\theta\cos\theta_1, \quad (10)$$

where ρ is the heliocentric distance in the plane of the sky. Substituting (9) into (10), we obtain

$$V_\rho = \frac{\dot{M}}{M}\rho\frac{1 - 3\cos^2\vartheta_1}{1 + 3\cos^2\vartheta_1}. \quad (11)$$

In addition, we assume that the radiation is emitted by a thin spherical shell of radius R centered on the Sun; then

$$\rho^2 + \left(\rho\frac{\cos\vartheta_1}{\sin\vartheta_1}\right)^2 = R^2, \quad (12)$$

and (11) assumes the form

$$V_\rho = \frac{\dot{M}}{M}Rx\frac{3x^2 - 2}{4 - 3x^2}, \quad (13)$$

where $x = \rho/R$. The dependence (13) is shown in Fig. 4. We can see that rapid motion occurs in the plane of the sky, with the maximum velocity at the surface (12) (Figs. 1b, 1c).

Finally, we note that our considerations are applicable not only to the first (dipole) term of the expansion of the potential into spherical functions $M\frac{P_1(\cos\vartheta_1)}{r^2}$ but also to any term of the form $C_n\frac{P_n(\cos\vartheta_1)}{r^{n+1}}$ $(m = 0)$, provided that the symmetry axis of the corresponding harmonic is directed along the vector τ at the time of the disturbance ($\dot{C}_n \neq 0$).

4. CONCLUSION

We have shown that the characteristic features of halo-type CMEs can be accounted for by the fact that halos are the only type of CME for which the heliographic equator is perpendicular to (or makes a large angle with) the surface of the heliospheric current sheet. This enables an Earth-based observer to study the structure of the heliospheric current sheet in its plane while observing halo CMEs. We find support for the hypothesis that the dipole moment of the Sun as a whole changes during halo CMEs, since disturbances from several sources of surface activity are added.

ACKNOWLEGMENTS

This work was supported by the Russian Foundation for Basic Research, project nos. 00-02-16360, 00-02-17736, and 00-02-16090; and the State Science and Technology Program in Astronomy.

REFERENCES

1. E. Hildner, O. C. St Syr, A. T. Herlihy, *et al.*, in *Abstracts of IUGG99* (International Union of Geodesy and Geophysics, Birmingham, 1999), GA4.01/W/030A2, p. A362.
2. D. F. Webb, E. W. Cliver, N. U. Crooker, *et al.*, J. Geophys. Res. **105**, 7491 (2000).
3. M. M. Molodenskiĭ, B. P. Filippov, and N. S. Shilova, Astron. Zh. **69**, 181 (1992) [Sov. Astron. **36**, 92 (1992)].
4. M. M. Molodenskiĭ and B. P. Filippov, *Magnetic Fields of Solar Active Regions* [in Russian] (Nauka, Moscow, 1992), p. 151.
5. A. J. Hundhausen, J. Geophys. Res. **98**, 13177 (1993).
6. N. S. Shilova and N. Ya. Vanyarkha, Geomagn. Aeron. **38**, 135 (1998).
7. E. V. Ivanov, V. N. Obridko, E. V. Nepomnyasdchaya, and N. V. Kutilina, Sol. Phys. **184**, 369 (1999).
8. R. A. Gulyaev and N. Ya. Vanyarkha, Sol. Phys. **140**, 369 (1992).
9. J. T. Hoeksema, J. M. Wilcox, and P. H. Scherrer, J. Geophys. Res. **88**, 9910 (1983).
10. M. A. Lyons, A. B. Stockton-Chalk, and D. J. Lewis, in *Proceedings of the 9th European Meeting on Solar Physics: Magnetic Fields and Solar Processes, Florence, 1999,* Ed. by A. Wilson, ESA SP-448, Vol. 2, Sess. 6, p. 943.

Translated by A. Getling

Astronomy Reports, Vol. 46, No. 7, 2002, pp. 597–608. Translated from Astronomicheskiĭ Zhurnal, Vol. 79, No. 7, 2002, pp. 659–672.

Common Features in the Development of Powerful Long-Duration Solar X-ray Flares

M. A. Livshits, O. G. Badalyan, and A. V. Belov

Institute of Terrestrial Magnetism, Ionosphere, and Radio Wave Propagation, Russian Academy of Sciences, Troitsk, Moscow oblast, 142190 Russia

Received October 19, 2001; in final form, November 23, 2001

Abstract—We have begun an investigation of the possible origins of considerable of powerful solar flares. This effect is manifest, first and foremost, in the existence of high-temperature plasma in flare loops over many hours. Analysis of the soft X-ray emission in two energy bands detected by the GOES satellites for about 20 powerful solar flares reveals long time intervals during the decay phase when the source temperature decreases, in general, exponentially. The characteristic time t_i for a decrease in the temperature by a factor of ten is 3–10 hours for most powerful events. In addition, another interval of very slow decrease with a characteristic time t_i of tens of hours can be identified in some cases. We found a gradual change in the dependence of the temperature on the square root of the emission measure for the source as a whole, which characterizes the transition from purely coronal processes to powerful flares with a prolonged inflow of plasma from the chromosphere. Modeling the energy balance in a loop can yield the requirements for the source of plasma heating in a long-lived arch system. A necessary condition for the development of prolonged flares seems to be a powerful coronal mass ejection, which initiates the formation of a source of plasma heating at coronal heights. Our analysis shows that a considerable fraction of the energy is often released in the region of the cusp, and that systems of giant coronal arches rising to heights of about 100 000 km above the limb are formed in most prolonged events (called dynamical flares in the terminology of Svestka). © *2002 MAIK "Nauka/Interperiodica"*.

1. INTRODUCTION

Large solar flares are very complex and often involve several different non stationary processes. Because of the variety in their observational manifestations, especially in the optical, there do not at first appear to be common features in the development of these phenomena. However, this point of view has been changing in recent years, as virtually real-time observations of solar flares in various spectral ranges have become available, including magnetic-field measurements. Large, uniform datasets on the soft X-ray emission of 51 000 solar flares have been accumulated, and hundreds of X-ray sources—systems of flare coronal loops—have been studied in detail.

It is now known that a system of hot loops is formed over a neutral line after a sudden impulsive energy release, followed by plasma heating and particle acceleration. The existence and gradual radiative cooling of such loops are the most characteristic elements of X-ray (two-ribbon) flares. The majority of flares with durations of about 1 h are of this type. The physical conditions in solar-flare coronal loops can be derived from observations quite reliably. Note also that the first observational evidence in favor of magnetic-field reconnection as a source of the primary energy release in two-ribbon flares was obtained only recently [1, 2]. One characteristic feature of the limb flare of February 21, 1992, studied in [1, 2] was the cusp-like shape of its soft X-ray image, with prolonged energy release near the top of the loop.

Another important factor in these studies has been the acquisition of a large volume of information about coronal mass ejections (CMEs) and the consideration of both flares and CMEs in the framework of joint non-stationary processes.

The present paper is concerned with possible differences between ordinary two-ribbon flares and more powerful phenomena with complex spatial and temporal structures. The basis for our analysis was a uniform data on the soft X-ray emission of powerful flares. Naturally, we also made use of radio data and information about the detection of CMEs as well as a theoretical analysis of the energy balance in flare loops. In conclusion, we shall discuss possible reasons for appreciable prolongation of the soft X-ray emission of the powerful flares under consideration.

2. THE OBSERVATIONAL DATA

Our analysis is based on data obtained by the GOES satellites. One of us (A. V. B.) used these

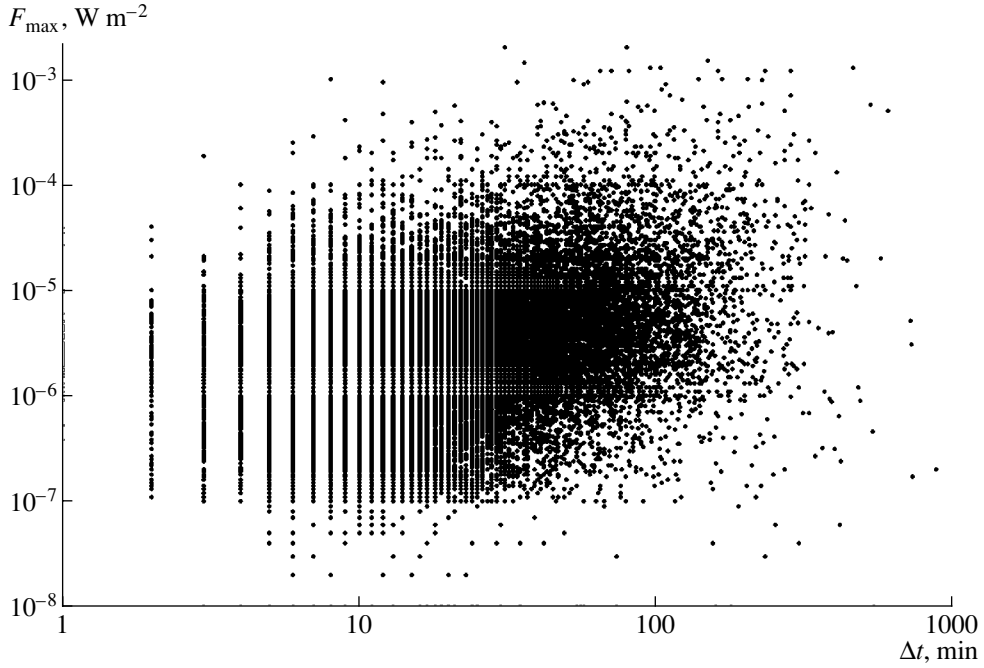

Fig. 1. The maximum flux at 1–8 Å as a function of the flare duration for all events in the database.

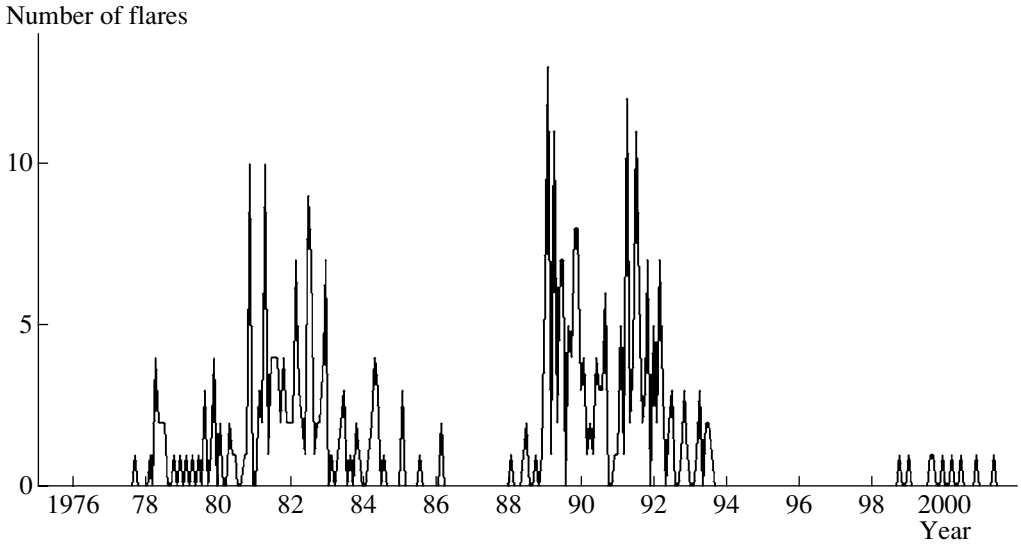

Fig. 2. Time distribution of the number of flares brighter than M1 with durations exceeding 120 min.

observations to compile a database of X-ray flares containing about 51000 events. The database includes the time of the onset of each event together with its duration, heliographic coordinates, and X-ray class (i.e., the maximum X-ray flux at 1–8 Å), as well as inferred characteristics of the accelerated particles and solar-wind flows associated with the event.

The maximum fluxes of the flares in the 1–8 Å band and their durations according to the GOES data are presented in Fig. 1. We will define the duration Δt as the time interval corresponding to 0.1 of the maximum intensity level. The quantities in Fig. 1 are discrete, because Δt is measured to within one minute and the X-ray class of the flare is measured to within 0.1 of the mantissa of the flux. Recall that X-ray classes B, C, M, and X correspond to fluxes near the Earth exceeding 10^{-7}, 10^{-6}, 10^{-5}, and 10^{-4} W/m^2, respectively; the flux of an X10 flare at 1–8 Å corresponds to 1 erg cm^{-2}s^{-1}.

Impulsive events with various intensities lie in

the left-hand part of Fig. 1. Events with durations over 10 min are primarily two-ribbon X-ray flares. As can be seen in Fig. 1 (and the corresponding histograms), the mean duration of two-ribbon flares is very close to $\Delta t = 1$ h. More prolonged events tend to become more powerful as Δt increases. This behavior is manifest in Fig. 1 in the appreciable inclination of the lower and upper envelopes of the distribution of prolonged events to the vertical axis. The origin of this tendency will be discussed below.

We separated out events with fluxes $F \geq 10^{-5}$ W/m^2 (class M1 and higher) and durations exceeding 120 min from the database. Figure 2 presents the distribution of the number of such events as a function of time; they are concentrated around times just before and after the cycle maximum. On the other hand, such flares are less frequent precisely at the maximum (i.e., near the field reversal). Note that there is a very small number of powerful prolonged flares in the current (23rd) cycle.

Five-minute data suitable for the analysis are available for both channels (1–8 and 0.5–4 Å) of the GOES satellites starting in 1988. We restricted our analysis to flares of classes above M1 with durations exceeding 180 min. There are about 80 such flares in the database. The corresponding points are located in the upper right-hand corner of Fig. 1. For completeness of the analysis and comparison with well-studied examples of flares, we added several shorter events to this sample: the purely coronal event of June 20, 1993; two well-studied flares (March 6 and 15) from a series of prolonged phenomena in March 1993; the Bastille Day flare of July 14, 2000 [3] (a two-ribbon flare composed of two coronal systems); and two sigmoidal flares [4]. The final list of analyzed events is presented in the first two columns of Table 1.

Thus, we chose powerful, prolonged X-ray flares and several other well-studied flare events for analysis using a single method.

3. TEMPORAL BEHAVIOR OF THE SOFT X-RAY EMISSION OF POWERFUL FLARES

The soft X-ray fluxes in the two energy intervals enable us to derive the temperature T and emission measure EM in the source. We will use a single-temperature approximation. For any particular GOES satellite, the flux in each channel is proportional to the emission measure multiplied by some function of the temperature. The ratio of the fluxes in the two channels enables us to find the temperature, and the emission measure is then determined by the flux in one of these channels. The method used to determine T and EM is described in [5]. This paper also gives the coefficients of proportionality between the current measured by a device and the radiation

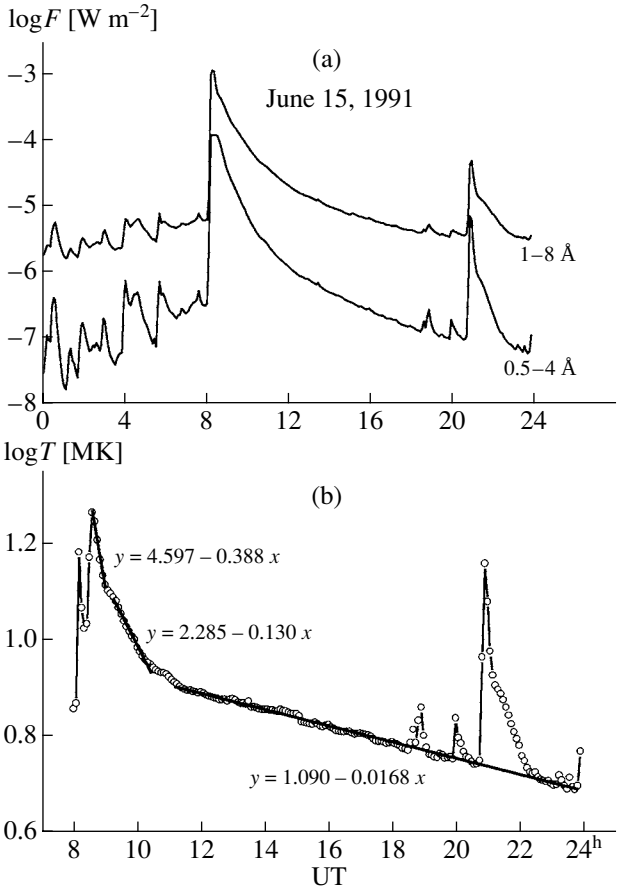

Fig. 3. (a) X-ray fluxes in two channels of the GOES-7 satellite and (b) temporal behavior of the temperature T for the flare of June 15, 1991. The straight lines show approximations of the temperature behavior for three separate time intervals. The variable y is the logarithm of the temperature in MK, and x is the time in hours.

fluxes in the two channels of the satellites (up to GOES-7 inclusive) and presents a theoretical X-ray spectrum calculated by Mewe *et al.* [6] for a fixed emission measure (in our case, EM = 10^{50} cm^{-3}).

The main difference of the powerful phenomena analyzed here from ordinary two-ribbon flares is the temporal behavior of their physical parameters in the decay phase. Since we consider very prolonged events, we will use five-minute integrations of the X-ray fluxes. This temporal resolution is sufficient to study the decay phase of the flares, but makes it difficult to use the same data to study the impulsive phase. In addition, there was a flux saturation in one or both channels near the maxima of the most powerful events. Therefore, we formally calculated the temperature distributions for the entire time interval but did not use values near the maxima in the final analysis.

In principle, even the temporal behavior of the X-ray fluxes of some powerful flares in either the 1–

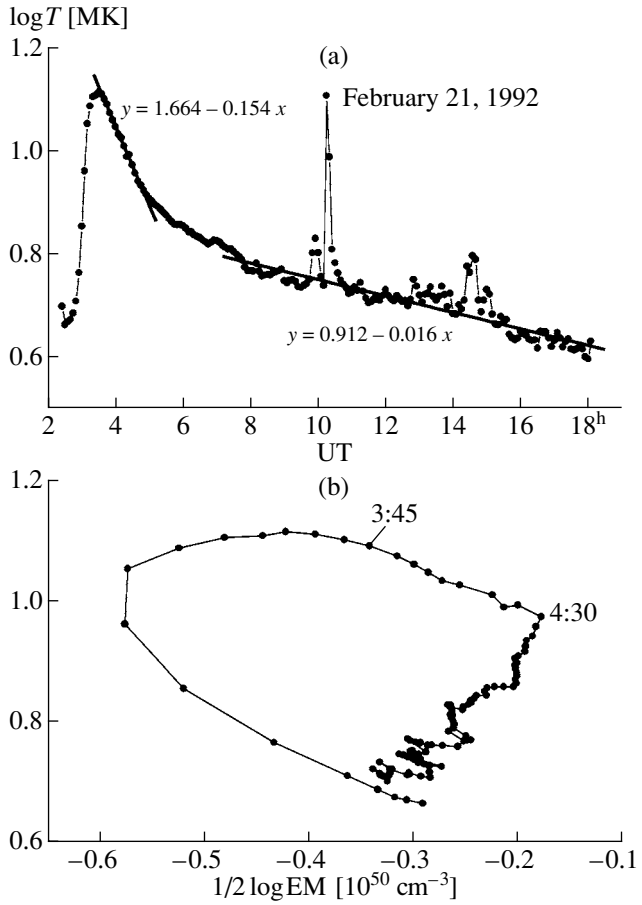

Fig. 4. (a) Time dependence of the temperature for the flare of February 21, 1992. An approximation similar to that in Fig. 3b is presented for this limb flare in the second and third intervals. (b) Comparison of $\log T$ and $1/2 \log$ EM at the same times. Time changes in the clockwise direction, and two UT times are marked.

8 Å or 0.5–4 Å band indicates that fairly large fluxes can last over 2 h, i.e., longer than the maximum glow time for two-ribbon flares (even those consisting of several arch systems). Of course, more valuable information can be derived from an analysis of the real physical characteristics (T, EM) in the emission source.

As an example, Fig. 3a shows the X-ray fluxes for the flare of June 15, 1991 at coordinates N33 and W69, whose X-ray magnitude exceeded X12. The flux saturation near the maximum of this event is visible. The flare began at 8:10 UT, and white-light emission was observed in a strong impulse. A two-ribbon flare in the active region and most of the very hard γ-ray emission ended at 8:50 UT. A system of giant loops formed after 10:00 UT at a considerable distance from the active region and was observed in Hα approximately until the end of the day (see, for example, [7, 8] and references therein).

Figure 3b presents the temperature behavior for this event. A set of time intervals in which $\log T$ is well approximated by straight lines can usually be distinguished in the phase of declining flare emission. The characteristic time for the exponential temperature decrease $t_i = (d \log T/dt)^{-1}$ is determined by the slope for the corresponding line segment. The t_i values for the flares in the upper right-hand corner of Fig. 1 exceed 2 h.

The characteristic times for the June 15, 1991 flare are $t_1 = 2.6$, $t_2 = 7.7$, and $t_3 = 59.5$ h. The corresponding time intervals refer to three characteristic stages in the flare development. The first is the end of a very powerful two-ribbon flare at the activity center. The second stage seems to correspond to the development of a cusp. Such cusp structures could not be detected directly before the launch of the Yohkoh satellite, but indirect conclusions can be drawn based on the measurement of a decimeter radio outburst at 327–610 MHz at 9 : 05–10 : 00 [7]. The third stage of this event corresponds directly to the development of a system of giant loops and their ascent to coronal heights of 100 000 km and more.

The second example is the cusp-type limb flare of February 21, 1992 [1] mentioned in the Introduction,

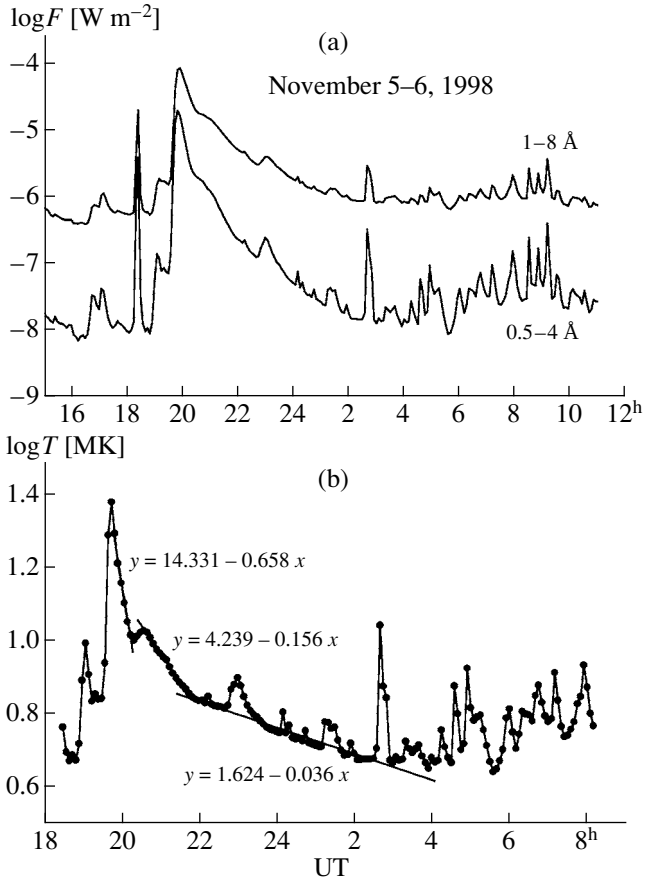

Fig. 5. Same as Fig. 3 for the sigmoidal flare of November 5–6, 1998.

which was characterized by a prolonged glow near the top of the loop. A linear interval after the time of the maximum temperature is clearly visible in Fig. 4a. Emission by the loop feet is almost undetectable for most flares occurring at or behind the limb. Therefore, the linear interval closest to the maximum corresponds to the characteristic time t_2 over which the energy is efficiently released in the cusp region. In the February 21, 1992 flare, this energy release appears to decrease at 4:30 UT, and the emission measure reaches its maximum at this time (the cusp-like point in the upper right-hand corner of Fig. 4b); later T and EM begin to decrease considerably. The ascent of the loops was also observed in this event, and their height exceeded 100 000 km at approximately 7:00 UT [1, 9].

We adopt the sigmoidal flare of November 5, 1998 as our third example. Fairly high loops can be observed beyond the active region in the images of such flares in some X-ray lines, and appear to be rising to greater heights. Since the neutral line often curves and crosses the active region, such sources have a sigmoidal (S) shape. In some cases, the process propagates beyond the active region only on one side, rather than on both sides.

The ejection of the upper part of the loop system may be responsible for the subsequent darkening of the X-ray image, which often occurs in very large regions and represents a continuation of the characteristic S-like shape. This is called the dimming effect or, in some cases, directed (collimated) dimming [10, 11]. Sigmoidal flares can be considered a specific (weaker) manifestation of dynamical flares [9].

Figure 5 presents the fluxes in the same two channels and the temporal behavior of $\log T$ for the November 5, 1998 flare. Such flares usually have quite flat tops. There is a characteristic step in the temperature behavior at 20:35 UT, as in many other prolonged events. This step is manifest only very weakly in the flux plots, sometimes being barely visible; it should not be confused with a secondary maximum far into the stage of decay, such as are usually associated with small flares in other active regions responding to a main event.

The transition from t_1 to t_2 in Fig. 5b coincides with the first appearance of a CME at 20:33 UT in the images of the SOHO C2 coronograph [4]. The Hα flare ribbons are already appreciably separated at this time; i.e., the height of the quasi-stationary loops has

Table 1. Parameters of the decay phase of prolonged X-ray flares

Date	Time (UT)	Class	Δt, h	Magnitude	λ	φ	t_1, h	t_2, h	t_3, h
March 10, 1989	18:48	X4.5	190	3B	31°	−22°		3.96	79.4
Sept. 29, 1989	10:47	X9.8	228					3.54	56.6*
May 15, 1990	12:46	X1.7	207	3B	42	−38		4.00	62.2
Jan. 27, 1991	14:40	X1.9	182	1B	−14	−59		4.04	62.5
Jan. 31, 1991	1:58	X1.3	201	2B	−17	35		4.46	13.8
March 7, 191	6:11	X5.5	206	3B	−20	−66			26.9
March 23, 191	3:05	M6.8	198	2B	−24	−11		7.53	32.2
March 31, 191	19:27	M6.3	272					7.68	28.4
June 4, 1991	3:37	X12	233	3B	30	−70		8.97	
June 15, 91	6:33	X12	284	3B	33	69	2.58	7.7	59.5*
June 28, 91	4:54	M6.0	334					4.86	90
Aug. 25, 1991	0:31	X2.1	272	2B	24	−77	3.74	7.72	16.3, 79.0
Feb. 21, 1992	2:20	M3.2	190					6.51	62.9*
Feb. 27, 1992	9:22	X3.3	221	3B	6	2		6.23	53.1
March 6, 193	20:14	M7.7	124	3B	−4	−29		2.28	13.9
March 12, 193	16:48	M7.0	234	3B	0	51	2.80	9.88	39.7
March 15, 193	20:39	M3.0	41	2F	−3	88		3.61	15.4, 72.3*
June 26, 93	14:55	C1.0	286					8.5	47.6
Apr. 29, 1998	16:06	M6.8	53		−18	−20	2.87		27.0
Sept. 30, 1998	13:50	M2.9	200		23	81	2.58	8.99	
Nov. 5, 1998	19:00	M8.4	72		22	18	1.52	6.42	27.9
July 4, 2000	10:05	X5.7	40	3B	22	7	1.97		93.5

So-called dynamical flares are marked by an asterisk in the last column (for more details, see text).

already reached its maximum. A pronounced dimming effect was observed in this event. Because the flare on November 5, 1998 was on the disk, the interval t_3 derived from the flux behavior cannot be identified with the system of giant arches in an obvious way.

Note that the intervals characterized by the times t_1 and t_2 cannot be identified in all cases, and the designations t_1 and t_2 are sometimes tentative. The quantity t_1 is absent for flares at or behind the limb, so that we immediately see the time interval corresponding to t_2.

Table 1 contains general information on the chosen flares—the event's time of onset, X-ray class and duration Δt according to the GOES catalog, optical magnitude, distance from the central meridian λ, and latitude φ. The characteristic times for the temperature variations t_i are presented in the last three columns of this table. For two events, two values of t_3 are presented, which may be associated with the formation of giant loops on different scales.

Studying the temporal behavior of the temperature in these flares showed exponential changes of T in three time intervals in the decay phase, corresponding to the end of the two-ribbon flare, glow in the cusp region, and the formation of a system of giant loops. We derived the variation time intervals for powerful prolonged solar flares $t_1 = 1 - 3$, $t_2 = 3 - 10$, and $t_3 = 15 - 100$ h.

Unfortunately, there are not yet sufficient data on giant solar flares to enable trustworthy identification of the characteristic times t_1, t_2, and t_3 with the processes indicated above. Note that sections of the X-ray curves affected by the background were not used in our determination of the temperatures and emission measures for giant flares.

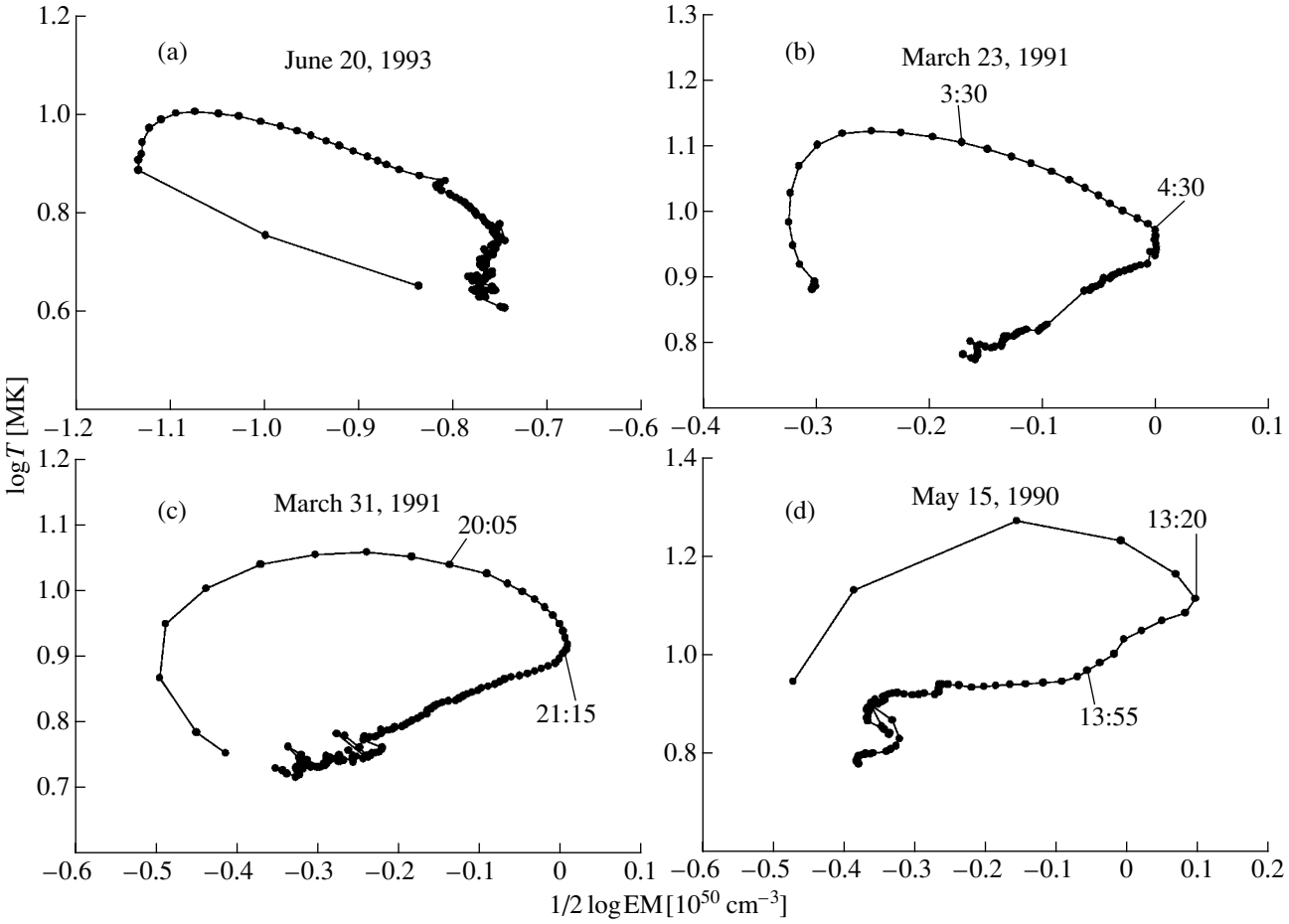

Fig. 6. $\log T - 1/2 \log EM$ diagrams for four flares. As in Fig. 4b, time changes in the clockwise direction, and the times of the beginning and end of the second interval t_2 are given in UT.

The approach of analyzing the soft X-ray emission of flares using $\log T - 1/2 \log EM$ diagrams was widely applied several years ago (see, for example, [12] and references therein). We constructed such diagrams for all the flares in our sample. A diagram for the cusp flare of February 21, 1992, is presented in Fig. 4b; several other examples are given in Fig. 6. An interesting feature of these diagrams is a certain hysteresis. This curve describes the evolution of a system of coronal loops from its formation to its subsequent decay. Figure 6 demonstrates a gradual transition from weak, purely coronal phenomena (Fig. 6a) to powerful two-ribbon flares with complex spatial and temporal structures (Fig. 6d). In purely coronal phenomena (Fig. 6a) with comparable times for the increase and decrease of the high-temperature emission, the maximum temperature occurs at relatively small emission measures. Further, the EM gradually increases to its maximum as the temperature gradually decreases. Only one example from this widespread class of coronal events is given here. We can see a gradual change in the shape of the hysteresis in Figs. 6b and 6c, when the maximum temperature shifts to the middle of the high-temperature part of the diagram. The same change of the hysteresis shape continues in powerful phenomena, with the hysteresis becoming inclined in the opposite direction relative to the axes, and the number of points in the high-temperature branch considerably decreasing. Efficient particle acceleration begins to occur here, producing an additional contribution to the thermal emission of these prolonged phenomena.

Signs of additional heating of coronal loops in the cusp region can be detected in a large number of events. This is manifest in these diagrams by the duration of the interval t_2 from some time after the temperature maximum up to the time when the EM reaches its maximum or begins to sharply decrease. Such behavior is seen in Figs. 4b, 6b, and 6c, where the times for the beginning and end of the intervals t_2 for these events are marked. A sharp cusp-like feature in the diagram, corresponding to the onset of the decrease in the emission measure against the background of the decreasing temperature, can be

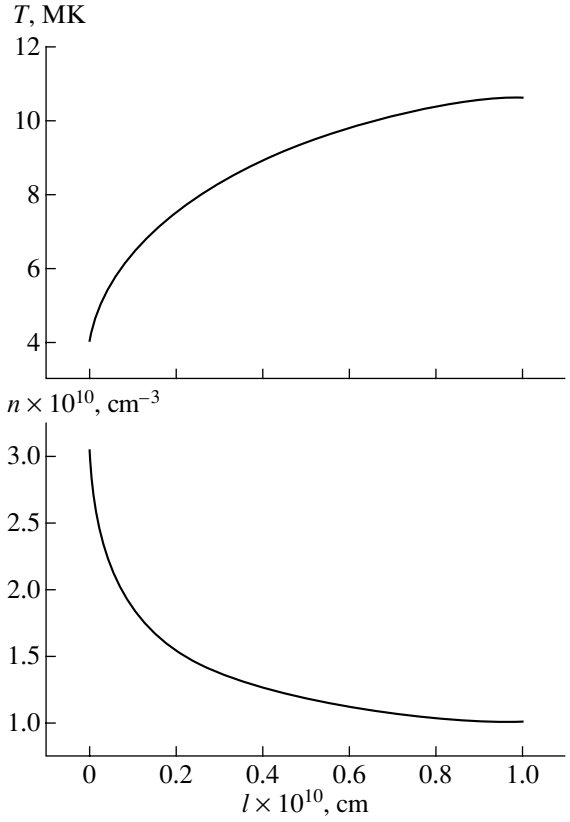

Fig. 7. Distribution of temperature and electron density along the loop (from the base to the top). The initial values for modeling were a half-loop length of 5×10^9 cm and a temperature throughout the loop of $T = 4$ MK.

seen only in the event of February 21, 1992, which is a typical cusp flare. However, along with the events of March 23 and 31, 1991, there was also additional heating in the events of January 31, 1991, June 28, 1991, and possibly some others. On the other hand, in several powerful phenomena (for example, the event of May 15, 1990), the interval t_2 corresponds to points in the lower branch of the diagram, after the maximum of the emission measure. In contrast to the case of quasi-equilibrium coronal loops with prolonged heating in the cusp region, the situation discussed here is determined by the evolution of beams of accelerated particles, and the dynamics of the phenomena are more clearly expressed.

Cases when a system of giant coronal loops was actually observed are marked by asterisks in the last column of the table. Such flares were studied in detail by Svestka [9], and are often called dynamical flares. The onset of the ascent of the loop system (heights above 100 000 km) is reflected in the temporal behavior of the temperature. For example, this is the beginning of the third time interval (t_3) in Fig. 3. A prolonged decrease in the temperature with $t_3 =$ 50–80 h is characteristic of all four events marked by asterisks. It seems reasonable to suppose that, when such prolonged decreases in the temperature are detected at large (compared to the background) radiation fluxes, the period t_3 is associated with the formation of systems of giant arches.

The emission measures for most of the analyzed flares reach their maxima after the temperature maximum. Consequently, the evaporation of plasma from the loop feet to its coronal portion likewise continues during this time. Of course, this evaporation occurs in a somewhat different way, and the upward motions will have different speeds from those for explosive evaporation in the impulsive phase. The upward evaporation of plasma decreases at subsequent times in the decay phase, so that the process approaches a purely coronal process; i.e., it resembles the evolution of a fixed mass of gas. Note, however, that the analysis of the gradient dy/dx in Fig. 6 and the corresponding dependences for other events did not lead to any definite conclusions about the physical mechanisms for the flares, in contrast to some earlier conclusions for solar and stellar flares (see [13] and references therein).

4. MODELING THE GAS-DYNAMICAL PROCESSES IN THE DECAY PHASE OF A FLARE

Thus, in most cases, the soft X-ray emission decreases quite rapidly after the flare maximum, after which the rate of decrease becomes substantially smaller. We carried out a set of model calculations to investigate the physical reasons for this prolonged X-ray glow.

We modeled the phase of gradual decrease of the X-ray emission neglecting magnetic forces. In other words, we assumed that the pressure of the hot plasma exceeds the magnetic pressure: the plasma parameter $\beta = 8\pi p/B^2 > 1$. For simplicity, it was also assumed that the loop has a semicircular shape with constant cross section. In this case, we can use a system of one-dimensional gas dynamical equations. The gravitational force, heat transfer along the magnetic field lines, and radiative energy losses were taken into account. The evaporation of material from the loop feet to its upper part can be neglected, since, for most of the events, the phase under investigation covers the time of the emission-measure decrease in the $\log T - 1/2 \log \mathrm{EM}$ diagrams. When modeling the processes in this phase, we can restrict our attention to purely coronal phenomena, i.e., to the evolution of a loop containing a fixed mass of plasma.

Using the experience of previous studies [14, 15], we concentrated on the flare of March 6, 1993. This flare belongs to an unusual series of prolonged flares observed in March, 1993; it was the shortest event

in this series, and its value of t_2 in Table 1 is the smallest. The plasma heating near the top of the loop was chosen to maximize the agreement between the calculated and observed temperature profiles. The heating function had the same form as in [14]; namely, the heating was distributed in space and time taking into account a small, time-independent contribution to stabilize the initial state. The latest version of the gas-dynamical code [15] was used in the calculations.

A comparison of the computed and observed behavior of the temperature in the decay phase of this flare is presented in Fig. 3 in [16]. Figure 7 shows the distributions of the density and temperature along the loop for calculations with a total heating energy of 3×10^{30} erg over 2.5 h during the development of the slow phase of the process. The mean density in the loop only slightly exceeds 10^{10} cm^{-3}, while the loop half-length doubed compared to its initial value, reaching $l = 10^{10}$ cm (so that the height of the loop is slightly less than 70 000 km).

These calculations confirmed the existence of a high-temperature plasma in the loop as long as energy is supplied to the source of X-ray emission. Moreover, both the density and height of the loops in Fig. 7 are in good agreement with observations. Indeed, typical densities of $\approx 10^{10}$ cm^{-3} and heights of 70 000 km began to be used for loops associated with large two-ribbon flares as early as the 1970s, after the publication of the monograph of Svestka in 1976. These values are supported by the detected emission measures and the dimensions of the flare loops observed in the X-ray images of the flare of March 6, 1993.

Performing calculations for all times of powerful flares based on the evolution of a purely coronal loop (as for the flare of March 6, 1993) is made difficult by the observed strong asymmetry between the growth and decay phases of the soft X-ray emission. We obtained a very high velocity for the plasma in the loop when modeling the observed X-ray growth phase, which lasted for only 0.5–1 h in the analyzed events. When the expansion of the loop is replaced by contraction, the downward motion of plasma leads to the development of shock waves in the lower parts of the loop, hindering further computations. To describe the subsequent, very long decay phase for the densest loops, we must either dampen such motions artificially or carry out calculations for the rise and decay phases separately when modeling powerful phenomena [15].

Calculations similar to those of [15] but with the solar gravitational acceleration showed that decay phases with t_2 from 3 to 10 h can be described using the above modeling. Of course, the characteristic times for the heating decrease for the other events in Table 1 are factors of two and more greater than for the flare of March 6, 1993. In addition, the plasma density in the loops decreases slightly, and the loop systems of the most powerful events are formed at heights of 100 000–130 000 km. Comparison of the modeling results with the observations yields a rather obvious conclusion: the number of loops (or, in other words, the length of the loop system along the neutral line) is greater for powerful, prolonged flares.

Thus, our modeling of the decay phase of powerful flares is in agreement with the observations, and the energy balance in the X-ray source imposes very strong constraints on the heating function. In this way, the theory for the flare must explain the appearance of the required powerful and prolonged heating.

Naturally, the loop system will expand and be ejected outwards after a sudden increase in the heating. Unfortunately, the one-dimensional calculations do not enable a detailed description of the observed velocities of the loop's ascent, especially at heights where the plasma parameter β becomes of the order of unity. However, an increase in t_3 relative to t_2 would be natural.

5. POSSIBLE ROLE OF CORONAL MASS EJECTIONS IN THE OVERALL NON-STATIONARY PROCESS

Recent studies have indicated that a flare and CME should be treated like a unified non-stationary process in which the CME plays an important role. The coronal mass ejection is observed in white light, due to the scattering of photospheric radiation by the electrons of the ejected plasma cloud. The birth of the CME is not easily observable in this range, but these phenomena can be detected by the SOHO C2 coronograph for about 10 min from some distance from the surface out to about six solar radii, and by the C3 coronograph for several hours out to distances of about 30 solar radii. Several CMEs per day are observed at the solar-activity maximum, but large CMEs are observed only once or twice per week [17, 18].

We compared the characteristic temperature behavior in a flare and the development of a CME, taking the onset of a type-II radio burst to indicate the passage of a CME. Table 2 presents the durations of the intervals t_2, the onsets of the intervals t_3, and the onsets of type-II radio bursts or the first observations of CMEs by the C2 coronograph.

The data for the last two solar cycles demonstrate that CMEs are often observed as early as during the impulsive phase of flares. However, in the case of two-ribbon flares with complex spatial and temporal structures and powerful, prolonged phenomena, CMEs are not always associated with an impulse and

are observed at times close to the appearance of the characteristic step or small secondary maximum in the time dependence of the temperature. A comparison of the onset times for the second interval and the type-II radio bursts in Table 2 indicates that this feature is located between the first and second linear intervals of the curve, i.e., between t_1 and t_2. For most events, the radio burst occurs about 20 min before the beginning of the interval t_2. In some cases, the main role of the CME is to initiate the development of the flare in a new part of the active region or activity complex.

Note the existence of a clear causal relationship: a system of giant arches cannot form (i.e., a dynamical flare cannot develop) without a powerful CME. The role of the CME is not to turn on an additional powerful heating source, as is supposed in studies based on the Kopp–Pneuman model. Instead, the CME creates the conditions necessary for the ascent of giant arches.

After a CME, the perturbation from the flare region (especially a fairly powerful one) propagates along a neutral line of the large-scale magnetic field. There are three different scenarios for the subsequent development of powerful events. The flare can either propagate to a neighboring active region in the same activity complex, and/or go to a region of weak magnetic fields beyond one or two boundaries of the active region (so-called sigmoidal flares [4]), and/or initiate the ascent of coronal loops, producing systems of giant coronal loops. Note that the formation of such systems of giant arches sometimes occurs several hundred thousand kilometers from the initial flare along the neutral field line, and this system exists in the solar corona for 0.5–1 days.

6. DISCUSSION

First, let us summarize the specific results of our study. We selected events with X-ray classes above M1 and durations over 3 h from a database containing 51 000 X-ray flares. The temporal behavior of the temperature and emission measure were determined for these events using data on the soft X-ray emission in two channels of the GOES satellites.

The temperature in the source decreases exponentially within several separate time intervals in the decay phase of the flares. We emphasize that a substantial change ("extention") of the temporal profile of an X-ray flare occurs when a CME propagates in the lower corona and actively influences the structure of the large-scale magnetic field. This facilitates the ascent of coronal loops in dynamical flares to heights exceeding 100 000 km.

The emission measure EM reaches its maximum later than the temperature, in contrast to the expectations for purely coronal processes. The $\log T - 1/2 \log \mathrm{EM}$ diagrams for flares of various types can be used to follow the gradual transition from powerful phenomena involving appreciable evaporation of material inside coronal arches to events related to the evolution of the coronal loops themselves. We derived the size and plasma density of one loop via gas-dynamical modeling using the observed energetics of the phenomenon. The resulting loop height 70 000–100 000 km and electron density $n = 10^{10}$ cm^{-3} agree very well with direct observations of such flares.

The most illustrative manifestation of a flare in the soft X-ray band is the formation of a system of hot coronal loops. This was called the main or hot phase by Syrovatskiĭ. Its duration is not very different from the time for the free emission of the plasma localized in the loops. This statement can be formulated in another way: although some additional heating takes place in the final stage of a two-ribbon flare, it does not fully compensate the corresponding radiative losses.

However, a high plasma temperature is often maintained over many hours in powerful solar flares. This is precisely the main problem considered in the present study. Two of our conclusions were unexpected: (1) there are two characteristic time intervals with appreciably different rates for the temperature decrease in the decay phase, and (2) the functions describing this decrease are very close to exponential.

A natural origin for the prolongation of powerful flares is the formation of several successively developing loop systems, which can be tentatively identified with flares in the activity complex. For example, the flare of July 14, 2000 was a rapid event in the northern part of the region and later evolved into a two-ribbon flare in which an additional system of loops developed after 10:24 UT. The onset of the development of this loop system coincides with a second, more powerful, type-II radio burst and the maximum of the γ-ray emission [3]. One characteristic feature of this flare was the formation of a common loop system in its final stage, after 10:30 UT. This loop system joined all three preceding sections (the impulse and both loop systems), and the height of the entire system began to increase.

The soft X-ray emission of the flare of July 14, 2000 considerably decreased within one hour of its onset. The subsequent glow of the large-scale loop system, observed just above the activity complex, was substantially weaker than the maximum brightness. Thus, as for many other powerful, compact, two-ribbon flares, the formation of new parts of the loop system did not appreciably (by many hours) prolong

Table 2. Periods of prolonged X-ray emission and onsets of type-II radio bursts or CMEs

Date	Time (UT)	Class	Interval t_2	Beginning of t_3	Beginning of type-II radio burst or CME
March 10, 1989	18:48	X4.5	19:30–20:30	23:25	19:20
Sept. 29, 1989	10:47	X9.8	11:55–12:55	15:00	11:26
May 15, 1990	12:46	X1.7	13:20–13:55	17:00	13:05
Jan. 27, 1991	14:40	X1.9	16:10–17:05	19:30	15:43
Jan. 31, 1991	1:58	X1.3	2:20–3:20	4:10	2:07
March 7, 1991	6:11	X5.5	–	9:25	7:47
March 23, 1991	3:05	M6.8	3:30–4:30	5:15	–
March 31, 1991	19:27	M6.3	20:05–21:15	21:25	19:41
June 4, 1991	3:37	X12	4:30	–	4:15
June 15, 1991	6:33	X12	9:15–10:20	11:10	8:07
June 28, 1991	4:54	M6.0	5:45–7:10	10:05	–
Aug. 25, 1991	0:31	X2.1	1:35–2:25	2:50	0:49 (IV)
Feb. 21, 1992	2:20	M3.2	3:45–4:50	7:10	3:07
Feb. 27, 1992	9:22	X3.3	10:10–11:25	14:50	9:51
March 6, 1993	20:14	M7.7	20:40–21:05	22:00	20:26
March 12, 1993	16:48	M7.0	18:50–19:55	20:40	17:52
March 15, 1993	20:39	M3.0	21:45–00:10	1:00	21:22 (IV)
Apr. 29, 1998	16:06	M6.8	–	17:10	16:58 (CME)
Sept. 30, 1998	13:50	M2.9	14:30–15:25	–	–
Nov. 5, 1998	19:00	M8.4	20:35–21:25	21:50	20:33
July 14, 2000	10:05	X5.7	–	12:15	10:27

the lifetime of the high-temperature plasma of this flare.

What is the origin of the more prolonged glow? A typical event with a linear interval t_2 for the logarithm of the temperature is the cusp flare of February 21, 1992. Table 1 shows that a linear interval corresponding to t_2 can be identified for most of the events, and the characteristic times t_2 are in the range 3–10 h. It can reasonably be assumed that all these intervals correspond to energy release in the cusp region. Recall that, for the powerful flares under consideration, the interval t_2 corresponds to times when the fluxes are still high, appreciably exceeding the background level.

The X-ray fluxes from the entire Sun include both emission from loops inside the activity complex and the glow of external plasma. Observations in the current cycle enable us to directly detect the propagation of non-stationary process beyond a given active region. The perturbation propagates quite rapidly along a neutral line of the large-scale magnetic field. If it reaches another active region, a new flare is sometimes initiated. Such a flare is manifest as an additional maximum (or maxima) in the decay phase of the luminosity curve of the main flare. If there are no flares with appreciable power in other active regions, the luminosity of the bright points along the neutral line is usually rather weak.

There were only a few cases for which we have complete information on the times and localizations of systems of giant loops that developed during a phenomenon and can be identified with the interval t_3. These are for observations of the largest systems of giant arches near the limb, which contribute considerably to the total X-ray flux. Note that, in some cases, there may be several loop systems (rather than one), which stop at different heights in the course of their development. For this reason, Table 1 sometimes contains two values of t_3 for the same event.

Thus, t_3 fairly often corresponds to an actual glow due to a system of giant loops, although, in some cases, an appreciable contribution is made by the activation of small-scale elements located along the neutral line, sometimes at large distances from the main flare.

Recent studies demonstrate that CMEs should be considered an integral part of an overall nonstationary process that includes a prolonged flare. CMEs are often observed as early as during the impulsive phase, facilitating the transformation of an impulsive event into an ordinary two-ribbon flare. In some flares with complex spatial and temporal structures, the development of a CME leads to the appearance of a new part of the loop system (and, accordingly, new ribbons). There is a strong interaction between the CME and the flare, which is not well understood and requires more detailed study. The propagation of the flare process beyond the active region, i.e., to regions of weak magnetic fields, has been considered in several recent papers on sigmoidal flares and various types of dimming effect. There is every reason to believe that the CME stimulates the formation of a source of plasma heating at coronal heights, both directly over the arch system near the cusp and at very large distances from the solar surface, in the distant magnetospheric tail of the active region. This prolongs the duration of the overall phenomenon and its soft X-ray emission.

Let us now briefly discuss the origin of the exponential decrease in temperature. It is clearly important that the temperature in each loop of the system varies approximately exponentially, and the processes in neighboring loops are not completely synchronous. Averaging the emission over a statistical ensemble of loops results in the observed effect for both a two-ribbon flare and the subsequent stage of dynamical phenomena. This averaging does not lead to an appreciable deviation of the temporal behavior of the temperature in the overall source from its behavior (decrease) in each loop.

Most of the soft X-ray emission by powerful solar flares is associated with the development of new parts of the flares located inside the activity complex. Therefore, the conclusion that powerful solar phenomena are associated with the evolution of local magnetic fields remains unchanged. There can be a release of energy in the cusp, but it is not usually a decisive factor, at least when the X-ray fluxes are close to their maximum values. However, the energy release in the cusp region of powerful flares can substantially prolong the duration of the X-ray glow. As a rule, this behavior is characteristic of phenomena whose development occurs outside the active region or activity complex and is more closely associated with the large-scale magnetic fields and powerful ejections of material.

In conclusion, we note that the flares analyzed here are similar to stronger X-ray flares on active, late-type stars—in particular, subgiants in RS CVn binaries—which are currently being very intensely studied.

ACKNOWLEDGEMENTS

This work was supported by the Russian Foundation for Basic Research, project nos. 99-02-16289, 01-02-17580, 02-02-17086.

REFERENCES

1. S. Tsuneta, Astrophys. J. **456**, 840 (1996).
2. T. G. Forbes and L. W. Acton, Astrophys. J. **459**, 330 (1996).
3. I. M. Chertok, S. Kahler, H. Aurass, and A. A. Gnezdilov, Sol. Phys. **202**, 337 (2001).
4. H. Wang, P. R. Good, G. Yang, *et al.*, Astrophys. J. **536**, 971 (2000)
5. H. A. Garcia, Sol. Phys. **154**, 275 (1994).
6. R. Mewe, J. S. Kaastra, and D. A. Liedahl, Legacy **6**, 16 (1995).
7. B. B. Akimov, P. Ambroz, A. B. Belov, *et al.*, Sol. Phys. **166**, 107A (1996).
8. A. V. Belov, E. A. Eroshenko, and M. A. Livshits, in *Proceedings of the Eight International Symposium on Solar Terrestrial Physics, Sendai, Japan, 1994,* p. 26.
9. Z. Svestka, F. Farnik, H. S. Hudson, *et al.*, Sol. Phys. **161**, 331 (1995).
10. B. J. Thompson, J. B. Gurman, W. M. Neupert, *et al.*, Astrophys. J. **517**, L151 (1999).
11. R. A. Harrison and M. Lyons, Astron. Astrophys. **358**, 1097 (2000).
12. B. Sylwester, J. Sylwester, S. Serio, *et al.*, Astron. Astrophys. **267**, 586 (1993).
13. F. Real and G. Micela, Astron. Astrophys. **334**, 1028 (1998)
14. K. V. Getman and M. A. Livshits, Astron. Zh. **77**, 295 (2000) [Astron. Rep. **44**, 255 (2000)].
15. I. M. Livshits and M. A. Livshits, Astron. Zh. **79** (3), 364 (2002) [Astron. Rep. **46**, 327 (2002)].
16. M. A. Livshits, A. V. Belov, and A. B. Struminskiĭ, Astron. Vestnik **35**, 559 (2001).
17. A. Hundhausen, in *Many Faces of the Sun,* Ed. by K. Strong *et al.* (Springer-Verlag, New York, 1999), p. 143.
18. O. C. St. Cyr *et al.*, J. Geophys. Res. **105**, 18169 (2000).

Translated by Yu. Dumin